UNCONVENTIONAL ADDITIVES FOR IMPROVING THE SOLID ELECTROLYTE INTERPHASE IN LI-ION BATTERIES

by

Robert Scott Young

Submitted in partial fulfilment of the requirements for the degree of Master of Science

at

Dalhousie University
Halifax, Nova Scotia
August 2021

To Lucy

TABLE OF CONTENTS

LIST OF TABLES

LIST OF FIGURES

ABSTRACT

Lithium-ion batteries (LIBs) are used in a wide variety of applications that are pushing for higher capacity and lifetime. Many LIBs contain graphite-based negative electrodes which are approaching their capacity limit. Silicon-based negative electrodes have the potential of providing a much higher capacity but struggle with severe volume expansion and contraction. Alloying Si with an electrochemically inactive material can suppress the volume expansion of the alloy and lead to better cycling. However, such Si-inactive alloy materials require more optimization of the solid electrolyte interphase (SEI) formation to increase capacity retention. The SEI of Li-ion cells is a passivating film that forms on the electrode/electrolyte interphase via the decomposition of electrolyte additives, solvents, and salts during the first few cycles. Optimal formation of the SEI on the negative electrode is related to increased performance in LIBs, leading to increased capacity retention, lifetime, and safety.

In this thesis, more unconventional methods of improving the formation of the SEI are explored. By incorporating solid additives into active materials, utilizing a multifunctional binder additive, and using water as a beneficial electrolyte additive, this work aims to beneficially modify SEI formation for better Li-ion cell performance. LiF was found to be a good solid phase electrode additive in Si-Fe alloys that led to improved capacity retention. Synthesized poly-VC is explored as a binder additive to modify SEI formation in Si-Fe alloy electrodes. Water is introduced as an electrolyte solution additive that led to improved cycling in NMC/Si-alloy full cells. The goal of this work is to find alternatives to the expensive conventional additives currently implemented in LIBs.

LIST OF ABBREVIATIONS USED

AC	Alternating Current
AIBN	Azobisisobutyronitrile
BMF	Blown Microfiber
BSE	Backscattered Electron
C	C as in C-rate, Capacity
CCCV	Constant Current Constant Voltage
C_{DL}	Double Layer Capacitance
CSL	Compact Stratified Layer
d	Atomic Plane Spacing
DEC	Diethyl Carbonate
DFT	Density Functional Theory
DMC	Dimethyl Carbonate
DTD	1,3,2-Dioxathiolane-2,2-Dioxide
E_B	Binding Energy
EC	Ethylene Carbonate
EIS	Electrochemical Impedance Spectroscopy
E_K	Kinetic Energy

EMC	Ethyl Methyl Carbonate
FEC	Fluoroethylene Carbonate
HSA	Hemispherical Sector Analyser
HOMO	Highest Occupied Molecular Orbital
HOPG	Highly Oriented Pyrolytic Graphite
LCO	Lithium Cobalt Oxide
LFP	Lithium Iron Phosphate
LIBs	Lithium-ion Batteries
$LiMO_2$	Lithium Transition Metal Oxide
LMO	Lithium Manganese Oxide
LUMO	Lowest Unoccupied Molecular Orbital
MMDS	Methylene Methanedisulfonate
NMC	Nickel Manganese Cobalt Oxide
NMP	n-methyl-2-pyrrolidinone
OCV	Open Circuit Potential
PEI	Polymer Electrolyte Interphase
PI	Polyimide
Poly-VC	Polymerized Vinylene Carbonate

PVDF	Polyvinylidene Fluoride
R_{CT}	Charge Transfer Resistance
R_s	Electrolyte Resistance
R_{tot}	Total Impedance
SE	Secondary Electron
SEI	Solid electrolyte interphase
SEM	Scanning Electron Microscopy
SPI	Solid Permeable Interface
SPL	Solid Polymer Layer
V_{avg}	Average Discharge Potential
VC	Vinylene Carbonate
V_{cell}	Cell Potential
$V_{negatve}$	Negative Electrode Potential
$V_{positve}$	Positive Electrode Potential
XPS	X-Ray Photoelectron Spectroscopy
XRD	X-Ray Diffraction
Z	Impedance
Z_w	Warburg Impedance Element

θ	Incident Angle of Radiation
λ	Wavelength of Radiation
Φ_{sp}	Work Function of Spectrometer

ACKNOWLEDGEMENT

I would like to express my deepest appreciation to my supervisor Dr. Mark Obrovac and give thanks to all members of the Obrovac lab for providing a supportive and creative environment. I will be forever grateful for the inspiration and guidance that was given to me during my studies. I would like to also acknowledge Dr. Tim Hatchard for ensuring smooth sailing with my research by taking care of all the instruments in the Obrovac lab.

Special thanks to Dr. Alex Speed for helping synthesize materials for this work and to Andrew George for providing X-ray photoelectron spectroscopy data. Also, a special thanks to Xiang Yang for providing training and insight into the workings of the scanning electron microscope.

CHAPTER 1. INTRODUCTION

1.1 Motivation

As the world struggles to keep up with the growing energy demands in parallel with countering the effects of global warming, advancements in energy storage have become indispensable. Obtaining energy from renewable resources is necessary to alleviate fossil-fuel dependence and achieve net zero carbon emissions. However, due to the intermittent supply of renewable energy from sources such as wind and solar, it is crucial to implement reliable energy storage devices. Energy storage allows for continuous supply from the harvested energy taken from renewable energy sources which stabilizes energy availability and provides a more reliable grid design. While energy storage solutions exist that are quite sustainable and cost efficient, like pumped hydro,[1] the use of secondary electrochemical cells eliminates the dependence of geographic factors, such as the need of an elevated structure for pumped hydro. The most commercially viable secondary battery in use today is the lithium-ion battery which has considerable advantages over many other cell types, such as high energy density and long cycle life.[2]

While initially developed for portable electronics, lithium-ion batteries (LIBs) are now used in a diverse range of applications including electric cars, satellites, and grid storage.[3] LIB chemistry is based on the shuttling of Li-ions back and forth between positive and negative electrodes. The stored chemical energy is converted to electrical energy when the Li-ions move from the negative electrode to the positive electrode. This process has been highly optimized over the past few years, with some LIBs being expected to have service lives of several years or even decades.

LIBs are being pushed to their limit to enable their use in applications such as electric vehicles. For this application, LIBs are required to have a high energy density, for extended drive range, and a long cycle life, to match the lifetime of the vehicle.[4] This has lead to engineering solutions, such as minimizing the current collector and separator thicknesses, incremental morphology optimization, and increasingly complex electrolyte additive usage. As LIBs approach the limit of their capabilities, there is still more being asked of them.

LIB electrodes are not thermodynamically stable in electrolyte at their full state of charge, and yet some LIBs have a service life of many years. This is because a passivating film forms on electrode surfaces that slows reactions with electrolyte. This passivating film is often referred to as the solid electrolyte interphase (SEI), and is a heterogeneous structure comprised of various compounds that form via the decomposition of electrolyte additives, solvents, and salts during the first few cycles of a LIB.[5] This passivating film controls much of the performance of a LIB. SEI morphology and composition are sensitive to the solvents, salts, additives, and active materials used. For example, an SEI rich in LiF is typically thinner and results in faster Li-transport than one lacking LiF.[6] Environmental conditions, such as temperature, also can have an impact on SEI formation. Therefore, there are many factors to consider in the study of the SEI and in SEI optimization. Optimal SEI formation on a negative electrode translates to increased safety, lifetime, capacity retention, and overall LIB performance. It is therefore important that SEI formation is studied and understood, to maximize LIB performance, so that LIB technology remains a sustainable solution to the world's increasing energy storage needs.

1.2 Lithium-ion Cells

1.2.1 General Configuration

Li-ion cells store energy in the form of electrochemical potential energy. A schematic of a typical Li-ion cell is shown in Figure 1.1. Typically, LIB cells consist of a lithium transition metal oxide ($LiMO_2$) positive electrode, a graphite negative electrode, and an organic carbonate-based electrolyte containing a lithium salt. The positive and negative electrodes are kept isolated by a permeable porous separator, such as a multilayer polypropylene/polyethylene membrane, allowing Li-ion mobility while preventing electrode shorting.

The electrochemical potential is a result of the difference in the chemical potentials of lithium in one electrode versus the other. Li-ions travel back and forth between the positive and negative electrode materials during charge and discharge.

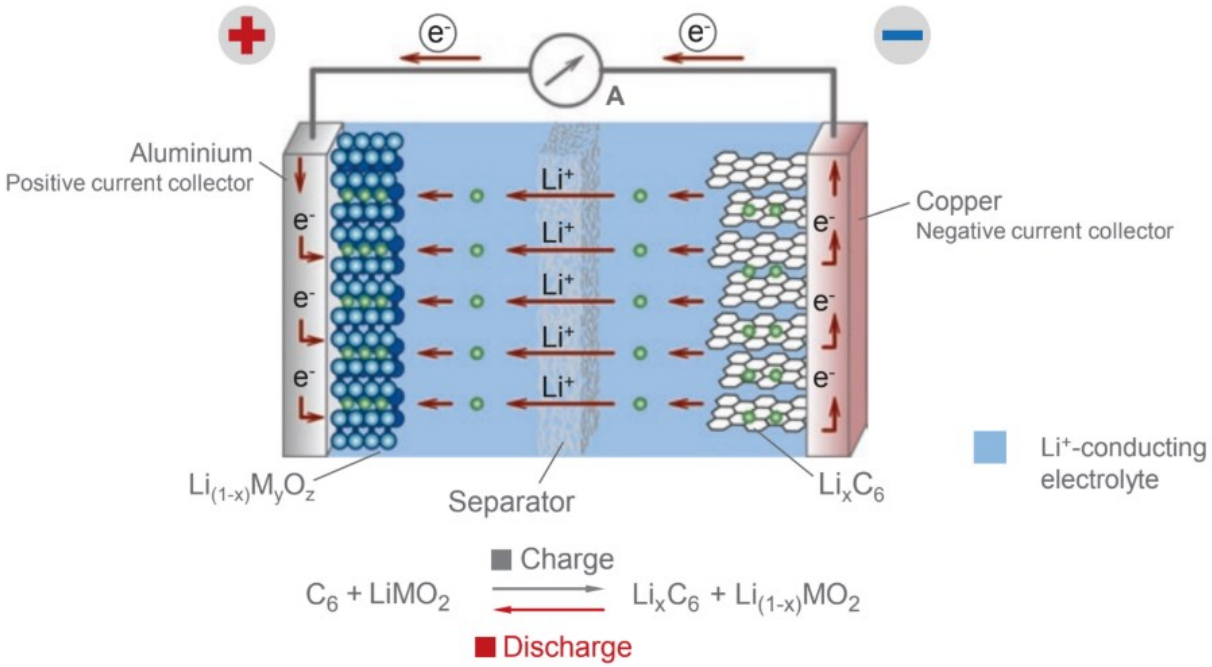

Figure 1.1. General schematic of a Li-ion cell consisting of a graphite negative electrode (right) and a layered transition metal oxide positive electrode (left).[7] Reproduced with permission from Reference 7.

During charge, the thermodynamically unfavored reaction of lithium travelling to the negative electrode occurs. The electrons are forced from the positive electrode to the negative electrode by an applied external potential, converting electric energy is into chemical potential energy which is stored in the cell. The now lithiated negative electrode experiences a decrease in potential to around 0.08 V vs. Li/Li^+, while the de-lithiated positive electrode encounters an increase in potential to around 4.3 V vs. Li/Li^+.[8] The two half reactions at the positive electrode and negative electrode during the charging process are:

$$LiMO_2 \rightarrow Li_{1-x}MO_2 + xLi^+ + xe^-$$

$$C_6 + xLi^+ + xe^- \rightarrow Li_xC_6$$

During discharge, the thermodynamically favorable reaction of lithium travelling to the positive electrode occurs. The positive and negative electrodes are connected by an external circuit that allows the flow of electrons and the flow of Li-ions; this can produce useful work.

Potential vs. capacity curves for a full cell, positive electrode, and negative electrode are shown in Figure 1.2. The potential vs. capacity curves in Figure 1.2 are from an artificial graphite negative electrode and an NMC532 positive electrode from CHEM 5312 course given by Professor Jeff Dahn. The potential of the positive electrode decreases, and the potential of the negative electrode increases until the cell reaches a lower potential cut-off. The resulting cell potential, V_{cell}, can be expressed as: $V_{cell} = V_{positve} - V_{negatve}$, where $V_{positive}$ is the potential of the positive electrode and $V_{negatve}$ is the potential of the negative electrode.

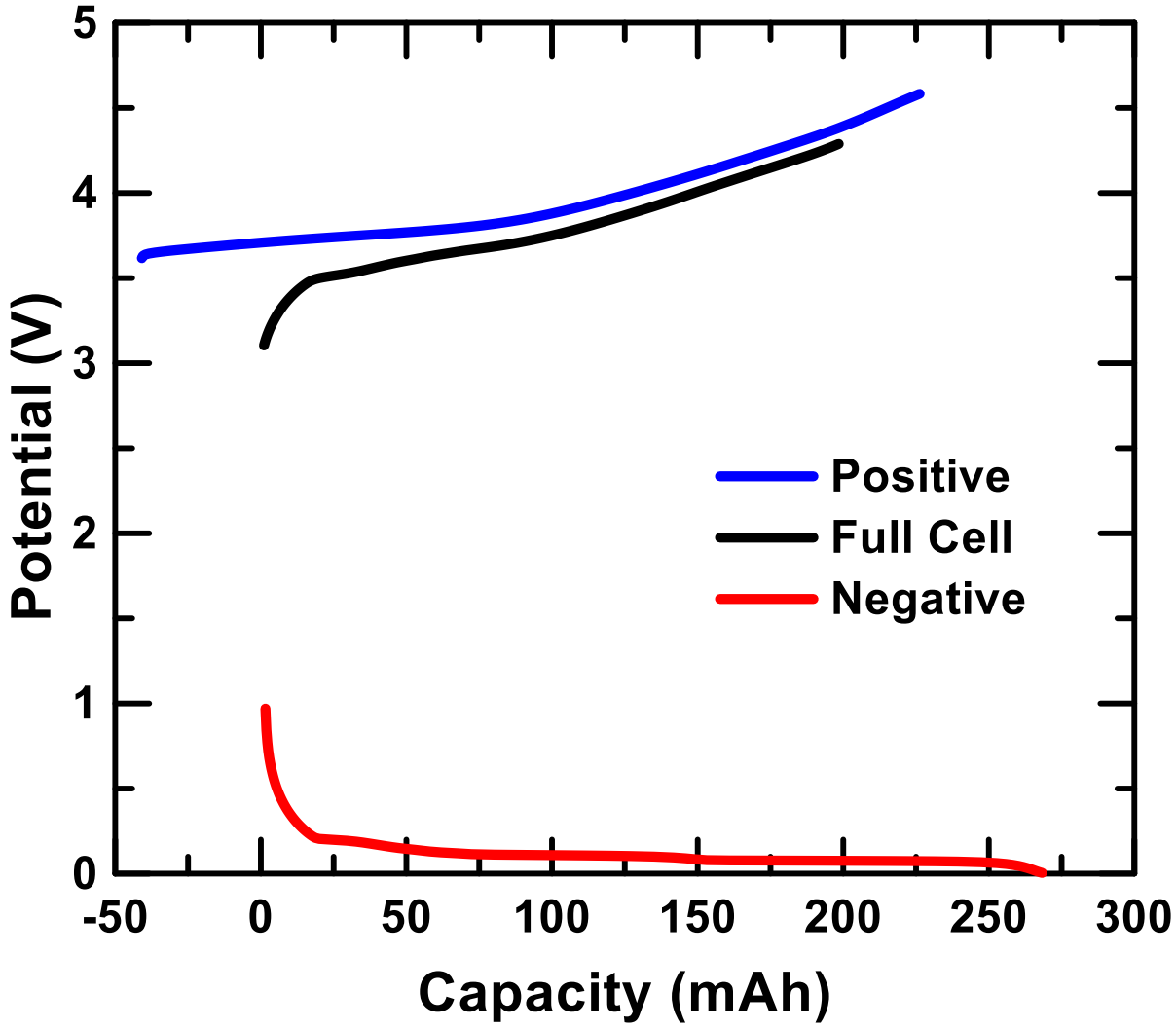

Figure 1.2. Galvanostatic potential vs. capacity curves for a full cell (black), positive electrode (blue) and negative electrode (red) vs. Li/Li^+.

1.2.2 Positive Electrodes

As previously mentioned, the typical positive electrode material is a $LiMO_2$ coated on an aluminum current collector. The electrode formulation also includes a binder, such as polyvinylidene fluoride (PVDF), and a conductive additive, typically a high surface area carbon black. $LiMO_2$ such as the layered and spinel structures shown in Figure 1.3, rely on lithium intercalation to store Li^+ ions. Although layered materials are commonly used, spinel and olivine structures are also found in some commercial applications.[8–10]

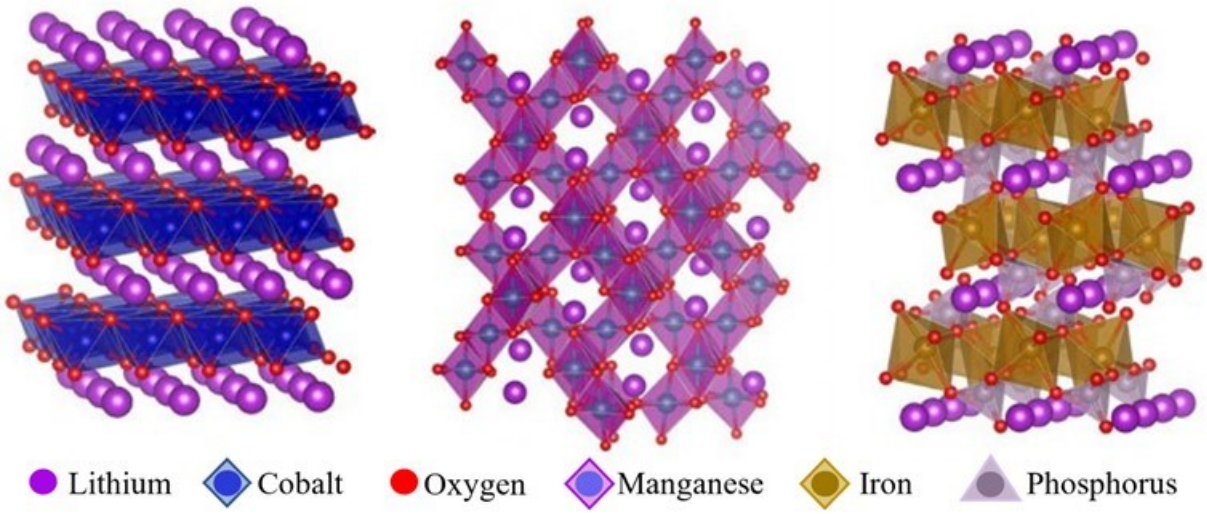

Figure 1.3. Crystal structures of common positive electrode materials. Layered lithium cobalt oxide (LCO) to the left, spinel lithium manganese oxide (LMO) in the centre, and olivine lithium iron phosphate (LFP) on the right.[11] Reproduced with permission from Reference 11.

1.2.3 Negative Electrodes

1.2.3.1 Intercalation

LIBs rely predominantly on intercalation chemistry to store energy. Conventionally, graphite coated on a copper current collector is used as the negative electrode. Graphite negative

electrodes have a high level of safety, compared to lithium metal. Graphite negative electrodes maintain a low reduction potential vs. Li/Li^+ (around 0.08V), and high volumetric capacity (719 Ah/L).[12] The structure of lithiated graphite is shown in Figure 1.4. Graphite is comprised of stacked graphene layers that are held together by weak Van der Waals forces between the graphene slabs. Lithium intercalates between the graphene layers and is most energetically stable in the center of a C_6 ring, not allowing additional Li-ions to occupy the immediate neighbouring C_6 ring site, due to coulombic repulsion.[13] This allows graphite to store a maximum of one lithium per six carbon atoms.[13,14] When it comes to storing lithium, intercalation materials are limited by the number of available crystallographic sites that can host lithium atoms. Therefore, there is a limitation on the energy density of these materials imposed by this host site limit.

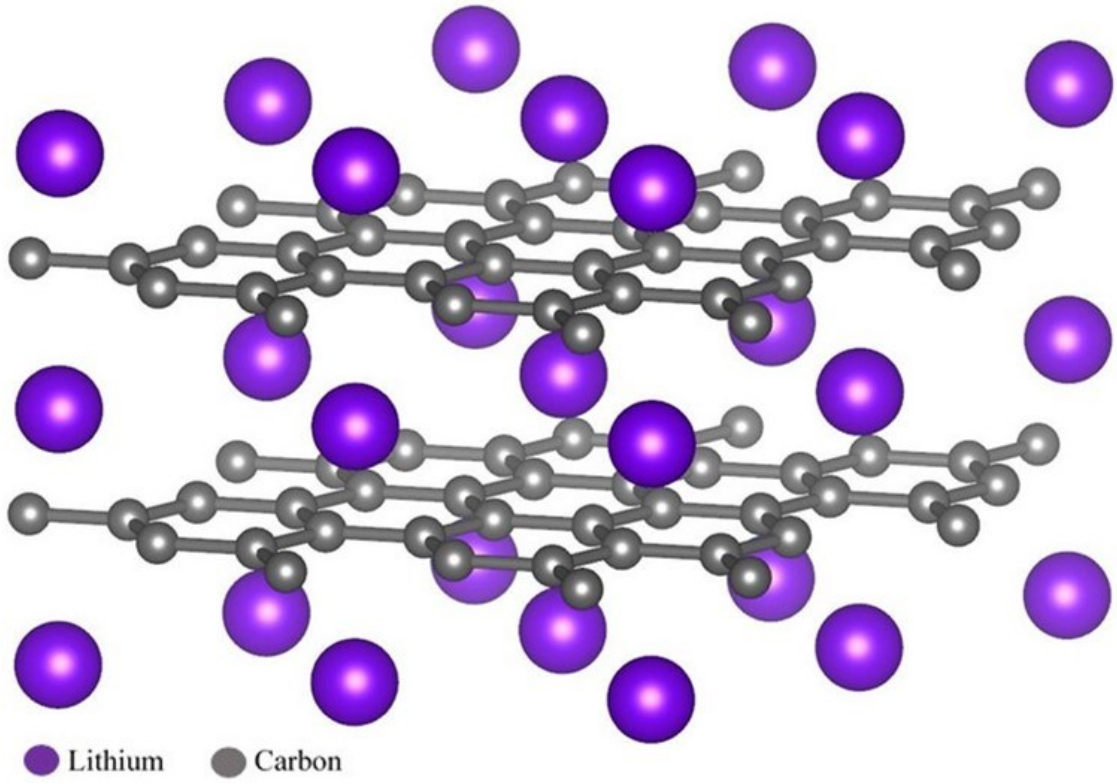

Figure 1.4. Structure of lithiated graphite.

1.2.3.2 Alloying

LIB negative electrodes are not restricted to graphite intercalation chemistry, any element that forms an alloy with lithium can also be used as a negative electrode material. During lithiation, the structure of an alloy can vary appreciably. Therefore, the storage capacity of such materials is not limited to the materials initial structure like that of intercalation chemistry. This allows alloy negative electrodes to store more lithium per host atom. For example, silicon can store 3.75 lithium atoms per silicon atom.[12] As a result, silicon has a much higher volumetric capacity than that of graphite (2194 Ah/L).[12] Volumetric and gravimetric capacities of some elements are given in Figure 1.5. This increase in volumetric capacity is common for alloy materials and the same is generally true for specific capacity, the capacity per unit weight. The specific capacity of silicon is 3579 mAh/g compared to graphite at 372 mAh/g.[12] Though this drastic increase in specific and volumetric capacity is alluring, the variation from the materials initial structure leads to increased volumetric expansion. For instance, fully lithiated Si expands 280% from its initial volume compared to graphite which expands by only 10%.[12,15]

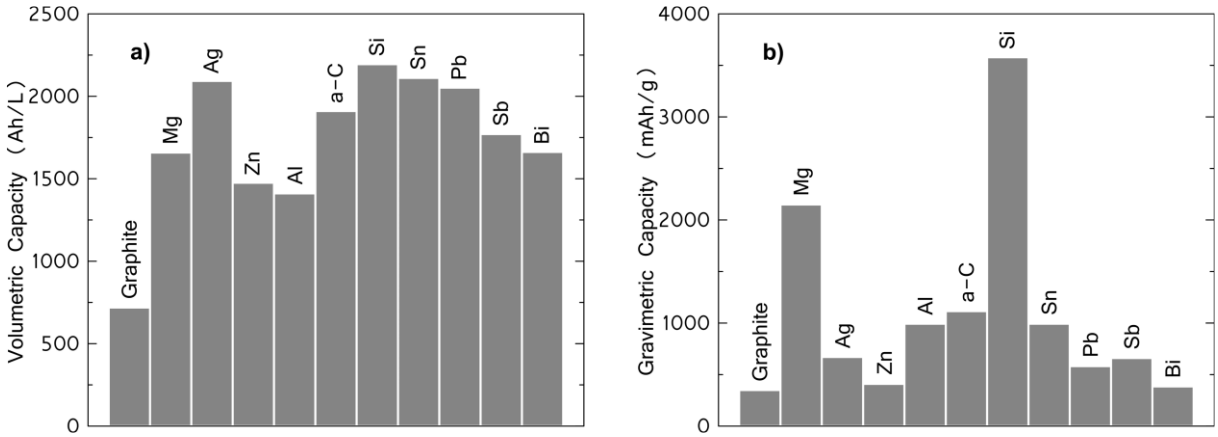

Figure 1.5. Volumetric and gravimetric capacities of elements calculated at full lithiation.[12] Reproduced with permission from Reference 12.

1.2.3.3 Lithiation of Si-Alloys

Silicon, as mentioned above, has a much higher volumetric capacity than graphite. The resulting increase of volumetric capacity originates from silicon's ability to host more lithium atoms per silicon atom, and it is this ability that inherently leads to a volume expansion of 280%. As silicon is lithiated, the bonds of the initial structure are broken to accommodate more lithium. Volume expansion is highly detrimental to the cycling performance of Li-ion cells and is a major barrier towards to commercial adoption of silicon-based negative electrodes.[15] Volume expansion can lead to loss of particle-to-particle contact, constant interruption of the solid electrolyte interphase formation, and a multitude of macroscopic scale issues.[16,17] Increased expansion (during lithiation) and contraction (during de-lithiation) lead to lithium loss, reduced cell life, and decreased cell performance.

Other than volume expansion, the formation of a crystalline lithiated silicon phase ($Li_{15}Si_4$) at low potential (< 50 mV) also hinders the cycling performance of pure silicon cycled to full capacity.[18,19] $Li_{15}Si_4$ formation is shown to be correlated with capacity fade.[19] The de-lithiation of $Li_{15}Si_4$, induces a two-phase reaction where amorphous Li_2Si is formed. The further de-lithiation of amorphous Li_2Si is uniform, eventually forming amorphous silicon. A representation of the lithiation and delithiation of silicon is shown in Figure 1.6. The two-phase reaction that occurs during $Li_{15}Si_4$ delithiation results in the co-existence of different phases with different molar volumes. This introduces a phase boundary with induced stress on the material. The stress at the phase boundary can cause fracturing of the alloy electrode material leading to loss of electrical contact and capacity fade.[12]

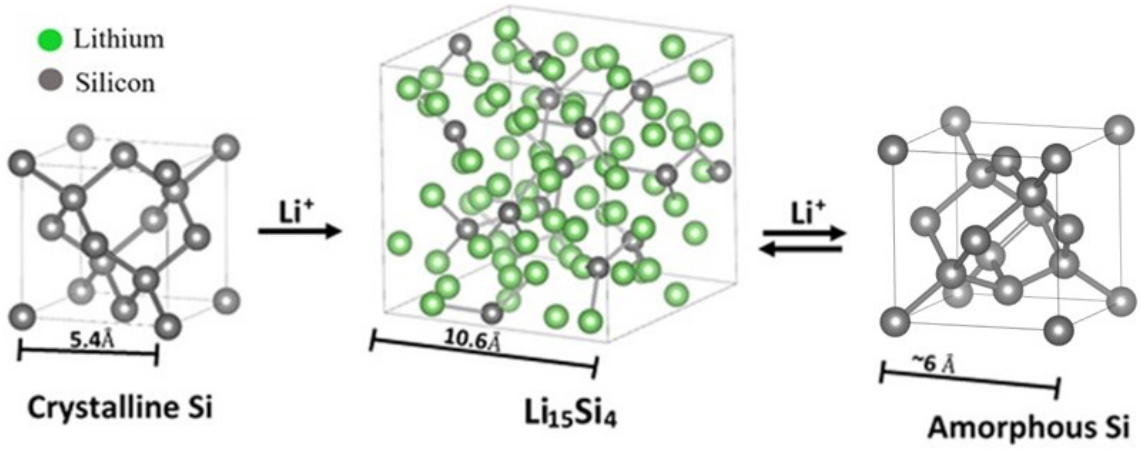

Figure 1.6. Visual representation of the electrochemical lithiation of silicon on a unit cell scale. Note that on the scale of a unit cell, local order is maintained in amorphous Si, while long range order is lost. Therefore, the amorphous Si unit cell only shows small perturbations compared to the crystalline Si unit cell.

One method used to overcome the limitations of pure Si is to alloy Si with an electrochemically inactive material.[12,15,20,21] Inactive material reduces the volume expansion of the alloy to a desired percentage by diluting the volume expansion since inactive material will not expand.[21] It is counterintuitive to give valuable space in the negative electrode to electrochemically inactive materials, but many positive effects are given from this process. Introducing electrochemically inactive elements into alloy materials mitigates the effects of volume expansion while lowering the average discharge potential at a given volume expansion (see Figure 1.7).

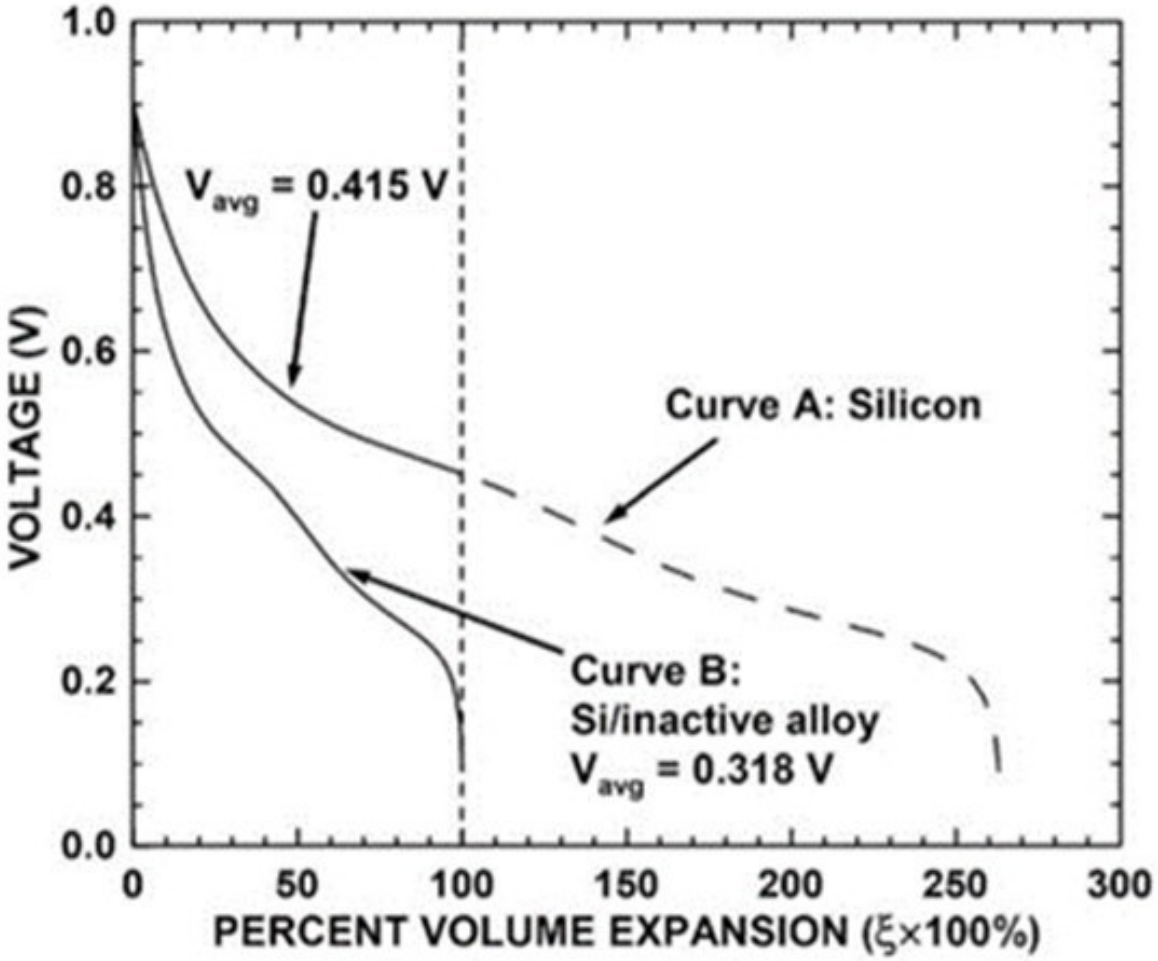

Figure 1.7. The voltage curves (vs lithium metal reference electrode) vs percent volume expansion during the delithiation half-cycle. Curve A is pure silicon and Curve B is an alloy of 36% active silicon/64% inactive component by volume.[21] Reproduced with permission from Reference 21.

As shown in Figure 1.7 the voltage verses the percent volume expansion shows that a given alloy with a volume expansion at full lithiation that is less than 280% has a lower average voltage than pure Si cycled to the same volume expansion. Therefore, Si-inactive alloys have an increased energy density at a given percent volume expansion.[21] A research goal in Si-inactive alloys is to find ideal inactive elements to alloy with Si and increase the performance of a Li-ion cell. Si-inactive alloy negative electrodes also have the additional advantage of suppressing the formation of crystalline $Li_{15}Si_4$ phase. When Si is incorporated into a matrix of

inactive material the two-phase reaction and phase boundary stress associated with $Li_{15}Si_4$ phase formation is avoided, leading to improved cycling performance.[22] The compressive stress experienced upon lithiation of Si within an inactive material matrix decreases the potential at which lithium forms an alloy which also decreases the potential at which $Li_{15}Si_4$ forms to below 0 V vs Li.[23,24]

1.2.4 Electrolyte Solution

The electrolyte solution (light blue shown in Figure 1.1) allows Li-ion transport between the positive and the negative electrode while being electrically insulating, so the cell does not short. The typical electrolyte solution in a Li-ion cell consists of a combination of organic carbonates and a lithium salt. Organic carbonates have good film forming properties, relatively low viscosity, high ionic conductivity, and generally operate within a large potential window. An ideal electrolyte solvent has a high dielectric constant, low viscosity, wide potential range, and is able to operate over a wide temperature range.[25] No perfect solvent exists, so a typical electrolyte solvent is a blend of organic carbonates whose properties balance out to create an optimized solvent. An electrolyte solution's ionic conductivity originates from the dissolved lithium salt. When choosing a lithium salt, the properties desired are high conductivity, ionic mobility, thermal stability, and chemical stability, as well as a large dissociation constant.[25] Lithium hexafluorophosphate ($LiPF_6$) is a popular lithium salt used in Li-ion electrolytes. Its well-balanced characteristics suit many applications; however, it is not a perfect salt. $LiPF_6$ unfortunately has poor thermal and chemical stability.[26] There is fortunately a wide collection of lithium salts of interest for lithium-ion cells, and a salt can be chosen whose properties match the application well. Another important ingredient of Li-ion battery electrolyte solutions is electrolyte additives. Additives, accounting for less than 10% by weight of the solvent, assist

in the formation of the SEI, tuning the morphology and composition to an optimized performance.[27] Additives are often reduced or oxidized before the rest of the electrolyte, facilitating the formation of a passivating layer between the electrodes and electrolyte, limiting further reaction and loss of lithium.

1.2.4.1 Solvents

As mentioned above, an electrolyte solvent is typically a mixture of organic solvents optimized to have a high dielectric constant (to dissociate the lithium salt), a low viscosity (to maximize ionic conductivity), and be stable over a large temperature range and potential window. There currently is no single solvent meeting all the requirements, so in order to achieve a desired set of properties, solvents are mixed at ratios that give a maximized performance. For example, the popular cyclic carbonate, ethylene carbonate (EC) has a high dielectric constant but unfortunately it is a solid at room temperature and greatly increases electrolyte solution viscosity when used in high amounts. To get the beneficial properties of EC while balancing out its negative properties, EC is mixed with a linear carbonate solvent such as diethyl carbonate (DEC) which lowers the solution's viscosity.[28] There are other solvents to choose from as well, such as ethyl methyl carbonate (EMC) and dimethyl carbonate (DMC) (Figure 1.8).

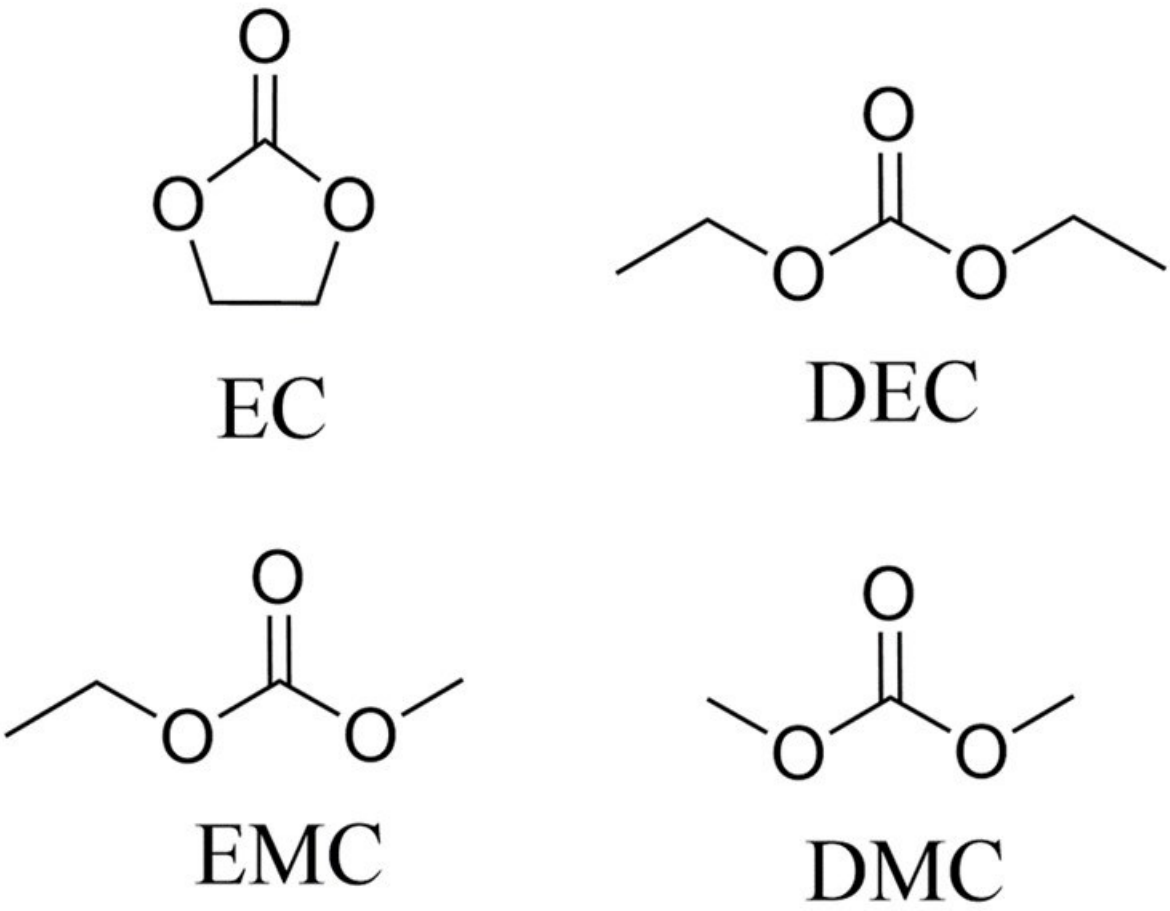

Figure 1.8. Chemical structure of organic carbonates EC, DEC, EMC, and DMC. Commonly used solvents for electrolytes in Li-ion cells.

A graphite negative electrode's exceptional cycling performance relies on EC's film forming properties, forming a stable SEI layer in the initial cycles.[29,30] SEI formation on graphite is said to follow two different steps; the solvent co-intercalation and decomposition beneath the surface at ~1 V and direct decomposition of solvents on the basal plane at lower potentials to form a precipitate layer.[30,31] Solvent co-intercalation is when the solvent that is shuttling the Li-ion intercalates into the electrode with the Li-ion rather than dissociating from the ion as it should. Solvent co-intercalation is generally harmful to a graphite electrode because it can lead to exfoliation of graphene layers, stripping active material and reducing the capacity of the electrode. However, solvent co-intercalation is important in the initial stage of SEI formation

on graphite in EC-based electrolytes.[30] The co-intercalated EC decomposes to form an immobile product between the graphene layers that prevents further solvent co-intercalation, preventing exfoliation of graphene layers in further cycles. This process is illustrated in Figure 1.9.

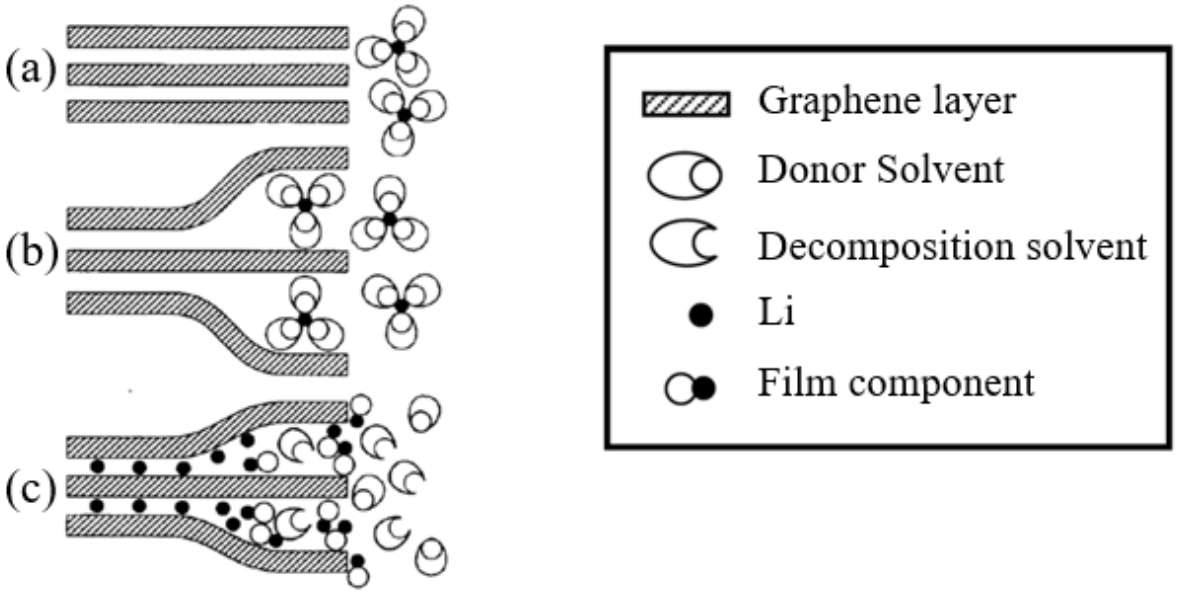

Figure 1.9. Solvent co-intercalation model for SEI formation on graphite proposed by Besenhard et al. (a) is before reaction, (b) is the intercalation of $Li_x(solvent)_y$ into graphite, and (c) is the internal decomposition of $Li_x(solvent)_y$ and film formation.[30] Reproduced with permission from Reference 30.

1.2.4.2 Electrolyte Salts

The use of lithium salts in the electrolyte solution of a Li-ion cell gives the solution its ionic conductivity and allows for the transport of Li-ions between the positive and the negative electrodes. Lithium salts come with a variety of properties, so different applications could require the use of various salts. Ideally, lithium salts for use in electrolyte solutions have high ionic conductivity and mobility to ensure optimal Li-ion diffusion. The salt ought to have a high dissociation constant and have wide thermal and chemical stability range. The most

common salt in organic carbonate-based electrolytes is $LiPF_6$, which is highly soluble and has high ionic conductivity and mobility. However, $LiPF_6$ lacks thermal and chemical stability, thermally dissociating at temperatures above 60 °C.[26] There is a wide collection of lithium salts to choose from, some popular $LiPF_6$ alternatives are lithium bis(oxalato)borate (LiBOB), lithium difluoro(oxalato)borate (LiDFOB), and lithium bis(trifluoromethanesulfonyl)imide (LiTFSI). These mentioned salts can be utilized solely or blended and are shown in Figure 1.10.

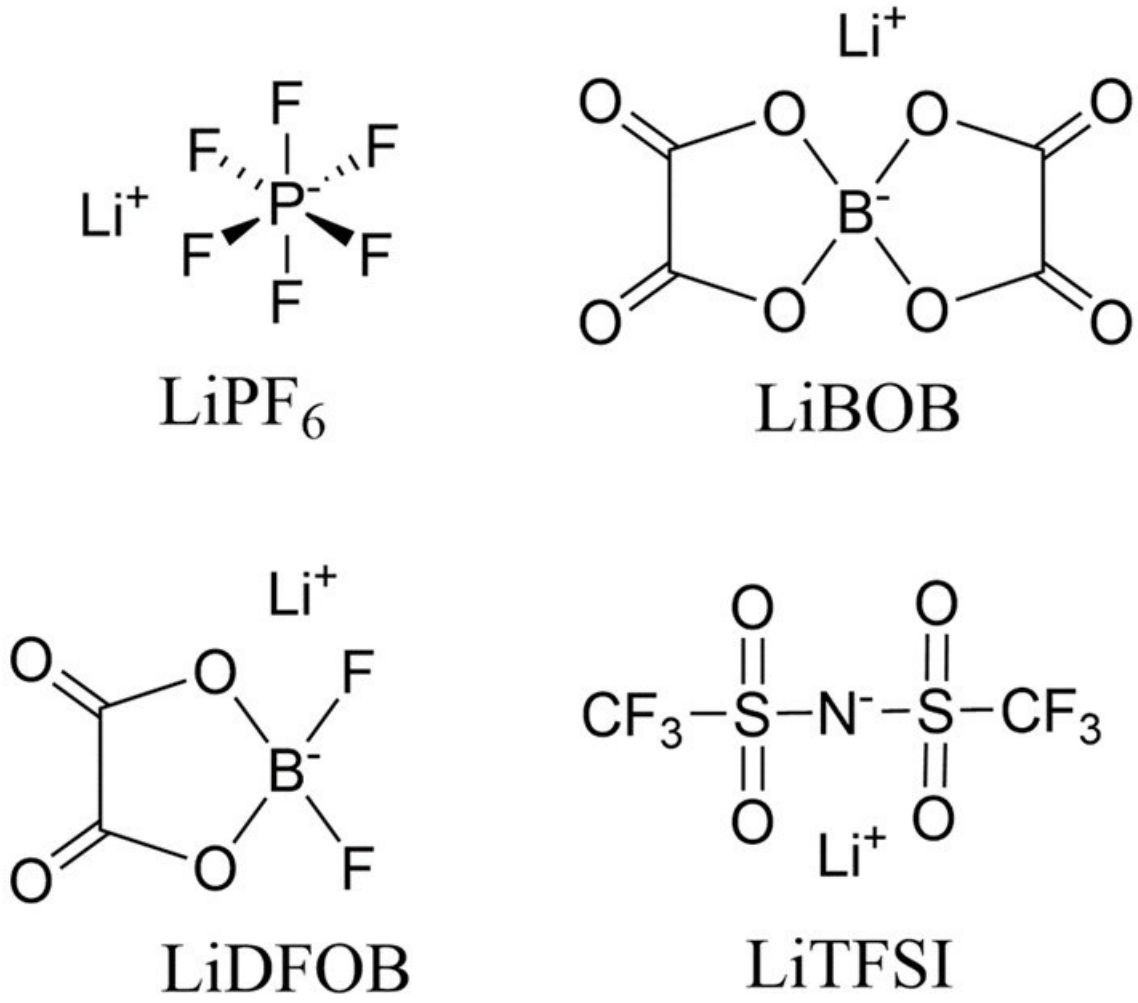

Figure 1.10. Structures of lithium salts $LiPF_6$, LiBOB, LiDFOB, and LiTFSI. Commonly used as salts for electrolytes in Li-ion cells.

The thermal instability of $LiPF_6$ would make it a bad choice for cells operating in temperatures over 60 °C. For an example, in this higher temperature application, it may be more suitable to use LiTFSI. LiTFSI has higher thermal and chemical stability compared to $LiPF_6$, decomposing on lithiated graphite only at temperatures around 170 ℃.[32,33] LiTFSI also has a higher dissociation constant but can corrode the aluminum positive electrode current collector in the right environment.[33] Although there may not be a perfect, one-size-fits-all salt for Li-ion cell electrolytes, there are fortunately many to choose from. The choice of lithium salt, like most commercial applications, is also often governed by the cost.

1.2.4.3 Additives

SEI formation during the initial charge of a Li-ion cell is crucially important towards the cycle life and performance of the cell. Components that are more readily reduced or oxidized will be the first to react at the electrode surfaces, this a property by which electrolyte additives are selected. Additives account for less than 10% the weight of the solvent, yet their presence in an electrolyte system can drastically alter a cells performance and lifetime.[27] Aiding in the modification of the morphology and composition of the SEI, additives have a tremendous importance in the electrolyte. Additives are often reduced or oxidized more readily than the rest of the electrolyte, meaning their decomposition contributes to the SEI formation before the decomposition of the rest of the electrolyte to limit reactions with the electrodes and lithium loss. For example, monofluoroethylene carbonate or fluoroethylene carbonate (FEC) is a popular additive that has been shown to produce an SEI composed predominantly of lithium fluoride (LiF).[34] It was found that LiF provides an extra Li source, lowers the initial irreversible capacity, suppresses electrolyte side reactions, and enables faster Li-ion transport.[6,35] A SEI rich in LiF is also more compact than an SEI with less, so the additive FEC can give these

benefits while reducing SEI thickness.[36] Repeated volume expansion in previously mentioned Si-alloys can lead to continual disruption and formation of the SEI, depleting electrolyte salts and solvents. This continuous formation will lead to capacity fade as more Li is consumed by SEI formation, possible isolation of active material, and overall poor cell performance.[37] FEC is used in cells containing Si-alloy negative electrodes to prevent electrolyte salt and solvent decomposition by forming an SEI layer that is thinner, more stable, and does not continuously grow.[37,38]

FEC is of course not the only additive in use today, there are a plethora of additives to choose from. Some common electrolyte additives include vinylene carbonate (VC), 1,3,2-dioxathiolane-2,2-dioxide (DTD), and methylene methanedisulfonate (MMDS). These mentioned additives are shown in Figure 1.11.

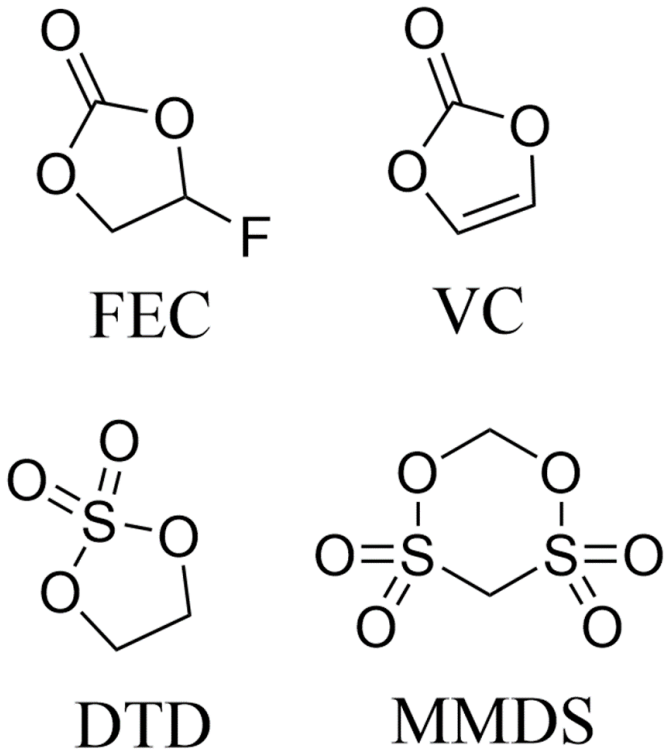

Figure 1.11. Chemical structure of additives FEC, VC, DTD, and MMDS. Commonly used additives for electrolytes in Li-ion cells.

The reduction potential of an additive is correlated to its lowest unoccupied molecular orbital (LUMO) energy, so a favourable additive for the negative electrode SEI should have a low energy LUMO.[39] The oxidation potential of an additive is correlated to its highest occupied molecular orbital (HOMO) energy, so a favourable additive for the positive electrode interface should have a higher energy HOMO.[39] Choosing an additive is similar to the process of choosing solvents and salts, it comes down to the desired application and a combination of various additives. A major downside of additive use is the increased cost to develop an electrolyte.

1.3 Solid Electrolyte Interphase (SEI)

Lithium and lithiated electrodes are known to be thermodynamically unstable when exposed to electrolyte, and yet some Li-ion cells have a service life of several years. When electrodes are charged in an electrolyte solution, rather than fully reacting until all the electrolyte is decomposed, the electrodes form a passivating film that slows the reactions. This passivating film is the SEI, a heterogeneous structure comprised of various salts, carbonates, phosphates, and polymers that forms via the decomposition of electrolyte additives, solvents, and salts during the first few cycles of a Li-ion cell. Both electrodes react with the electrolyte during the first charge, some of the by-products of these initial reactions will precipitate onto the surfaces of the electrodes. This film created by the precipitated by-products is electronically insulative, thus preventing further reaction, but fortunately the film is ionically conductive to allow the transport of Li-ions into and out of the electrodes. Li-ion transport through the SEI is mainly via mobile point Frenkel or Schottky defects.[5,40] The SEI concept was first introduced by Emanuel Peled in 1979, though there are a variety of compositions it can possess, its role in the

life and performance of Li-ion cells is undisputed.[5,41] A very popular representation of the SEI on lithium metal or carbon electrode suggested by Peled et al. is shown in Figure 1.12.

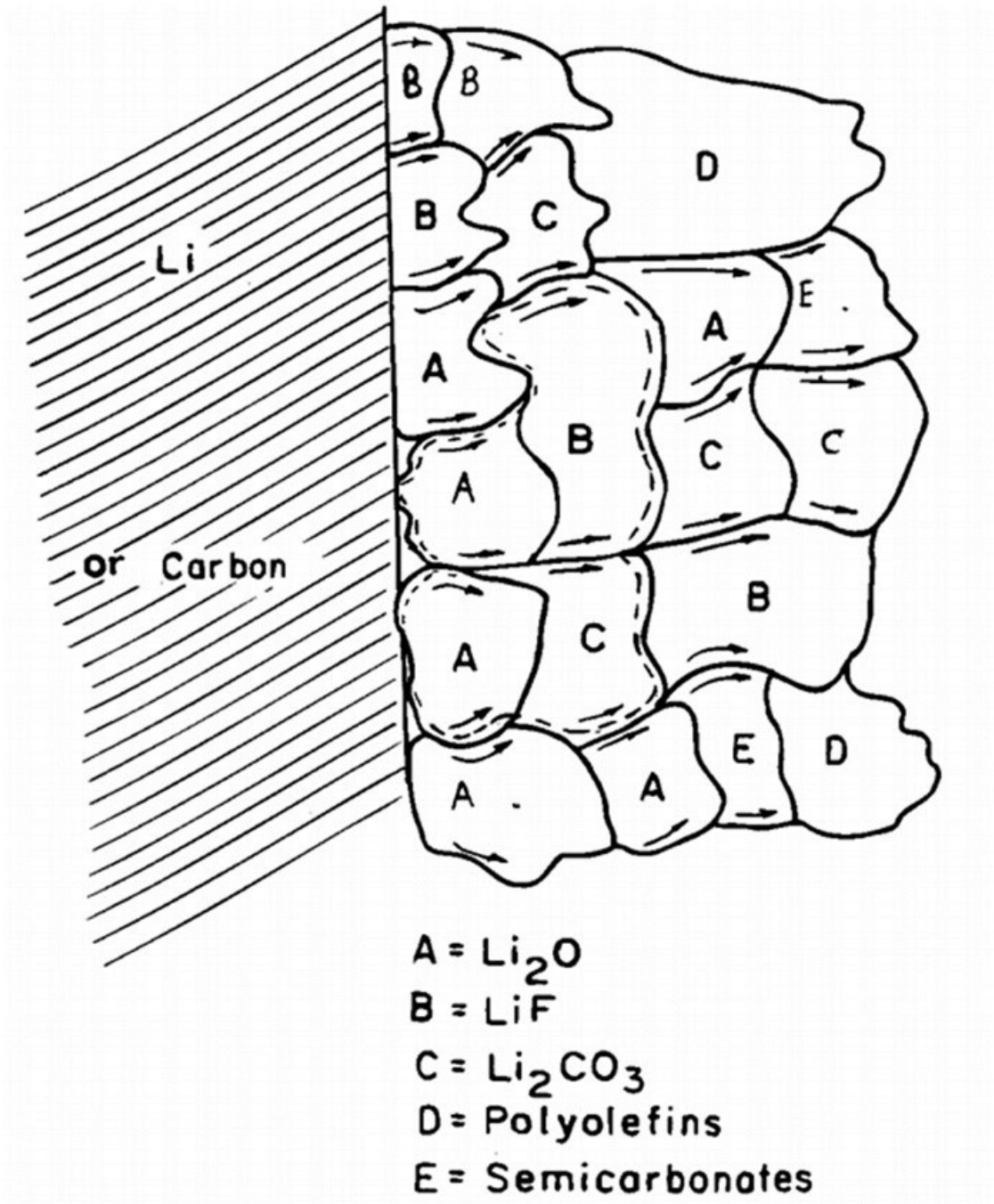

Figure 1.12. Schematic representation of a heteropolymicrophase structured SEI on lithium or carbon electrode. [41] Reproduced with permission from Reference 41.

Since the SEI is so important for cell performance, it has been studied intensively and various methods of modifying its structure and composition were explored. There are many interesting methods of manipulating the SEI including the use of electrolyte additives, the coating of electrode particle surfaces, and even going so far as to create an artificial SEI all together.[42] In the common organic carbonate-based electrolyte some combination of LiF, Li_2CO_3, polyolefins, Li_2O, semi-carbonates, lithium alkoxides, nonconductive polymers, and more reaction products are expected to form on electrode surfaces.[41] This SEI model introduced by Peled is the most well known and accepted model for this passivation layer but other models have been proposed such as the polymer-electrolyte interphase (PEI) model, the solid-polymer-layer (SPL) model, and the compact-stratified layer (CSL) model.[43] Regardless of the model used, there is a form of passivating layer at the negative electrode/electrolyte interphase that is absolutely crucial to the workings of a Li-ion cell and a similar layer formed at the positive electrode/electrolyte interphase. Both interphases deserve attention and understanding their formation will allow the preferential modification needed to increase the overall performance of future Li-ion cells.

1.3.1 Negative Electrode/Electrolyte Interphase in Standard Electrolyte

The SEI is difficult to characterize due to its sensitive and complicated composition. However, there are methods of characterizing the SEI surface such as x-ray photoelectron microscopy (XPS) and methods of probing its electrochemical performance such as electrochemical impedance spectroscopy (EIS).[44–46] The SEI on negative electrodes has been studied extensively, as it is an integral part of the cell's performance. The negative electrode/electrolyte interphase forms this passivating SEI to protect the electrolyte from fully decomposing on the electrode, its composition as discussed above includes inorganic and organic compounds that

originate from the reduction of electrolyte components. Figure 1.13 depicts the reactions that occur on graphite to form the SEI in a standard electrolyte system.

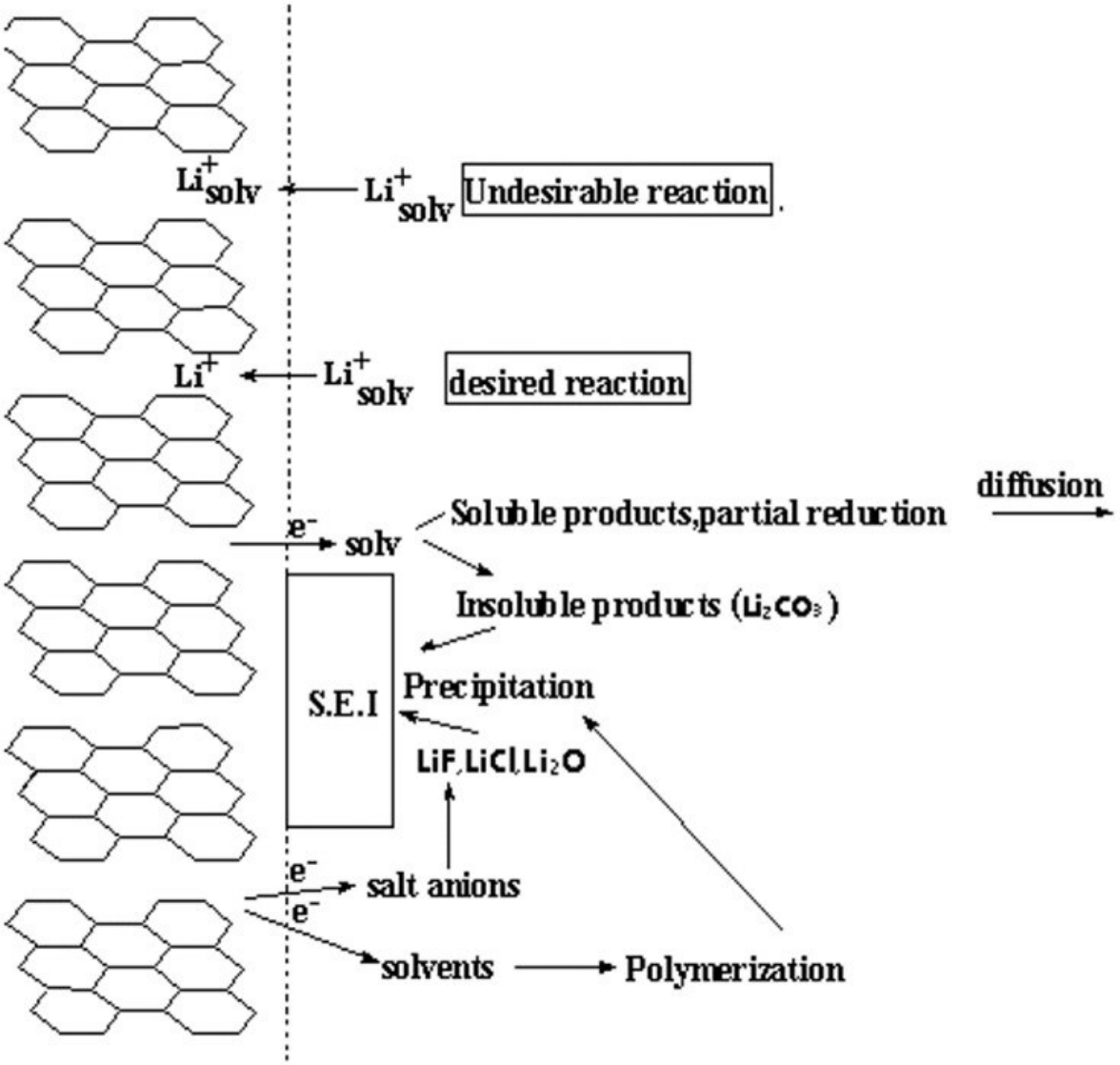

Figure 1.13. Diagram showing the formation of the SEI on graphite electrode.[5] Reproduced with permission from Reference 5.

The formation of the SEI depends on the electrode material, solvent, salts, and additives used in electrolytes, and other environmental factors such as temperature. Elevated temperatures lead to increased reactivity of the SEI and thus accelerated capacity fade.[47,48] SEI composition varies according to depth. It has been proposed that closer to the electrode the SEI is richer in

inorganic compounds and closer to the electrolyte the SEI is richer in organic compounds.[41,49] Peled et al. studied the reaction products formed on highly oriented pyrolytic graphite (HOPG) and found that the SEI on the graphite's edge plane was richer in inorganic compounds while the graphite's basal plane was richer in organic compounds.[50,51] This shows that factors other than the electrolyte chemistry effect the formation of the SEI.

EC is an important film forming component, aiding in the successful formation of an SEI on graphite.[28,30] Solvent co-intercalation from EC-based electrolytes is important for SEI formation on graphite. Co-intercalated EC decomposes between the graphene layers to form an immobile product that prevents later solvent co-intercalation, thus preventing exfoliation of graphene layers in future cycles.[30] After the initial co-intercalation, precipitates formed by the reduction of electrolyte at the electrodes surface will form the passivating layer that is considered the SEI. LiF and Li_2CO_3 are generally accepted as major components of a SEI on a graphite electrode in EC-based electrolytes with $LiPF_6$ salt.[39] Wu et al. used LiF as a surface modifier for graphene and observed increased cycle life and rate capability.[6] It was shown that the LiF provides an additional Li source, lowering the initial irreversible capacity and reducing SEI thickness. Using density functional theory (DFT), Y. X. Lin et al. observed that a layer of LiF as thin as 2 nm could prevent electron tunneling from a lithium electrode, while Li_2CO_3 required 3 nm.[52] A SEI comprising LiF is formed thinner and results in faster Li-transport.[6] As discussed in the additives section, electrolyte additives are used in small quantities to modify the composition and morphology of the SEI. Fluorinated electrolyte additives like FEC are commonly used to form a thinner more stable SEI layer, richer in LiF.[35,53] The SEI formation on negative electrode is crucial for the safety, lifetime, capacity retention, and overall performance of Li-ion cells.

1.3.2 Positive Electrode/Electrolyte Interphase in Standard Electrolyte

Positive electrode surface chemistry has historically received less attention relative to the extensive studies of the negative electrode. It has been shown that the impedance of the positive electrode increases upon cycling and during storage which indicates the formation of a surface film or the modification of the active electrode surface. The positive electrode/electrolyte interphase forms a similar film to slow the reactions between the electrolyte and the electrode, its composition originates from the oxidation of electrolyte components during early cycling. It was observed that commonly used solvents in Li-ion cells are not electrochemically stable at potentials higher than 3.5 V and oxidize while the lithium salts remain unoxidized at potentials as high as 5 V.[54] Though the salts may remain stable at elevated potentials, some lithium salt will still react with the formed interphase by first reacting with impurities and forming precipitating products. For example, $LiPF_6$ reacts with trace water via equations 1.1, 1.2, and 1.3 to form products that interact with the positive electrodes surface.[55]

$$LiPF_{6\,(d)} \leftrightarrow LiF_{(d)} + PF_{5\,(d)} \tag{1.1}$$

$$PF_{5\,(d)} + H_2O_{\,(d)} \rightarrow HF_{(d)} + PF_3O_{\,(d)} \tag{1.2}$$

$$PF_3O_{\,(d)} + ne^- + nLi^+_{(d)} \rightarrow LiF_{(s)} + Li_xPOF_{y\,(s)} \tag{1.3}$$

When studying spinel $LiMn_2O_4$ positive electrode material, it was found that the amount of surface material present increased with cycle number.[56] This indicates that the film formed on $LiMn_2O_4$ is not sufficiently dense to serve as a fully passivating layer between the electrolyte and electrode. In the case of the positive electrode/electrolyte interphase, electrolyte is able to continually transport to the electrode surface and oxidize.[56,57] Ideally, this is not the case with the negative electrodes SEI. The negative electrodes SEI fully passivates the electrode surface to prevent further reduction of the electrolyte during cycling, but the positive

electrode/electrolyte interphase allows for the continual oxidation of electrolyte, not fully passivating the electrode. This key distinction leads to the film formed at the positive electrode surface being referred to as a Solid Permeable Interface (SPI) rather than a SEI.[58] It is generally accepted that the composition of the SPI is similar to that of the SEI but in addition to the ways that the SEI is important for cell performance, the SPI can also limit cell performance by decomposing electrolyte continuously during cycling.

1.4 Overview

This thesis examines how SEI formation may be modified in ways not normally considered: by incorporating solid additives that affect SEI formation directly in active materials, utilizing water as a beneficial electrolyte additive (normally considered detrimental to cell performance), and utilizing binder additives to modify SEI formation. Chapter 2 explains the experimental techniques used in the work of the following chapters. The fundamental theory behind each technique will be introduced as well as a description of how the techniques were used in this work. Chapter 3 introduces the use of solid phase electrode additives. In this work, LiF and Li_2CO_3 are investigated as components in Si-Fe alloys that can modify the SEI and lead to improved cycling. Chapter 4 focuses on the effects of synthesized poly-VC being used as a binder additive to modify SEI formation in Si-Fe alloy electrodes. Chapter 5 highlights the use of water as an electrolyte solution additive to improve cycling in nickel manganese cobalt (NMC)/silicon alloy and lithium cobalt oxide (LCO)/silicon alloy full cells.

CHAPTER 2. EXPERIMENTAL METHODS

2.1 Mechanical Alloying

Mechanical alloying is the process of developing powdered materials with extremely fine and controlled microstructures. Mechanical alloying is commonly used in powder metallurgy where homogeneous amorphous powers are produced by repeated plastic deformation, cold welding, and particle fracturing in a high-energy environment.[59] The type of mechanical alloying used in this work is ball milling, where the powders are milled in a hardened steel vial and the milling media used is stainless steel balls. The steel vials are placed in a milling machine that shakes the sample so that the powders coat the surfaces of the steel balls and are smashed into the walls of the container as well as into other balls.

During milling, every collision between the balls and the wall traps and plastically deforms or fractures some powder. Particle fracturing results in the formation of fresh reactive surfaces without a passivating layer. This can lead to the cold welding of metal particles. These cold-welded particles can succumb to further particle fracturing, eventually leading to amorphization.[60,61] The grain size of the produced alloys decreases with increased milling time and the final grain size is reached when there is a balance between dislocation and recrystallization.[59,61]

In this work, a total of 0.5 ml of precursor powder was loaded into a 65 ml hardened steel milling vial (SPEX, model 8000-D, Spex CertiPrep, Metuchen, NJ) along with 180 g of 1.6 mm stainless steel balls and sealed under an argon atmosphere. The volume of the sample was 0.5 ml (based on true density), which was determined in previous studies to be the desirable amount to form a thin layer of powder on the surfaces of the milling balls of optimal thickness

to make milling efficient.[61] The vials are sealed with steel caps that have an O-ring seal, so the vial environment remains argon.

2.1.1 Two-Step Method

In some compositions prepared in this thesis, inorganic phases (LiF and Li_2CO_3) were introduced as Si-alloy components. The introduction of inorganic phases into the milling process resulted in incomplete amorphization of the Si phase. Having an amorphous Si-alloy is important for maintaining homogenous lithiation of the alloy particles during cell cycling. To enable the incorporation of inorganic phases in Si-alloys while achieving complete amorphization of the Si phase, a two-step ball milling procedure was developed. For $Si_{40'}(FeSi_2)_{(60-x)'}(LiF)_{(x)'}$ and $Si_{40'}(FeSi_2)_{(60-x)'}(Li_2CO_3)_{(x)'}$ alloys, the two-step ball milling procedure involved milling Si and Fe first for 8 hr. This first step resulted in the formation of $FeSi_2$ and the amorphization of excess Si. Then as a second step, LiF or Li_2CO_3 was added, and the mixture was milled for an additional 8 hr. This ensured the incorporation of all the components while reaching the desired amorphous level.

2.2 Electrode Preparation

Electrode slurries in this work were prepared by mixing a 70:5:25 weight ratio of alloy:carbon black (Imerys Graphite and Carbon, Super C65): binder in an appropriate slurry solvent. For some electrodes the binder/slurry solvent was an aromatic polyimide (PI)/n-methyl-2-pyrrolidinone (NMP, 99.5%, Sigma-Aldrich) where the polyimide was added in the form of a 20% (w:w) solution of poly(amic acids) in NMP (Hitachi DuPont MicroSystems, LLC). Slurries were mixed with a high-shear mixer equipped with a Cowles blade for 10 min at a rotational frequency of 5000 rpm. Electrode slurries were coated onto electrolytic copper foil

(Furukawa Electric, Japan) to a slurry thickness of 0.102 mm using a stainless-steel coating bar and dried at 120 °C for 1 h. 1.3 cm^2 electrode disks were cut from the coatings. Electrodes with PI binder were subsequently cured by heating at 300 °C for 4 h under flowing argon, as described by B. N. Wilkes et al. in reference 5.[62]

2.3 Electrochemical Characterization

Electrodes were assembled into 2325-type coin cells and cycled with a lithium foil counter/reference electrode. These coin cells were cycled at 30.0 ± 0.1 °C between 0.005 V and 0.9 V with a Maccor Series 4000 Automated Test System at a C/10 rate for the first cycle and C/5 for subsequent cycles. To replicate CCCV full cell charging, cells were held at 5 mV at the end of each cycle until a current limit of C/20 was reached. C-rates were established based on the theoretical 3579 mAh/g active Si capacity.[12] Fade rate was defined as the average percent capacity fade per cycle between cycles 10 and 80.

2.3.1 Cell Construction

Electrodes were placed into 2325-type coin cells with a lithium foil counter/reference electrode separated by one layer of Celgard 2300, a layer of blown polypropylene microfiber (BMF) separator (3 M Co.), and another layer of Celgard 2300 in that order (shown in Figure 2.1.).

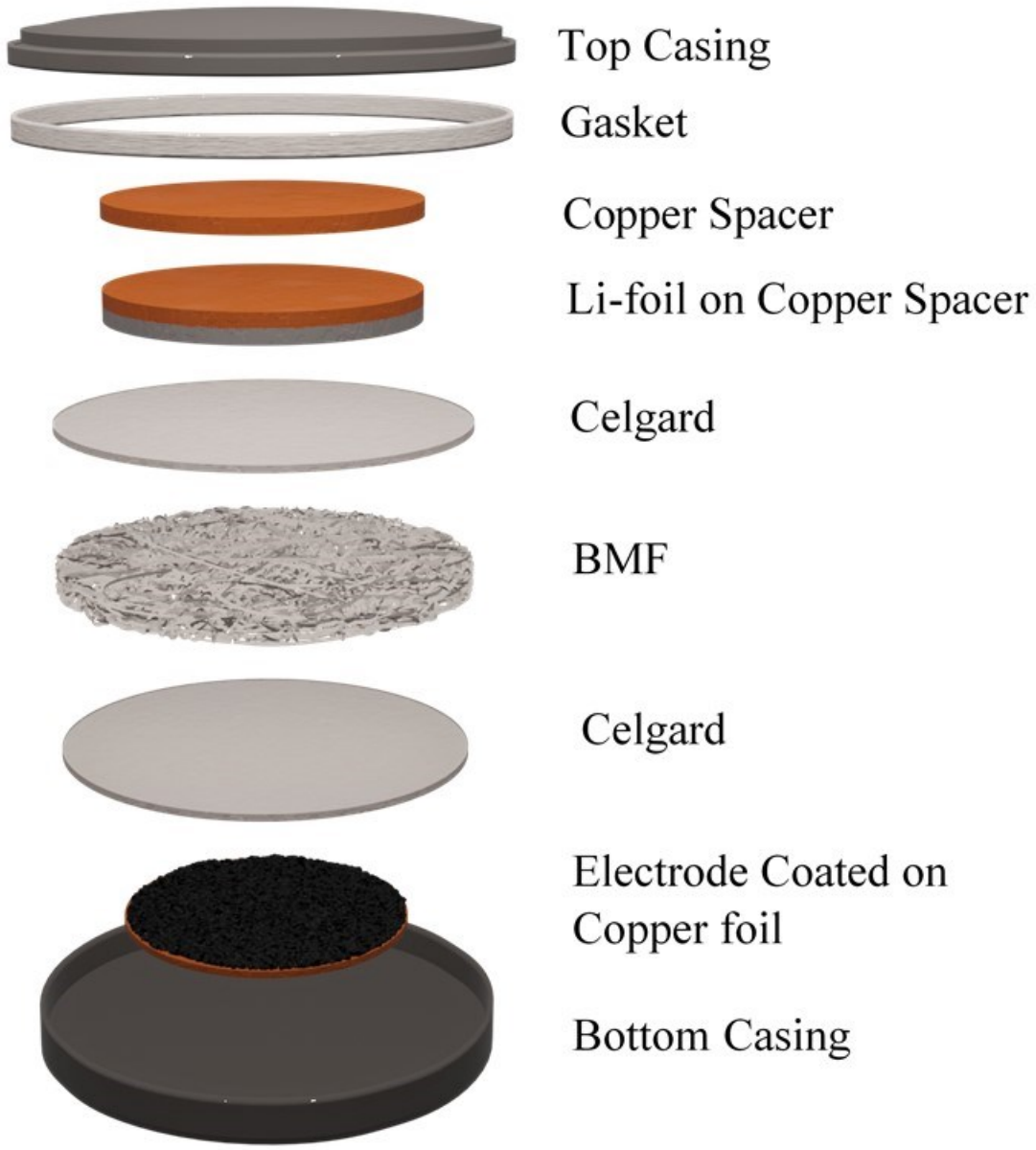

Figure 2.1. Deconstructed view of a typical 2325-type coin cell.

Cells were assembled in an Ar-filled glove box using 100 µl of electrolyte. Electrolyte consisted of either 1M LiPF6 (BASF, 99.94%, water content 14 ppm) in (v:v) (3:6:1) ethylene carbonate (EC):diethyl carbonate (DEC) (BASF, 98%, water content < 50 ppm):fluoroethylene carbonate (FEC) (BASF, >99.94%) or 1 M LiPF6 in (v:v) EC:DEC (1:2).

2.3.2 Symmetric Cells

Symmetric cells were assembled in 2325-type coin cells with two identical electrodes separated by two layers of Celgard 2300 and one layer of blown polypropylene microfiber (BMF). One of the electrodes was prepared in a lithiated state, while the other was in a delithiated state, as follows. The delithiated electrode was assembled into a Li-half cell and then lithiated to a potential of 0.005 V and then delithiated to 0.9 V at a rate of C/20. The lithiated electrode was also assembled into a Li-half cell and then lithiated to a potential of 0.005 V, delithiated to 0.9 V at a rate of C/20 and then lithiated to 0.005 V at a C/5 rate and held at this potential until the current dropped below C/20. After these cycling regimes, the cells were disassembled in an Ar-filled glove box, the lithiated and delithiated electrodes were recovered and were subsequently assembled into symmetric cells.

2.4 Scanning Electron Microscopy

Scanning electron microscopy (SEM) is a technique used for investigating materials that are too small to be effectively observed by optical microscopy. A cutaway image of a SEM is shown in Figure 2.2. An image is generated by scanning the sample with a focused beam of electrons and capturing the scattered electrons in detectors. Electrons are produced by running an electric current through a tungsten filament and accelerated towards the sample through a potential difference from the source to the emitter. These generated electrons interact with the sample, scattering to produce various signals that give information about the surface composition and topography of the sample. SEM images are produced from one of two scattering types, by the detection of secondary electrons (SE) or of backscattered electrons (BSE). SEM images in this work were obtained with a TESCAN MIRA 3 field emission SEM

using a 5.0 kV accelerating potential. Both SE and BSE images were collected pre- and post-cycling.

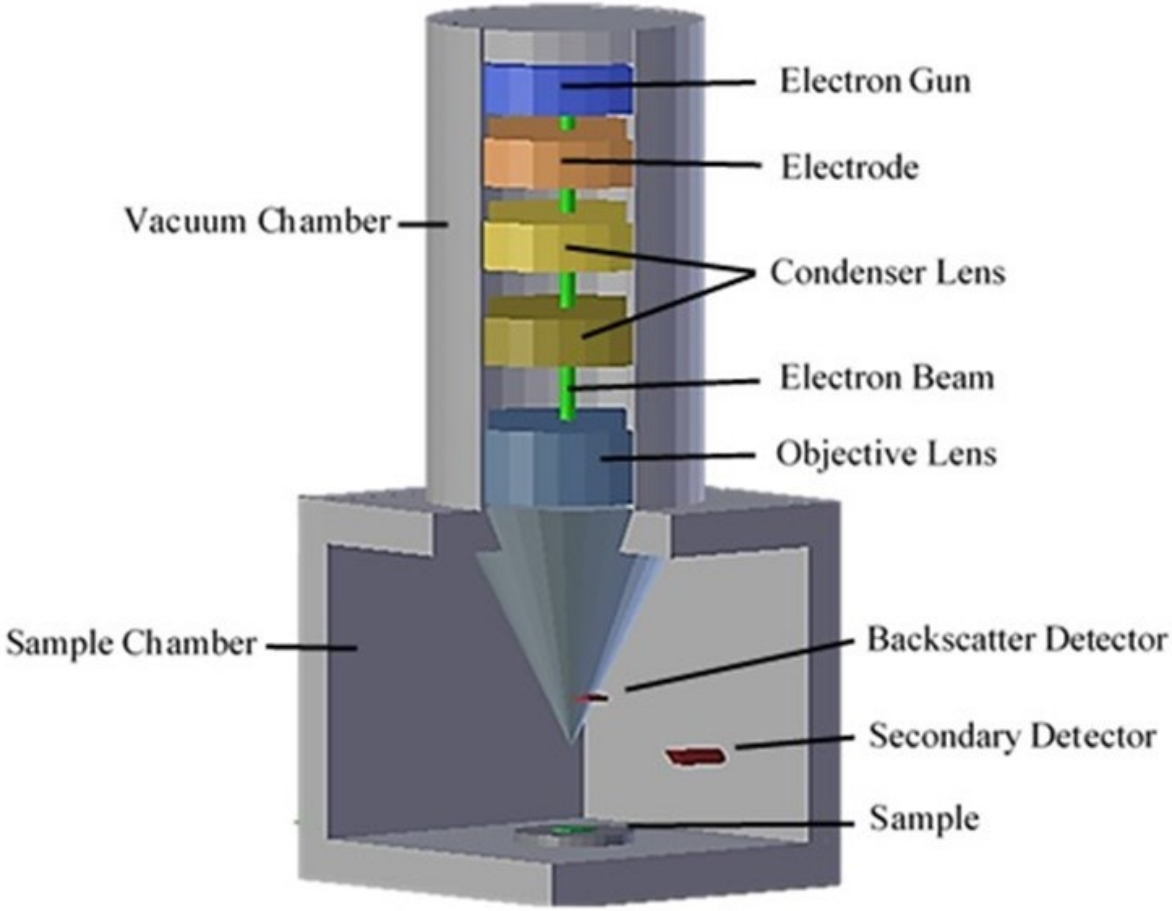

Figure 2.2. Cutaway schematic of a typical SEM.

2.4.1 Secondary Electrons (SE)

When an SEM sample interacts with the focused electron beam, the atoms in the sample can become ionized. In this process low-energy electrons are emitted from the sample surface. These electrons are guided towards a detector with a potential bias to generate a SEM image of the sample's topography. Electrons excited in this fashion are defined as secondary electrons (SE), which conventionally have an energy less than 50 eV.[63] During inelastic scattering, energy transferred from the focused electron beam to the sample can result in an ejection of a

SE. SEs are primarily used for probing topographic properties like surface roughness because SEs are generated from regions near the samples surface and provide better lateral resolution than other electron sources.

2.4.2 Backscattered Electrons (BSE)

When the high energy electron beam meets the sample, both elastic and inelastic scattering can happen. The inelastic scattering results in an ejection of a SEs while elastic scattering produces backscattered electrons (BSE). Elastic scattering is present when the incident electron changes direction after colliding with the sample with negligible energy loss. BSEs conventionally have an energy greater than 50 eV and can have an energy close to the incident beam energy.[63] The intensity of BSEs in a given region can distinguish atomic composition of the sample because BSEs are incident electrons elastically deflected back from the sample surface. In this case, an atom with more electrons scatters more electrons back at the detector and the image will appear brighter in areas where the sample has atoms with more electrons. An atom with fewer electrons will appear relatively darker, as fewer electrons are scattered towards the detector, and thus the contrast can differentiate atomic composition throughout the sample. A BSE image is generated from regions that are usually deeper in the sample than SE images.

2.5 X-Ray Diffraction

X-ray diffraction (XRD) is an important non-destructive technique for characterizing the structure of crystalline materials using an incident X-ray beam. In an XRD measurement a sample is illuminated with an X-ray beam and the angles and intensities of the resulting diffracted X-rays are measured. A crystalline material can be thought to be made up of a series

of parallel lattice planes that intersect the points on the lattice. The lattice planes are separated by a distance d, which is referred to as the d-spacing. When the incident X-ray interacts with the sample it is scattered by the electrons of the atoms in the lattice planes. The diffracted X-rays can constructively interfere if the path difference between diffracted X-rays is equal to an integer number of wavelengths, creating a detectable scattered ray.

The conditions where diffracted X-rays constructively interfere is commonly called the Bragg condition, where at a particular angle (when the Bragg condition is met) a Bragg peak is located.[64] A schematic of X-ray diffraction satisfying the Bragg condition for constructive interference is shown in Figure 2.3. By measuring the intensity with varying incident angle, the angle of Bragg peaks can be detected and correlated to the d-spacing of the lattice planes in the sample. The relationship between Bragg peak angle and d-spacing is given in the Bragg equation (equation 2.1) where λ is the wavelength of the incident X-ray, θ is the incident angle, and n is an integer value.

$$n\lambda = 2dsin\theta \qquad 2.1$$

Each crystalline material has a unique set of parallel lattice planes that will give a pattern of Bragg peaks, creating a unique X-ray diffractions pattern for every material.

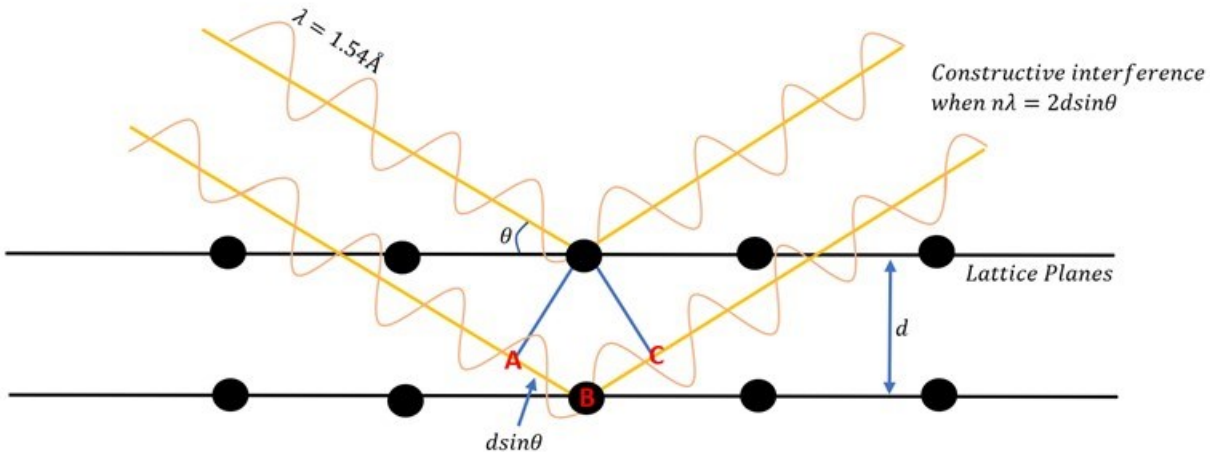

Figure 2.3. Schematic of X-ray diffraction and the conditions to satisfy the Bragg condition for constructive interference. The path difference between the two waves is ABC and the rays are in phase, so ABC is an integer multiple of λ.

X-rays are generated in a vacuum tube by irradiating a water-cooled electrode (typically made out of copper for laboratory X-ray diffractometers used for samples of inorganic compounds) with electrons generated by a tungsten filament. The electrons are accelerated toward the Cu electrode via a potential difference on the order of kilovolts. The electrons are accelerated such that they possess sufficient kinetic energy to knock an electron from the 1s orbital (K shell) of a Cu atom, on the order of kiloelectronvolts. Once a core electron is ejected, an electron from an outer shell must relax to a lower energy state to occupy the vacancy in the 1s orbital. This relaxation to a lower state is accompanied by a release of energy due to conservation of energy.

For Cu, there are two unique X-ray wavelengths emitted as the result of the electron transition from upper 2p and 3p orbitals (M and L shells respectively) to the 1s orbital. These electron transitions are referred to as Kα (2p→1s) and Kβ (3p→1s). These transitions have distinct wavelengths and intensities, Cu-Kβ radiation has a wavelength of 1.39225Å and Cu-Kα radiation ranges from 1.54060-1.54443Å.[65,66] The reason Cu-Kα is reported with a range is due to the degeneracy of the 2p orbital which has one higher energy orbital (2p1/2) and two lower energy orbitals (2p3/2). Due to the different energy of 2p electrons possessing different spin

states, Kα radiation is broken into Kα1 and Kα2 radiation. Kα1 and Kα2 correspond to 1.54060Å (2p3/2→1s) and 1.54443Å (2p1/2→1s), respectively.[65-67]

Kβ radiation is less intense than Kα radiation and is typically filtered from the diffracted X-ray to reduce the noise in the measurement. Kβ radiation is filtered from the diffracted X-ray beam by either using a Ni-filter or a diffracted beam monochromator. A Ni-filter will absorb the Kβ radiation, allowing the Kα radiation to pass through because the absorption edge of Ni is between the energy of Cu-Kα and Cu-Kβ radiation.[67] A diffracted beam monochromator is a single crystal placed in the path of the diffracted X-rays held at a fixed angle. The diffracted beam monochromator is set to an angle such that the Bragg condition is only satisfied at the Kα radiation wavelength, effectively blocking Kβ radiation (or any other radiations) from reaching the detector.

From the vacuum tube, incident X-rays pass through a divergence slit which is used to optimize the length of the X-ray beam reaching the sample. The incident X-ray then interacts with the sample, scattering from the electrons within the lattice, and constructively interfering when the Bragg condition is met. The diffracted X-rays then travel to the anti-scatter and receiving slits which reduce beam scatter and background noise while focusing the X-rays on the monochromator. The monochromator then allows only the Kα radiation to reach the detector.
The above description explains the setup for a Bragg-Brentano diffractometer, which was the XRD setup used in this work (depicted in Figure 2.4). With Bragg-Brentano geometry, the setup of a Bragg-Brentano diffractometer, the X-ray vacuum tube and detector move together along the measurement circle at the same rate and step size.[64]

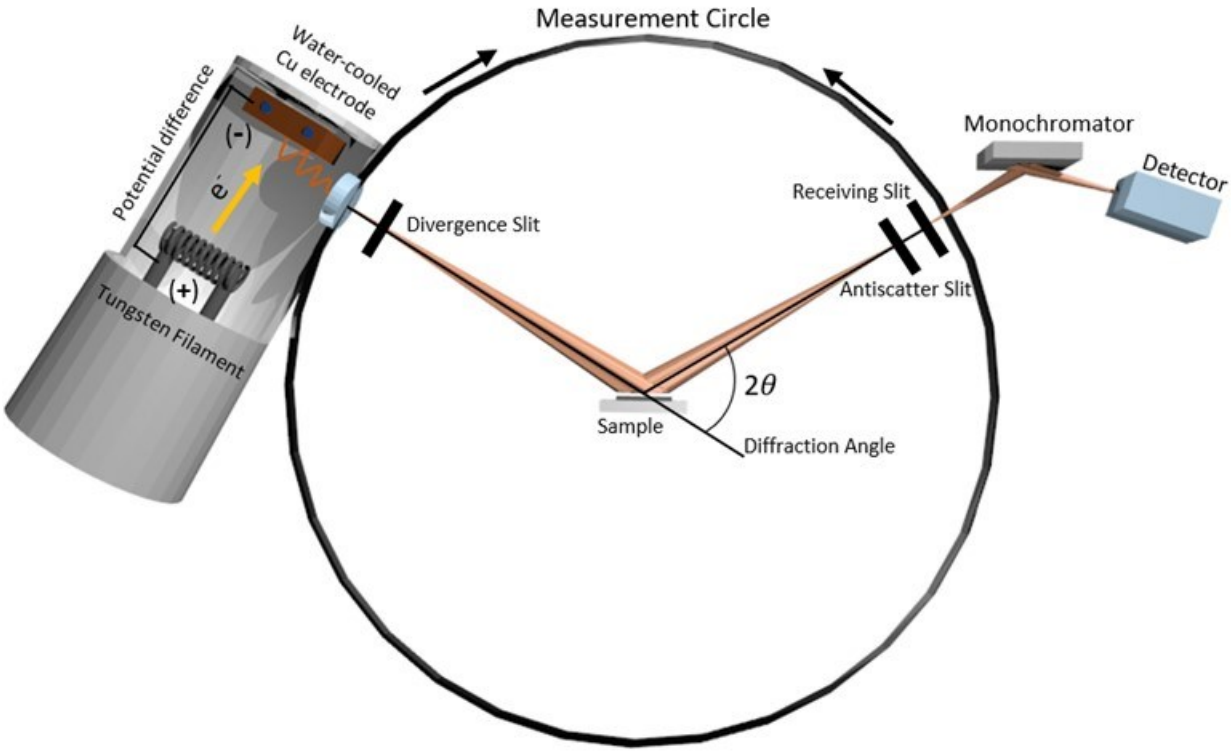

Figure 2.4. Cutaway schematic of a Bragg-Brentano diffractometer.

In this work, XRD patterns were collected using a Rigaku Ultima IV diffractometer with a Cu Kα X-ray source operating at 40 kV and 45 mA. The XRD used a diffracted beam graphite monochromator to filter out Cu-Kβ radiation. Powder samples are placed in a 25 mm × 20 mm × 3 mm stainless-steel sample well and leveled flush with the well height with a glass microscope slide. Measurements were taken from 20° to 60° 2θ with 0.05° step size and a 3 second count time of per step. XRD patterns were plotted as the relative intensity vs. the scattering angle (2θ). At angles of 2θ where the Bragg condition is met, constructive interference occurs, and peaks in the X-ray intensity are observed.

2.6 X-Ray Photoelectron Spectroscopy

X-ray photoelectron spectroscopy (XPS) is a surface sensitive spectroscopic technique that provides a method for probing the chemical composition of the electrode surface. XPS utilizes the photoelectric effect to characterize the elements present on a surface. Generated X-rays are irradiated on a sample to eject photoelectrons from the core level of the atoms by overcoming the binding energy (E_B) of the electron. Electrons from different chemical environments or different elements will have varying E_B, so E_B is the parameter which identifies the electron's source element and atomic energy level.[68] The kinetic energy (E_K) of photoelectrons are measured directing by the spectrometer and with equation 2.2 the E_B is determined to distinguish the source element.

$$E_B = hv - E_k - \Phi_{sp} \qquad 2.2$$

Here, Φ_{sp} is the work function of the spectrometer, which is the energy required for an electron to escape from a solid surface, and hv is the energy of the incident X-ray. A photoelectron from an atom in a higher positive oxidation state will have a higher E_B, because extra coulombic interaction between it and the cation core keeps the electron more tightly bound in its electron-deficient environment.[69] Likewise, the photoelectron from an atom with a lower oxidation state will have a lower binding energy, because of the coulombic repulsion of electron-electron interaction reducing the cations hold on the electron. The capability to distinguish between atoms in different oxidation states and chemical environments makes XPS a powerful technique for determining the composition of surface films.

The typical XPS is equipped with an electron source, such as a tungsten filament, that irradiates a water-cooled aluminum electrode. The electrons that collide with the Al electrode stimulate Al-Kα x-ray generation that is directed towards the sample and is generally first passed through

a monochromator. When the Al-Kα radiation reaches the sample, photoelectrons are emitted and picked up by the lens of the hemispherical sector analyser (HSA). The HSA is essentially a hemispherical capacitor that creates a polarized electric field guiding the incoming electrons towards the inner, positively charged, hemisphere.[68] The HSA separates photoelectrons based on E_K because photoelectrons with less E_K will be moved more by the electric field present in the HSA. This separates the photoelectrons with various E_K values before reaching the multichannel detector. A cutaway image of a typical XPS is shown in Figure 2.5.

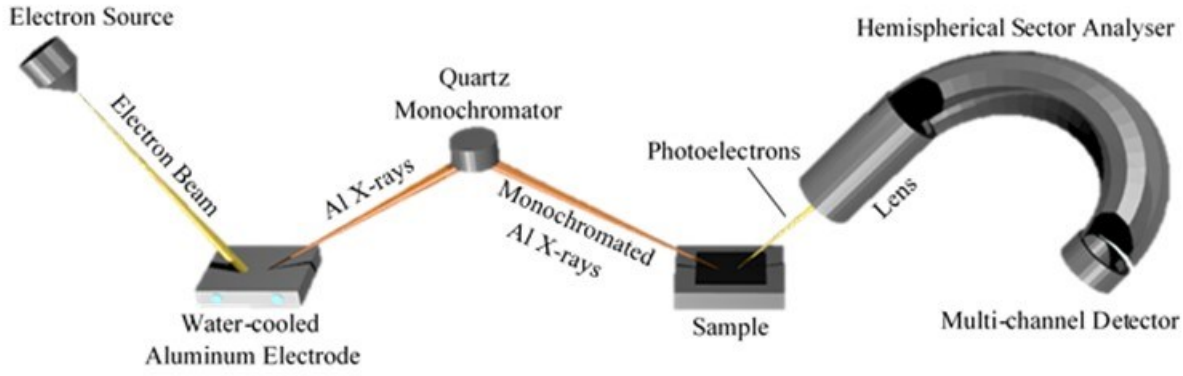

Figure 2.5. Cutaway schematic of a typical XPS.

In this work, samples came from pre- and post-cycled cells. Post-cycled electrodes are air sensitive, so to limit the reactions at the electrode surface the coin cells are disassembled in an Ar-filled glovebox. The coin cells are disassembled to remove the electrodes for sampling and the electrodes are rinsed with DEC to remove impurities from the surface. The rinsed samples are left to dry overnight and then sealed in Ar-filled bags for transfer to the XPS, avoiding as much air exposure as possible. The XPS processing and peak fitting was done by Andrew George from the Department of Physics and Atmospheric Science at Dalhousie University. Dalhousie's XPS does not contain a monochromator, so the generated Al-Kα radiation is unmonochromatized when it reaches the sample. The F1s, C1s, and O1s spectra were focused

on in this work to analyze the species present in the SEI. Additional data processing was needed due to various levels of surface charging in the samples, shifting the peaks. To account for surface charging, the F1s spectra were aligned using the LiF F1s peak, the C1s spectra were aligned using the C-C bond C1s peak, and the O1s spectra were aligned using the Li_2CO_3 O1s peak.

2.7 Electrochemical Impedance Spectroscopy

Electrochemical impedance spectroscopy (EIS) is a powerful, non-invasive technique for determining the internal impedance of an electrochemical cell. A cell's impedance is highly related to its power capability and safety. Measuring impedance can give great insight into the kinetics involved with Li-ion migration. This technique treats the cell as a black box and interprets the kinetic processes by observing the transfer function or the relationship between an input signal and output. The input is usually an alternating current (AC) potential, and the output is a current.[70] In this case the transfer function is the admittance and admittance is the inverse of impedance. The AC potential is usually applied in a frequency range from 10 mHz to 100 KHz to the cell at its open circuit equilibrium potential (OCV). EIS probes the system at equilibrium by applying a slight perturbation and observing how it returns to equilibrium. The amplitude of the applied AC potential is in the mV-range, centered around the cell's OCV, usually between +/- 10 mV. A small amplitude is used to maintain a linear relationship between the current response and applied potential.[70,71]

The current response is reported as a function of the frequency to distinguish various contributions to the current as different frequencies relate to different kinetic mechanisms. For example, mid to high frequency (0.1 Hz to >1000 Hz) responses are generally correlated to

double layer charging, charge transfer resistance, and intercalation processes while low frequency (<0.1 Hz) responses are related to solid-state bulk diffusion phenomena.[12,70]

In impedance spectroscopy, the electrochemical behavior of the cell is represented by an equivalent electrical circuit model. The kinetics involved in Li-ion transport are replicated with a collection of resistors and capacitors which have different responses to the perturbative input potential. For a resistor, impedance is constant with increasing frequency. For a capacitor, the imaginary impedance approaches zero with increasing frequency with no real impedance component. A basic equivalent circuit that accounts for double layer capacitance (C_{DL}), charge transfer resistance (R_{CT}), the electrolyte resistance (R_s), and solid-state diffusion (Z_w) through the electrode is exemplified in Figure 2.6.[72]

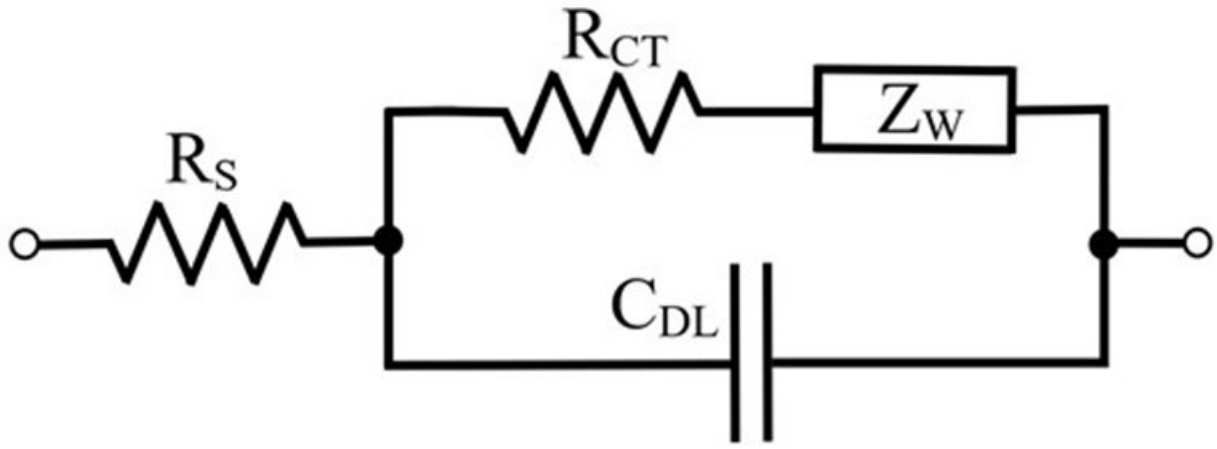

Figure 2.6. Lithium-ion electrode equivalent circuit with resistor in series with a resistor/capacitor parallel group with a Warburg impedance element.

Additional contributions to impedance can also exist, for example from the diffusion of Li^+ in the SEI, particle-particle contact resistance, the imperfect capacitance of the double layer, etc. Here, R_{tot} is used represent the real component of the total impedance experienced by a Li-ion during diffusion from one electrode to another. The simplest way to visualize the R_{tot} is to plot

the negative imaginary impedance vs the real impedance. This is called a Nyquist plot (example in Figure 2.7). For a resistor/capacitor parallel group, the Nyquist plot shows a well-defined semi-circle where the diameter is equal to R_{tot}.[12,70]

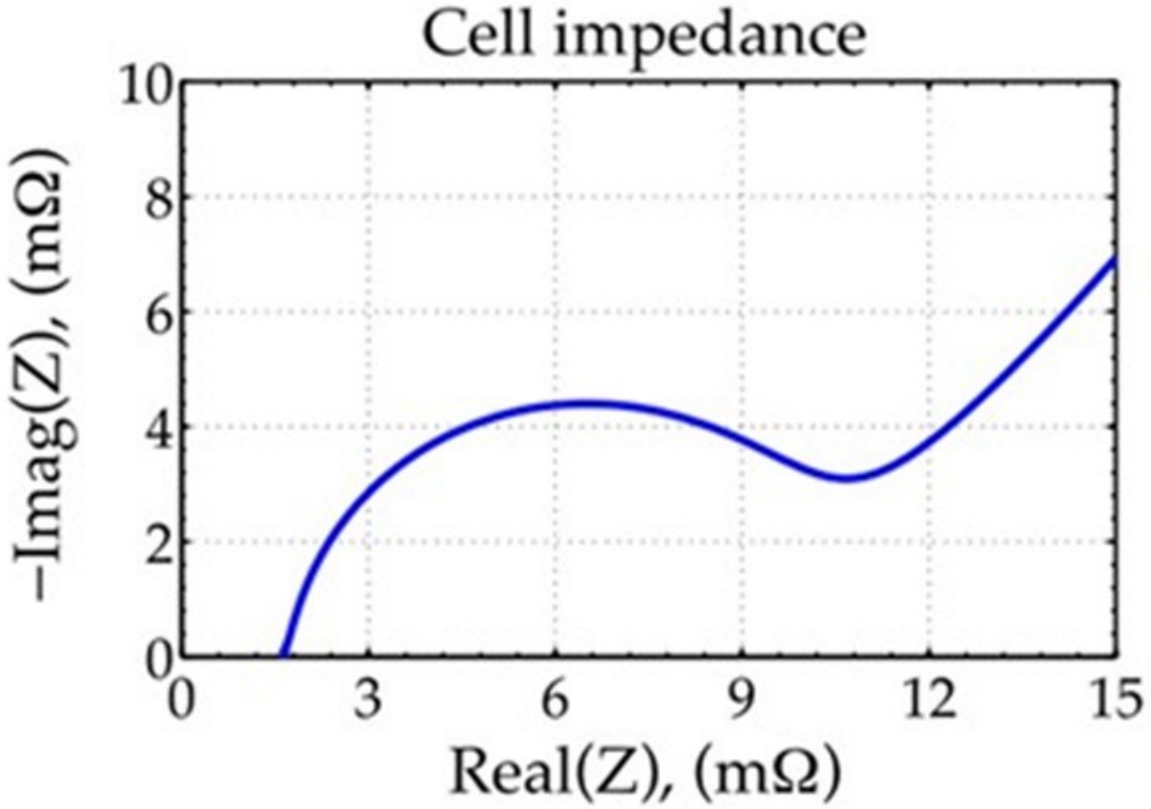

Figure 2.7. Nyquist plot of an equivalent circuit model similar to the model in Figure 2.6.[11] Reproduced with permission from Reference 11.

EIS was performed in this work using a Biologic VMP-3 potentiostat where alternating current (AC) impedance spectra were collected with 10 points per decade from 100 kHz to 10 mHz with a 10 mV amplitude signal. The total impedance values, (R_{tot}), is represented by the diameter of the semicircle in the Nyquist plot, which corresponds to the sum of the R_{CT} and the resistance of lithium ions transporting through the SEI layer.

CHAPTER 3. ACTIVE MATERIAL ADDITIVES[1]

3.1 Introduction

Electrolyte solvent additives are commonly used to improve electrochemical performance in Li-ion cells by modifying SEI formation. The use of solids as additives to modify SEI formation is far less common. Here, $Si_{40'}(FeSi_2)_{(60-x)'}(LiF)_{(x)'}$ and $Si_{40'}(FeSi_2)_{(60-x)'}(Li_2CO_3)_{(x)'}$ (' = volume percent) alloys with LiF or Li_2CO_3 incorporated in the alloy as a solid active material additive are studied. The use of solid additives may be a valuable method for improving electrochemical performance of Si-alloy negative electrodes. Silicon-based negative electrode materials have been heavily researched as a means of increasing energy density in next-generation LIBs. By using Si based negative electrode materials, it is estimated that full cell energy density can be increased by as much as 34%.[12] Si is able to store 22.5 times more lithium per host atom than

---

[1] A majority of Chapter 3 has been previously published as R. S. Young, B. Scott, Congxiao Wei, and M. N. Obrovac. *J. Electrochem. Soc*, **167**, 160524. (2020). All cycling, EIS, XRD, and SEM images of $Si_{40'}(FeSi_2)_{(60-x)'}(LiF)_{(x)'}$ alloys was content from this article. R.S. Young prepared all samples, measured all XRD patterns, built all coin cells, performed all EIS, analyzed all samples with SEM, and prepared all XPS samples. B. Scott monitored the slurry additive cell cycling while the primary author was away and Congxiao Wei was responsible for preparing the electrode cross-sections for SEM. The XPS data of Figure 3.9 and 3.10, along with the Li_2CO_3 additive results, represents work exclusively done by the author that has not previously been published.

graphite which is conventionally used as a negative electrode material in LIBs, and, as a result Si, has a theoretical volumetric capacity of 2194 Ah/L, 3 times larger than that of graphite (719 Ah/L).[12] However, the electrochemical lithiation of Si causes a volume expansion as large as 280%, resulting in poor charge/discharge cycling characteristics.[12,21]

In order to decrease volume expansion and improve cycling performance, Si can be alloyed with an electrochemically inactive component such as iron.[12,21,73] It has additionally been shown that the addition of an inactive phase can decrease the potential at which $Li_{15}Si_4$ forms. $Li_{15}Si_4$ contributes directly to poor cycling performance as a result of the high stress generated at the two-phase reaction front during delithiation, causing particles to fracture and become mechanically disconnected.[19,74] In pure Si, $Li_{15}Si_4$ crystallizes at 50 mV.[19,74] By incorporating an inactive phase, $Li_{15}Si_4$ formation can be suppressed completely.[19,73]

Here, the addition of inactive phases that have an additional function of helping form a more stable SEI are considered. LiF and Li_2CO_3 were selected for this purpose, since they have been found to be components of stable SEIs. It was thought that when these solid additives are incorporated directly in Si-alloys as an inactive phase, they might have the following beneficial properties:

- act as a typical inactive phase by reducing volume expansion and suppressing $Li_{15}Si_4$ formation
- any additive phase on the surface might be incorporated directly in the SEI, resulting in enhanced SEI stability
- any additive phase within the particles could enhance SEI formation on any alloy surfaces exposed during cycling due to particle fracture

- in the case of LiF (which has sparing solubility in the electrolyte), enhance stable SEI formation via modification of the electrolyte composition

3.2 LiF

LiF has been previously studied as a surface modifier to improve cycling performance of negative electrode materials. Wu et al. used LiF as a surface modifier for graphene, resulting in increased cycle life, and rate capability.[9] It was found that the LiF provided an extra Li source, lowering the initial irreversible capacity, while reducing SEI thickness, suppressing electrolyte side reactions, and enabling faster Li-ion transport.[6] Using DFT, Y. X. Lin et al. were able to show that a layer of LiF as thin as 2 nm can prevent electron tunneling from a lithium electrode, whereas Li_2CO_3, another well-known SEI component, requires 3 nm.[52] As a consequence, an effective SEI comprising LiF is formed thinner, resulting in the observed faster Li-transport. Fluorinated electrolyte additives are commonly used to form a thinner more stable SEI layer comprising LiF.[15,35,53] However, the use of fluorinated electrolyte additives can increase electrolyte cost and introduce irreversible capacity losses.

In this study, LiF is evaluated as a component in Si-Fe alloys. Being an inactive component, it is expected to improve cycling performance by reducing overall alloy volume expansion. LiF is slightly soluble in carbonate electrolytes (LiF solubility in dimethyl carbonate (DMC) is 1.07×10^{-5} mole fraction at 25 °C and 101.1 kPa).[12] Therefore, the presence of LiF in the alloy is additionally expected to act as an electrolyte additive, by keeping the electrolyte constantly saturated with LiF, so that it is continuously incorporated into the SEI.

3.2.1 Experimental

Si-$FeSi_2$-X (X = LiF) alloys were prepared from Si (99%, -325 mesh, Sigma-Aldrich), Fe (99.9%, -325 mesh, Sigma-Aldrich) and LiF (98.5%, -325 mesh, Alfa-Aesar). A total of 0.5 mL of precursor powder was loaded into a 65 mL hardened steel milling vial (SPEX, model 8000-D, Spex CertiPrep, Metuchen, NJ) with 180g of 1.6 mm stainless steel balls. Loaded vials were sealed under an argon atmosphere.[61] Initially alloys were prepared by loading all three components and ball milling simultaneously; however, it was found that the presence of LiF inhibited the mechanochemical reaction of Si and Fe. Instead, a two-step ball milling procedure was used where Si and Fe were first milled for 8 hours, followed by the addition of LiF and an additional 8 hours of milling.

SEM images were obtained with a TESCAN MIRA 3 field-emission SEM using a 5.0 kV accelerating potential. Both secondary electron (SE) and back-scattered electron (BSE) images were collected pre- and post-cycling. XRD patterns were collected using a Rigaku Ultima IV diffractometer with a Cu Kα x-ray source operating at 40 kV and 45 mA and a diffracted beam graphite monochromator.

Electrode slurries were prepared by mixing a 70:5:25 weight ratio of alloy:carbon black (Imerys Graphite and Carbon, Super C65):binder in an appropriate slurry solvent. For some electrodes the binder/slurry solvent was an aromatic polyimide (PI)/n-methyl-2-pyrrolidinone (NMP, 99.5%, Sigma-Aldrich) where the polyimide was added in the form of a 20% (w:w) solution of poly(amic acids) in NMP (Hitachi DuPont MicroSystems, LLC). Slurries were mixed using a high-shear mixer equipped with a Cowles blade for 10 minutes at a rotational frequency of 5000 rpm. Electrode slurries were coated onto electrolytic copper foil (Furukawa Electric,

Japan) to a slurry thickness of 0.102 mm using a stainless-steel coating bar and dried at 120 °C for 1 hour. 1.3 cm^2 electrode disks were cut from the coatings. Electrodes with PI binder were subsequently cured by heating at 300 °C for 4 hours under flowing argon, as described in Reference 62.[62]

Electrodes were assembled into 2325-type coin cells with a lithium foil counter/reference electrode separated by one layer each of Celgard 2300 and blown polypropylene microfiber (BMF) separator (3M Co.). The cells were assembled in an Ar-filled glove box using 100 µL of electrolyte. Electrolyte consisted of either 1 M $LiPF_6$ (BASF, 99.94%, water content 14 ppm) in (v:v) (3:6:1) ethylene carbonate (EC):diethyl carbonate (DEC) (BASF, 98%, water content < 50 ppm):fluoroethylene carbonate (FEC) (BASF, > 99.94%) or 1 M $LiPF_6$ in (v:v) EC:DEC (1:2).

Cells were cycled at 30.0 ± 0.1°C between 0.005 V and 0.9 V with a Maccor Series 4000 Automated Test System at a rate of C/10 for the first cycle and C/5 for subsequent cycles. To simulate CCCV full cell charging, cells were held at 5 mV at the end of each cycle until a C/20 current limit was reached. C-rates were determined based on a theoretical 3578 mAh/g active Si capacity. The fade rate was defined as the average percent capacity fade per cycle encountered between cycles 10 and 80.

Symmetric cells were assembled in 2325-type coin cells with two identical electrodes separated by two layers of Celgard 2300 and one layer of blown polypropylene microfiber (BMF). One of the electrodes is prepared in a lithiated state, while the other is in a delithiated state, as follows. The delithiated electrode was lithiated to a potential of 0.005 V and then delithiated to

0.9 V at a rate of C/20. The lithiated electrode was lithiated to a potential of 0.005 V, delithiated to 0.9 V at a rate of C/20 and then lithiated to 0.005 V at a C/5 rate and held at this potential until the current dropped below C/20.

Electrochemical impedance spectroscopy (EIS) was performed with a Biologic VMP-3 potentiostat where alternating current (AC) impedance spectra were collected with 10 points per decade from 100 kHz to 10 mHz with a 10 mV amplitude signal. In this work total impedance values, (R_{tot}), represent the diameter of the semi-circle in the Nyquist plot, which corresponds to the sum of the charge transfer resistance and the resistance of lithium ions transporting through the SEI layer.[75]

X-ray photoelectron spectroscopy (XPS) measurements of the $Si_{40'}(FeSi_2)_{(60-x)'}(LiF)_{(x)'}$ electrodes were performed on both pristine and post-formation (after 3 cycles) cells. The samples were prepped in an argon-filled glove box, where coin cells were disassembled, the electrodes were rinsed with DEC to remove impurities, and the electrodes were left to dry in the glove box overnight. After drying, the samples were taken to the spectrometer in airtight argon-filled bags to limit exposure to the atmosphere. The XPS samples in this work were processed by Andrew George from the Department of Physics and Atmospheric Science at Dalhousie University. The F1s, C1s, and O1s spectra were focused on to analyze the species present in the SEI. After retrieving the data from Andrew, various levels of surface charging were observed in the samples. Surface charging on the samples caused peaks to be shifting to higher binding energies. To account for surface charging, the F1s spectra were aligned to the LiF F1s peak, the C1s spectra were aligned to the C-C bond C1s peak, and the O1s spectra were aligned to the Li_2CO_3 O1s peak.

3.2.2 Results and Discussion

A series of ball milled Si-Fe-LiF alloys were prepared such that the volume expansion experienced upon lithiation was always 112%. This corresponds to an active Si volume fraction of 40%.[2]

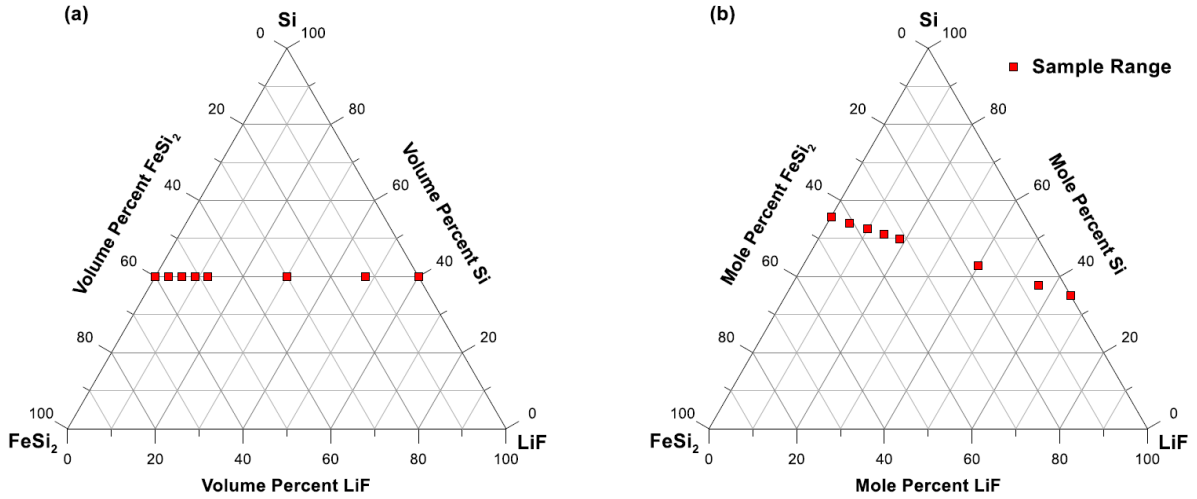

Figure 3.1. Ternary Si-$FeSi_2$-LiF composition diagrams in terms of (a) volume percent and (b) mole percent. The red squares indicate the compositions explored in this work.

This composition range is shown in Figure 3.1(a) and (b) in terms of volume percent and mole percent of each component, respectively. This series can be represented in terms of volume percent as $Si_{40'}(FeSi_2)_{(60-x)'}(LiF)_{(x)'}$ where the primed quantities are used to indicate volume percentage, in order to differentiate them from conventional chemical formula units.

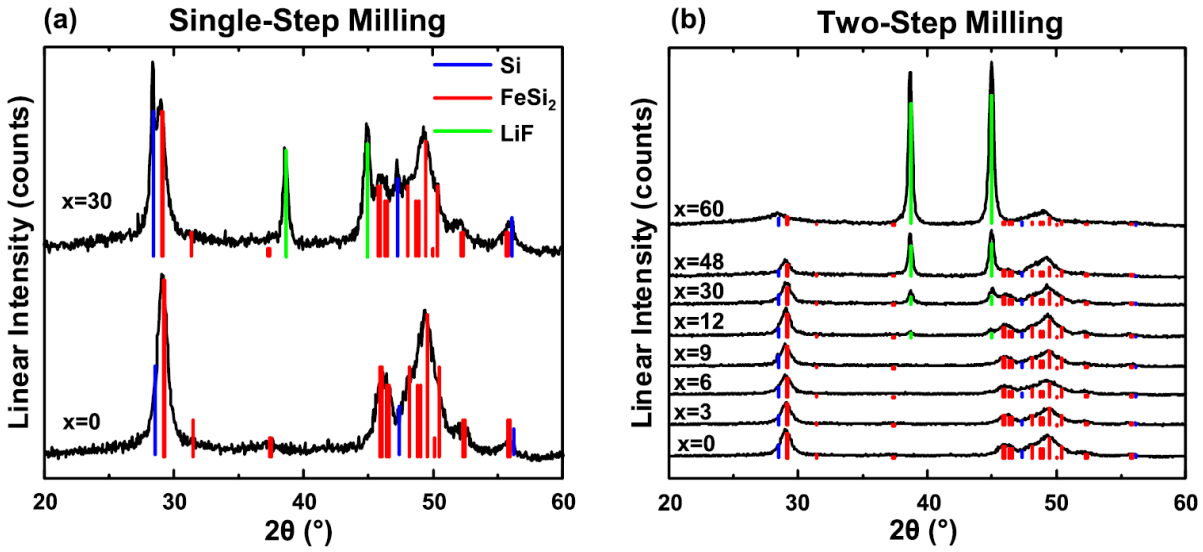

Figure 3.2. XRD patterns of $Si_{40'}(FeSi_2)_{(60-x)'}(LiF)_{(x)'}$ prepared by (a) milling in a single step, and (b) milling in two-steps.

XRD patterns of ball milled $Si_{40'}(FeSi_2)_{(60-x)'}(LiF)_{(x)'}$ (x = 0 and x = 30) alloys are shown in Figure 3.2(a). When there is no LiF present, crystalline Si (cr-Si) and Fe react, forming $FeSi_2$ and amorphous Si (a-Si). However, when LiF is present, a peak corresponding to unmilled cr-Si is present in the XRD pattern. Apparently, the presence of LiF impedes the amorphization of Si during ball milling. In order to obtain an amorphous active Si phase for each sample, milling was conducted in two steps. In the first step only Si and Fe were milled, to form a Si-Fe alloy with a completely amorphous active Si phase. This was followed by a second milling step to incorporate LiF. XRD patterns of alloys synthesized using this two-step method are shown in Figure 3.2(b). These alloys consist of a-Si, LiF and $FeSi_2$. As the LiF content is increased there is a proportional increase in the intensity of the LiF peaks in the XRD patterns and a simultaneous decrease in the $FeSi_2$ peak intensity, as expected.

Symmetric cells were constructed in order to determine the effect of LiF additions in $Si_{40'}(FeSi_2)_{(60-x)'}(LiF)_{(x)'}$ on impedance.

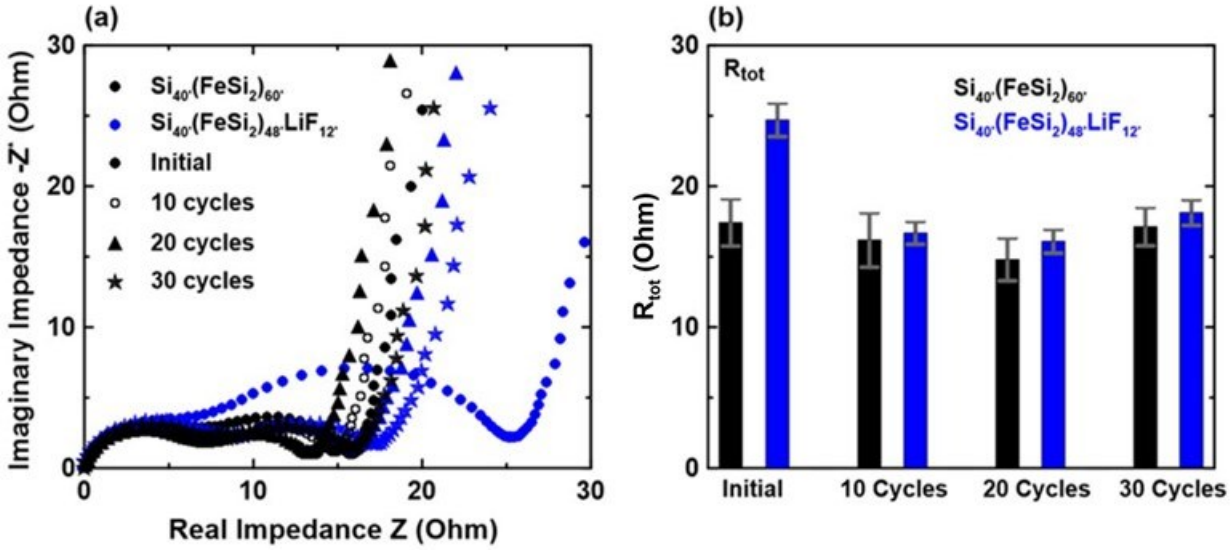

Figure 3.3. (a) Nyquist plots of $Si_{40'}(FeSi_2)_{(60-x)'}(LiF)_{(x)'}$ electrodes where x = 0 and 12, and (b) corresponding R_{tot} values. Error bars were calculated based on three duplicate cells for each experiment.

Electrochemical impedance spectra of $Si_{40}(FeSi_2)_{(60-x)}(LiF)_{(x)}$ (x = 0 and 12) electrodes measured prior to cycling and after 10, 20, and 30 cycles are shown in Figure 3.3(a) and the corresponding R_{tot} values are shown in Figure 3.3(b). R_{tot} was measured as the distance from the origin to the minimum point at the end of the capacitance spike. In this data, the appearance of two semicircles indicates the presence of two distinct interfaces, likely the electrolyte/SEI interface and the SEI/electrode interface. Electrodes containing LiF had higher impedance initially. During initial cycling, the impedance of both electrodes decreased. This has been observed previously by Yan et al. and may be due to a decrease in electronic resistance as the electrode expands and the resulting compressive stresses improve the electrical connection between alloy particles.[18] However, R_{tot} decreases more rapidly during initial cycles, to nearly match that of the pure Si-Fe alloy after 10 cycles, possibly because of more efficient SEI formation.

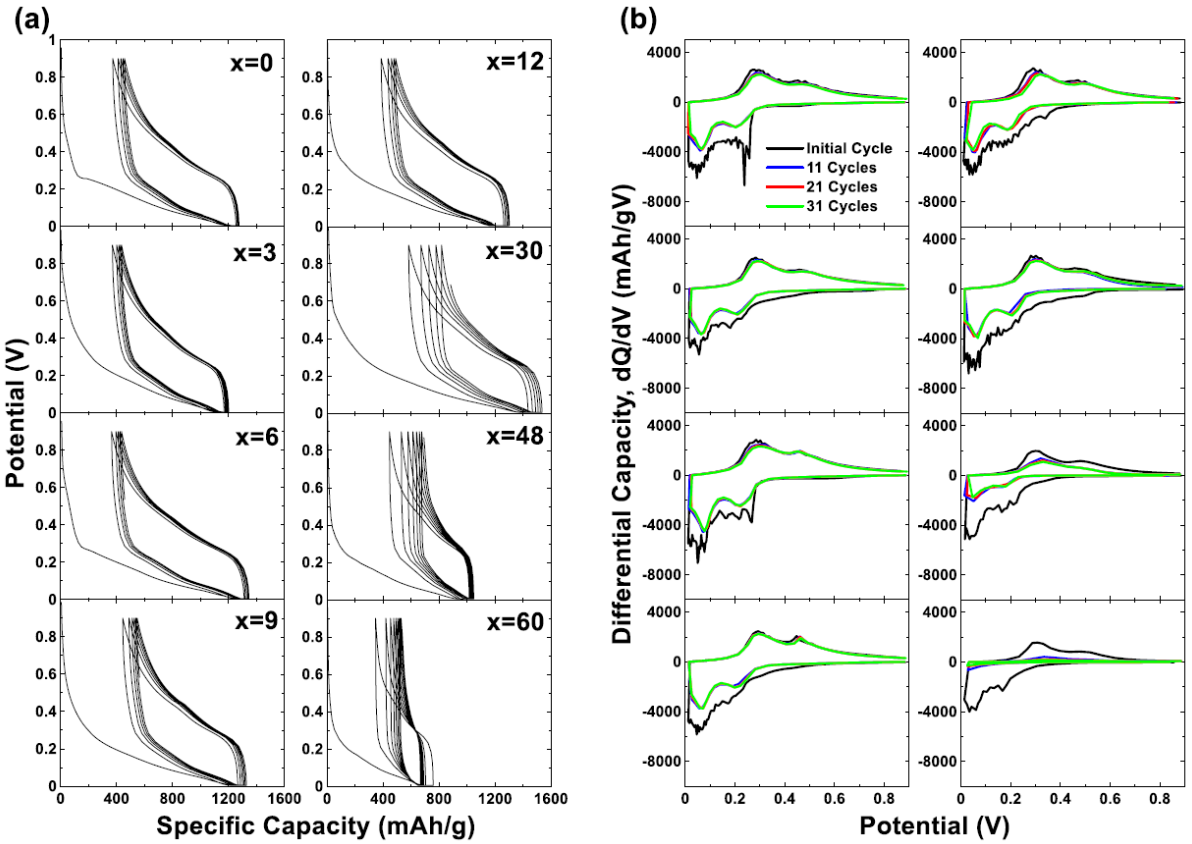

Figure 3.4. (a) Potential profiles and (b) differential capacity curves of $Si_{40'}(FeSi_2)_{(60-x)'}(LiF)_{(x)'}$ electrodes.

Potential profiles and differential capacity plots of $Si_{40'}(FeSi_2)_{(60-x)'}(LiF)_{(x)'}$ electrodes cycled in half-cells are shown in Figure 3.4(a) and (b). The potential profiles and differential capacity curves are characteristic of a-Si with two sloping plateaus and no evidence of $Li_{15}Si_4$ formation. All of the potential profiles are similar for $x \leq 12$. Larger LiF content results in decreased initial coulombic efficiency (ICE), lower reversible capacity, and fade. It is speculated that this may be due to the partial solubility of LiF in the electrolyte, which may lead to alloy degradation for high LiF contents.

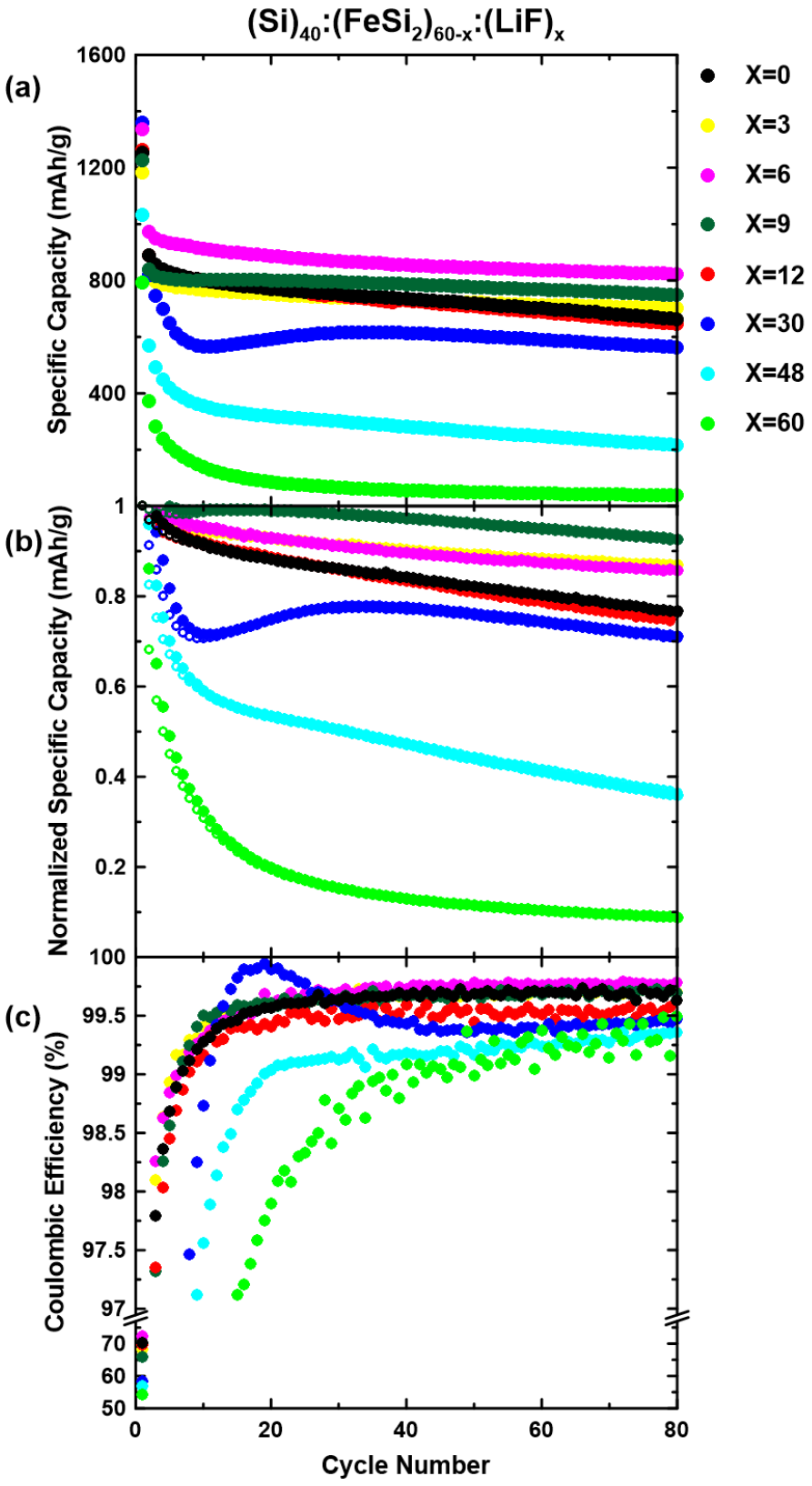

Figure 3.5. (a) Specific capacity vs cycle number, (b) normalized capacity vs cycle number, and c) columbic efficiency vs cycle number of $Si_{40'}(FeSi_2)_{(60-x)'}(LiF)_{(x)'}$ electrodes.

Figure 3.5(a) shows the cycling performance of the $Si_{40'}(FeSi_2)_{(60-x)'}(LiF)_{(x)'}$ electrodes. For small values of x, as the LiF content increases, the specific capacity also increases. This is expected since the molar mass of the electrode decreases as $FeSi_2$ (4.95 g/mL) is replaced by an equal volume of LiF (2.64 g/mL). To account for this change in molar mass, capacities were normalized according to their first delithiation capacity, as shown in Figure 3.5(b). The pure Si-Fe alloy (x = 0) has a capacity retention of nearly 80% after 80 cycles. The capacity retention increases significantly, to over 95%, as the LiF content is increased to x = 9. As LiF content is further increased there is a continual decrease in capacity. This is likely caused by the degradation of the $Si_{40'}(FeSi_2)_{(60-x)'}(LiF)_{(x)'}$ alloys with high LiF contents, due to LiF solubility, as mentioned above. Figure 3.5(c) shows the coulombic efficiency (CE) of the $Si_{40'}(FeSi_2)_{(60-x)'}(LiF)_{(x)'}$ electrodes. The pure Si-Fe alloy has a steady-state CE of about 99.6%. A slightly improved CE of 99.8% is observed when x = 6. Poor CE is observed for higher values of x, as expected. In half-cell testing, capacity retention is thought to be related to electrode mechanical integrity, while CE is related to the extent of electrolyte reactions at the electrode surface. The above results imply that small additions of LiF to alloys aid in maintaining alloy mechanical integrity and in reducing electrolyte reactivity. Indeed, this can be seen in Figure 3.6, which shows cross-sectional BSE-SEM images of $Si_{40'}(FeSi_2)_{(60)'}$ and $Si_{40'}(FeSi_2)_{(54)'}(LiF)_{(6)'}$ electrodes before and after cycling.

In Figure 3.6(a), both $Si_{40'}(FeSi_2)_{(60)'}$ and $Si_{40'}(FeSi_2)_{(54)'}(LiF)_{(6)'}$ alloy particles prior to cycling appear bright in the images, due to the high contrast between the iron containing alloy and the polymer binder and carbon black between the alloy particles. In addition, the pristine alloy particles have sharp definite edges. After cycling, both electrodes show signs of fracture surface erosion, as has been observed previously for alloy particles,[76] however the extent of the

degradation is much less in the $Si_{40'}(FeSi_2)_{(54)'}(LiF)_{(6)'}$ alloy. This can be seen more clearly in the lower magnification images shown in Figure 3.6(b). The difference is striking. Almost all of the $Si_{40'}(FeSi_2)_{(60)'}$ alloy has been eroded after 100 cycles, whereas most of the $Si_{40'}(FeSi_2)_{(54)'}(LiF)_{(6)'}$ alloy still intact. The above results imply that small additions of LiF to alloys aid in maintaining alloy mechanical integrity and in reducing electrolyte reactivity. This may be accomplished via a thinner, more stable SEI formation with small additions of LiF.

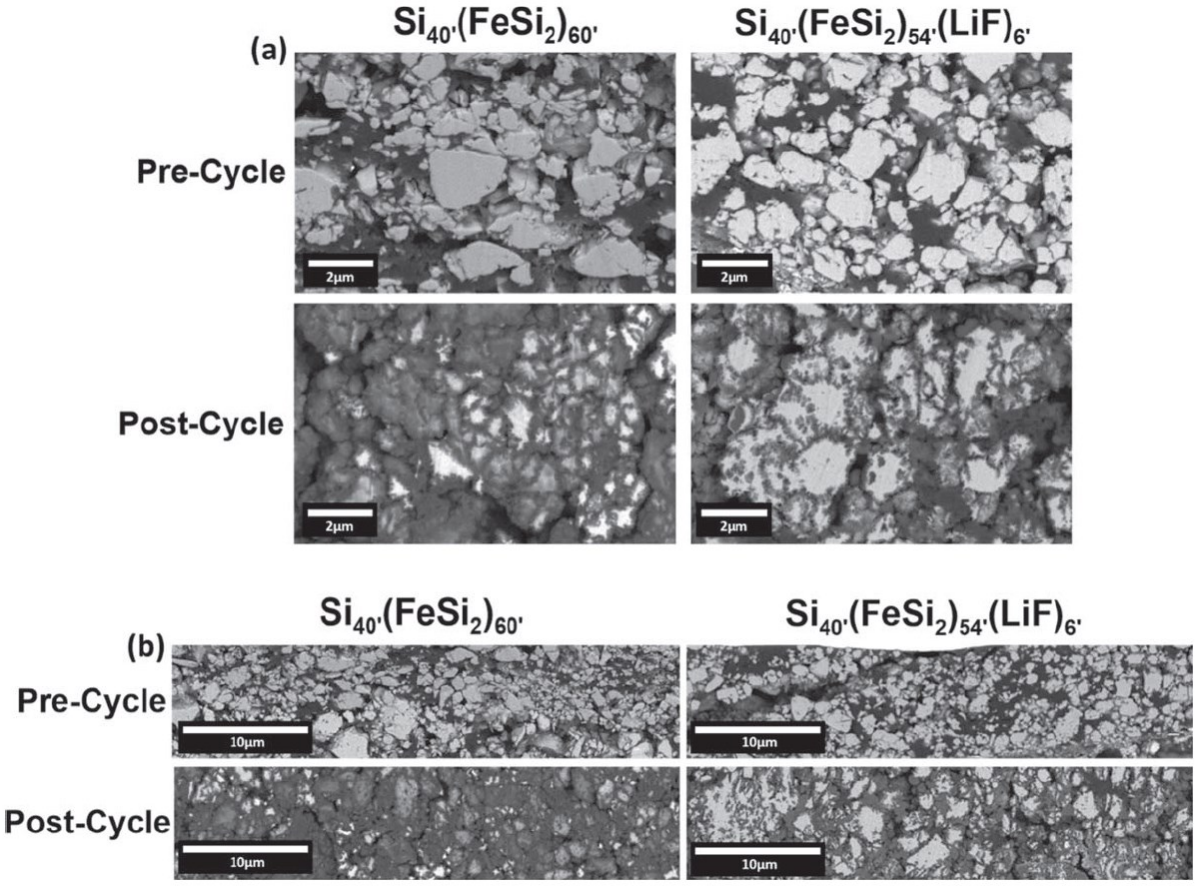

Figure 3.6. Cross-sectional BSE-SEM images of $Si_{40'}(FeSi_2)_{(60-x)'}(LiF)_{(x)'}$ for x=0 and 6, pre and post cycling. (a) high magnification, (b) lower magnification.

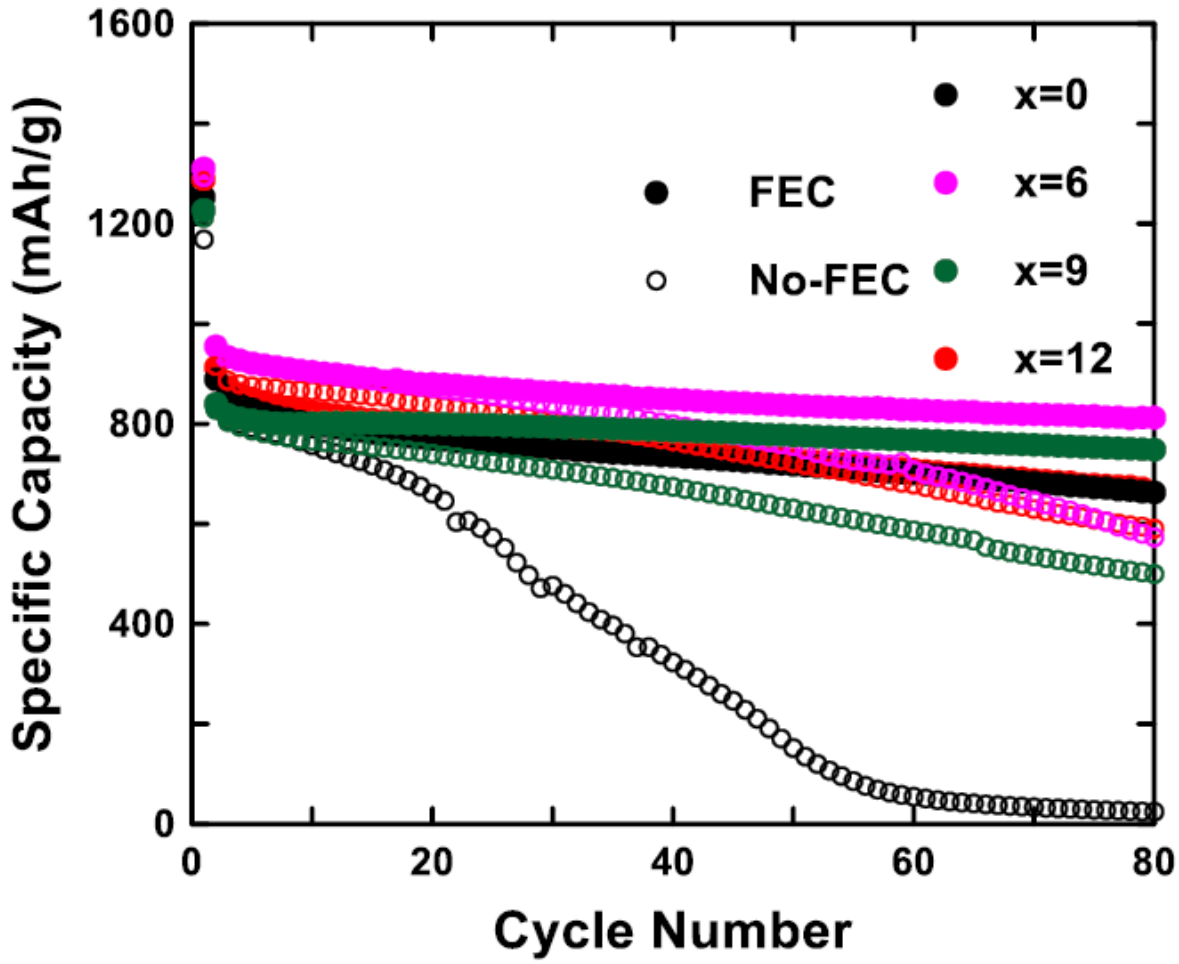

Figure 3.7. Cycling performance of $Si_{40'}(FeSi_2)_{(60-x)'}(LiF)_{(x)'}$ electrodes in FEC containing and FEC-free electrolyte.

Figure 3.7 displays the results of cycling the $Si_{40'}(FeSi_2)_{(60-x)'}(LiF)_{(x)'}$ alloys in electrolyte with and without FEC additive. $Si_{40'}(FeSi_2)_{(60)'}$ alloy shows rapid capacity fade (~0% capacity retention / 60cycles) when no FEC is present. Additions of LiF result in significant cycling improvement, with $Si_{40'}(FeSi_2)_{(54)'}(LiF)_{(6)'}$ having 60% capacity retention after 80 cycles. When FEC is added, the fade rate of the $Si_{40'}(FeSi_2)_{(60)'}$ alloy is superior (75% capacity retention / 80 cycles) to what was achieved by adding LiF alone. However, the best capacity retention is obtained when both FEC and LiF are utilized (85 % capacity retention / 80 cycles). Therefore, LiF and FEC seem to be additive in their ability to improve capacity retention.

LiF was then used as a slurry additive to determine whether the addition of LiF to the alloy by ball milling was necessary. $Si_{40'}(FeSi_2)_{(60-x)'}$ alloys were prepared where x = 0, 6, and 9; and LiF component was incorporated as an additive in the electrode slurry, so that the final electrode composition was identical to the $Si_{40'}(FeSi_2)_{(60-x)'}(LiF)_{(x)'}$ series alloys. Electrochemical performance was evaluated in FEC-containing and FEC-free electrolyte, shown in Figure 3.8.

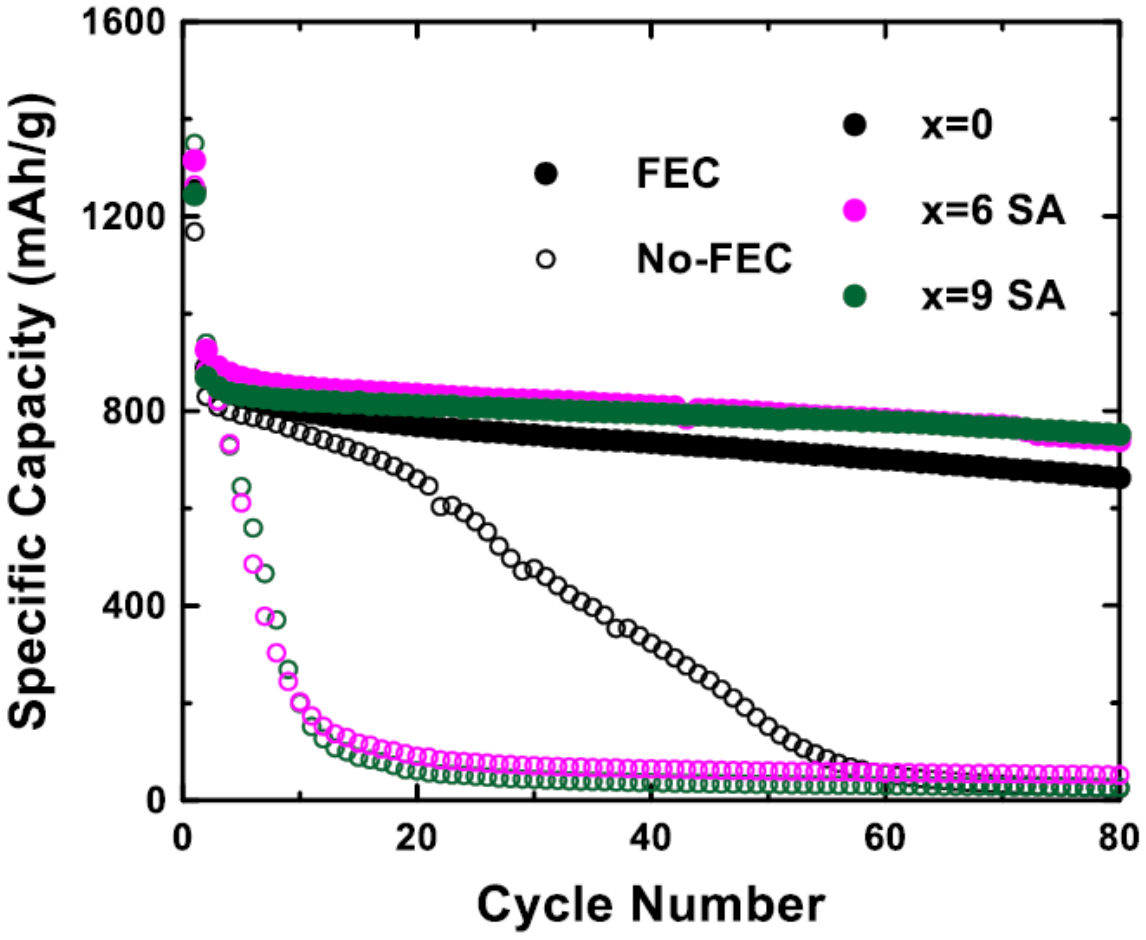

Figure 3.8. Cycling performance $Si_{40'}(FeSi_2)_{(60-x)'}$ where $(LiF)_{(x)'}$ was incorporated as a slurry additive (SA) using FEC containing and FEC-free electrolyte.

When electrolyte contained FEC, improved capacity retention was observed for x = 6 and 9, compared to x = 0. The improvement for x = 9 was identical to when the LiF was incorporated directly in the alloy. However, for x = 6, the best performing formulation (13.00 % fade rate) did not have the degree of improvement as when the LiF was incorporated directly in the alloy

(9.78 % fade rate). Therefore, the addition of LiF to electrode slurries can be a facile method for improving electrochemical performance of Si-alloy negative electrodes. However, in this instance incorporating LiF directly in the alloy is superior. When the electrolyte did not contain FEC, LiF additions to the slurry caused rapid capacity fade. This behavior is typical of rapid mechanical failure of the electrode. It is difficult to understand why this is not a failure mode when FEC is present. It is suspected that when FEC is present, FEC decomposition products already saturate the electrolyte with LiF, limiting the dissolution of the LiF that is incorporated in the electrode, thereby reducing the electrode mechanical failure.

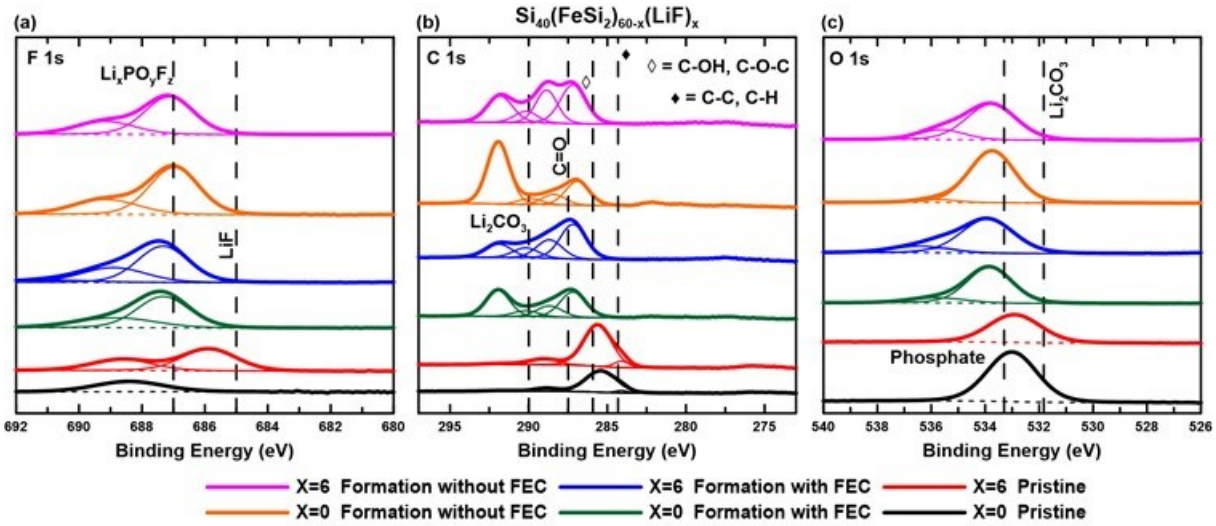

Figure 3.9. Post formation XPS F 1s, C1s, and O1s spectra for $Si_{40'}(FeSi_2)_{(60-x)'}(LiF)_{(x)'}$ alloy electrodes from half-cells with 1 M $LiPF_6$ in EC:DEC (1:2 v/v) electrolyte with 10 vol% FEC (blue (x = 6) and green (x = 0)) and no additives (pink (x = 6) and orange (x = 0)). Pristine electrode samples are also given in red (x = 6) and black (x = 0). No charge corrections.

Figure 3.9 shows XPS spectra of pristine and post-cycled (cycled 3) $Si_{40'}(FeSi_2)_{(60-x)'}(LiF)_{(x)'}$ electrodes with x =0 and x = 6. The cycled electrodes were cycled vs Li metal in electrolytes consisting of 1 M $LiPF_6$ in EC:DEC (1:2 v/v) with and without 10 vol% FEC. In Figure 3.9(a), there is an unexpected peak found in the F1s spectra around 688.5 eV. The pristine x = 0 sample does not contain any fluorinated substances, so the peak at 688.5 eV should not be there. The same peak is seen in the pristine x = 6 sample as well. After repeated scanning of the sample it

was determined that this peak was not a product of error and given the position it is thought that this may be a Fe 2p peak.[77] In Figure 3.9, it was observed that the samples had various levels of surface charging. If the sample is insulating, photoemission can cause electrostatic charging to occur which results in the peak positions being shifted to a higher binding energy.[68] To account for surface charging, the F1s spectra in Figure 3.9(a) were aligned to the LiF F1s peak, the C1s spectra in Figure 3.9(b) were aligned to the C-C bond C1s peak, and the O1s spectra in Figure 3.9(c) were aligned to the Li_2CO_3 O1s peak. This resulted in the XPS spectra of Figure 3.10 shown below.

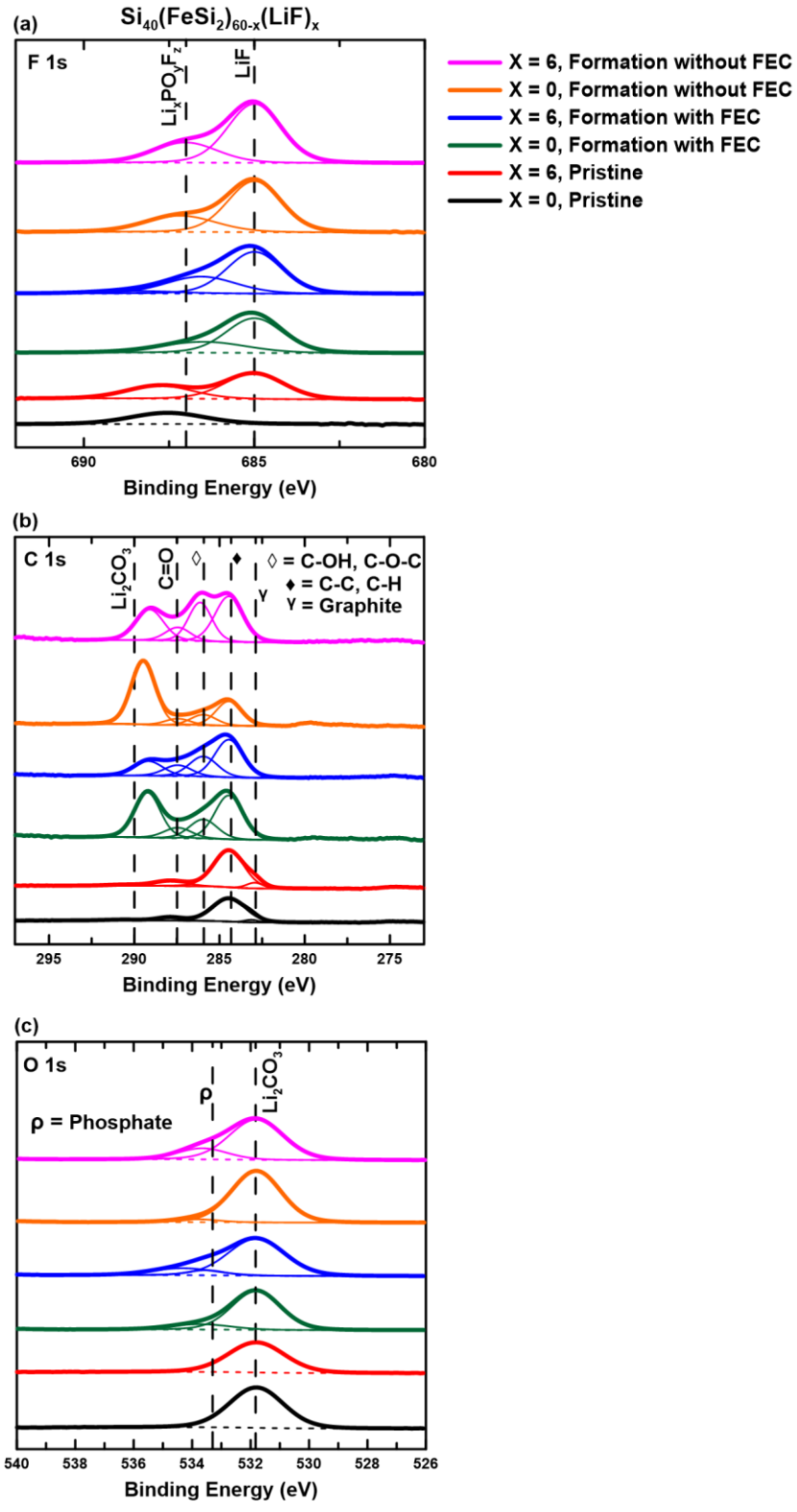

Figure 3.10. XPS F 1s, C1s, and O1s spectra corrected for charging effects for $Si_{40'}(FeSi_2)_{(60-x)'}(LiF)_{(x)'}$ alloy electrodes from half-cells with 1 M $LiPF_6$ in EC:DEC (1:2 v/v) electrolyte with 10 vol% FEC (blue (x = 6) and green (x = 0)) and no additives (pink (x = 6) and orange (x = 0)). Pristine electrode samples are also given in red (x = 6) and black (x = 0).

Figure 3.10(a) clearly shows the presence of LiF on the surface of all electrodes post-cycling. Sources of LiF for $Si_{40'}(FeSi_2)_{(60-x)'}(LiF)_{(x)'}$ x = 0 electrodes include FEC and $LiPF_6$. $Li_xPO_yF_z$ was assigned to a lower binding energy peak and is a well-known SEI component in carbonate electrolytes containing $LiPF_6$ salts.[35] No significant differences could be identified amongst the post-cycled electrodes, however the analysis was hindered because of the presence of the Fe 2p peak.

Figure 3.10(b) shows the C1s spectra of the pre and post-cycled electrodes. Peaks in these spectra were identified as being from the carbon in Li_2CO_3 along with C-C, C-H, C-O-C, and C-OH bonding. There is a C-C peak around 284.5 eV, a large C-H peak around 285 eV, a C-O peak around 286-287 eV, and a small C=O peaks around 288-289 eV.[78] All post-formation electrodes also formed Li_2CO_3, identified by a peak around 290 eV.

Figure 3.10(c) shows the O1s spectra of the pre and post-cycled electrodes. The O1s spectra also confirmed the presence of Li_2CO_3 with a peak around 531.8 eV and shows the presence of phosphate in some post-cycled cells with a peak around 533-533.5 eV, consistent with the $Li_xPO_yF_z$ identified in the F 1s spectra. An interesting trend observed in the O1s spectra is the relative amounts of phosphate in the x = 0 and x = 6 electrodes. The relative phosphate present is quantified by the phosphate to Li_2CO_3 peak ratio, which are listed in Table 3.1. Error from the peak fitting was determined by measuring the variation in the peak ratios that caused a ± 1 change in the goodness of fit. It was observed that cells containing LiF have a higher phosphate to Li_2CO_3 peak ratio then the electrodes without. Furthermore, cells in FEC containing electrolytes also have higher phosphate to Li_2CO_3 peak ratios. This shows that electrodes cycled in FEC containing electrolyte form more phosphate compounds and electrodes with LiF form even higher amounts. Since the signal is consistent with $Li_xPO_yF_z$, this could further explain

why cells with increased phosphate to Li_2CO_3 peak ratio have increased capacity retention. Previous work found that the presence of $Li_xPO_yF_z$ in the negative electrode SEI increases the discharge capacity of Li-ion cells.[79,80]

Table 3.1. Phosphate to Li_2CO_3 peak ratios from the O1s spectra of $Si_{40'}(FeSi_2)_{(60-x)'}(LiF)_{(x)'}$ electrodes for x = 0 and 6.

$Si_{40'}(FeSi_2)_{(60-x)'}(LiF)_{(x)'}$	FEC containing electrolyte (Phosphate)/(Li_2CO_3) ratio	FEC-free electrolyte (Phosphate)/(Li_2CO_3) ratio
x = 0	0.17 ± 0.01	0.05 ± 0.01
x = 6	0.35 ± 0.02	0.25 ± 0.01

The C1s spectra of the pre and post cycled alloys are shown in Figure 3.10(b). It was observed that higher relative amounts of Li_2CO_3 present in samples resulted in decreased capacity retention. The relative amount of Li_2CO_3 is taken as the ratio of Li_2CO_3 to C-C peaks. To obtain this ratio, peak fitting of the C1s spectra was done with gaussian functions. Li_2CO_3 to C-C peak ratios are listed in Table 3.2. The Li_2CO_3 to C-C peak in x = 0 electrodes cycled in an FEC containing electrolyte increases from 0.91 ± 0.17 to 2.56 ± 0.45 when the same electrode was cycled in electrolyte without FEC. The same trend was also observed for x = 6 electrodes, where the Li_2CO_3 to C-C peak ratios were 0.40 ± 0.09 and 0.95 ± 0.21 in FEC containing and FEC free electrolytes, respectively.

Table 3.2. Li_2CO_3 to C-C peak ratios from the C1s spectra of $Si_{40'}(FeSi_2)_{(60-x)'}(LiF)_{(x)'}$ electrodes for x = 0 and 6.

$Si_{40'}(FeSi_2)_{(60-x)'}(LiF)_{(x)'}$	FEC containing electrolyte $(Li_2CO_3)/(C-C)$ ratio	FEC-free electrolyte $(Li_2CO_3)/(C-C)$ ratio
x = 0	0.91 ± 0.17	2.56 ± 0.45
x = 6	0.40 ± 0.09	0.95 ± 0.21

When comparing the XPS data to the cycling data on the same electrode composition, it is seen that electrodes with a higher Li_2CO_3 to C-C peak ratio had a lower capacity retention. Both x = 0 and x = 6 electrodes exhibit higher capacity retention when cycled in cells with FEC containing electrolyte. These electrodes also show lower Li_2CO_3 to C-C peak ratios relative to the same electrodes cycled in cells with FEC free electrolyte. Cells made with x = 6 electrodes show higher capacity retention than x = 0 electrode containing cells, and x = 6 electrodes show lower Li_2CO_3 to C-C peak ratios relative to x = 0 electrodes. These observations suggest that both LiF incorporation into the electrode and FEC addition into the electrolyte aid in forming a SEI with lower amounts of Li_2CO_3, which leads to increased capacity retention during cycling.

3.3 Li_2CO_3

Another major component of the SEI originating from the decomposition of FEC or VC is Li_2CO_3. Li_2CO_3 was also investigated as a multifunctional alloy component. Ball milled $Si_{40'}(FeSi_2)_{(60-x)'}(Li_2CO_3)_{(x)'}$ alloys were prepared such that their theoretical volume expansion upon full lithiation was 112%.

3.3.1 Experimental

Si-$FeSi_2$-Li_2CO_3 alloys were prepared from Si (99%, -325 mesh, Sigma-Aldrich), Fe (99.9%, -325 mesh, Sigma-Aldrich) and Li_2CO_3 (99%, powder, Alfa-Aesar). Initially, the alloys were prepared by loading all three components and ball milling simultaneously; however, like the findings of LiF alloys, Li_2CO_3 inhibited the mechanochemical reaction of Si and Fe. The two-step ball milling procedure was used again, where Si and Fe were first milled for 8 hours, followed by the addition of Li_2CO_3 and an additional 8 hours of milling. XRD patterns were collected using a Rigaku Ultima IV diffractometer with a Cu Kα x-ray source operating at 40 kV and 45 mA and a diffracted beam graphite monochromator.

Electrode slurries were prepared with the same recipe as the $Si_{40'}(FeSi_2)_{(60-x)'}(LiF)_{(x)'}$ electrodes by mixing a 70:5:25 weight ratio of alloy:carbon black:PI in NMP. Slurries were mixed and subsequently coated onto electrolytic copper foil in the same methods as the $Si_{40'}(FeSi_2)_{(60-x)'}(LiF)_{(x)'}$ electrodes, to the slurry thickness of 0.102 mm. Electrodes were assembled into 2325-type coin cells with a lithium foil counter/reference electrode in electrolyte consisting of 1 M $LiPF_6$ in (v:v) (3:6:1) EC:DEC:FEC.

3.3.2 **Results and Discussion**

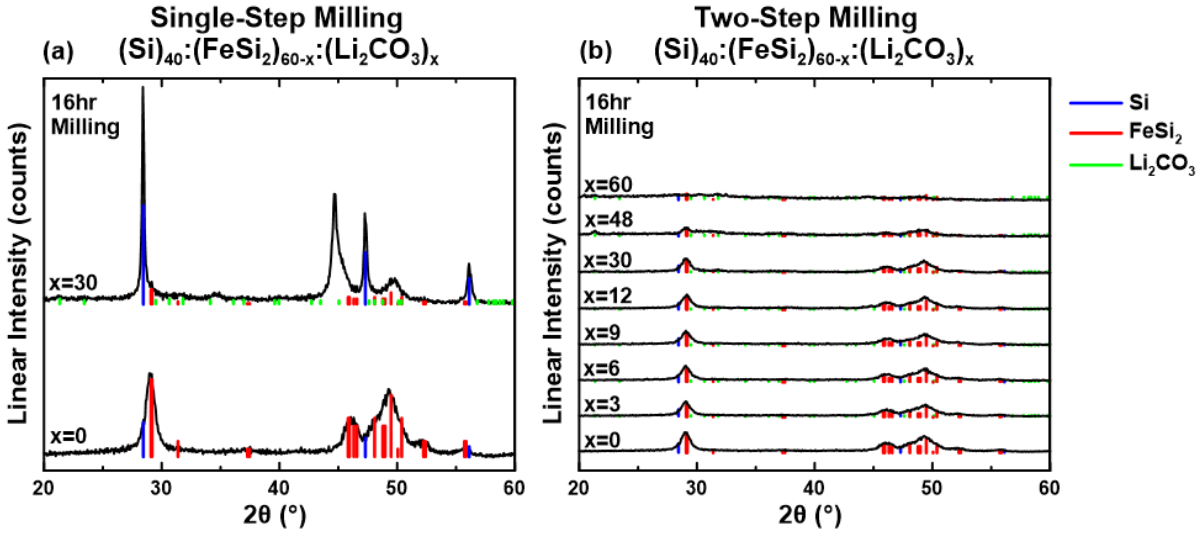

Figure 3.11. XRD patterns of $Si_{40'}(FeSi_2)_{(60-x)'}(Li_2CO_3)_{(x)'}$ prepared by (a) milling in a single step, and (b) milling in two-steps.

XRD patterns of ball milled $Si_{40'}(FeSi_2)_{(60-x)'}(Li_2CO_3)_{(x)'}$ alloys are shown in Figure 3.11. There was a substantial reaction between Li_2CO_3 and Si forming unknown products. As Li_2CO_3 content is increased features in the XRD pattern are broadened such that an amorphous XRD pattern is observed.

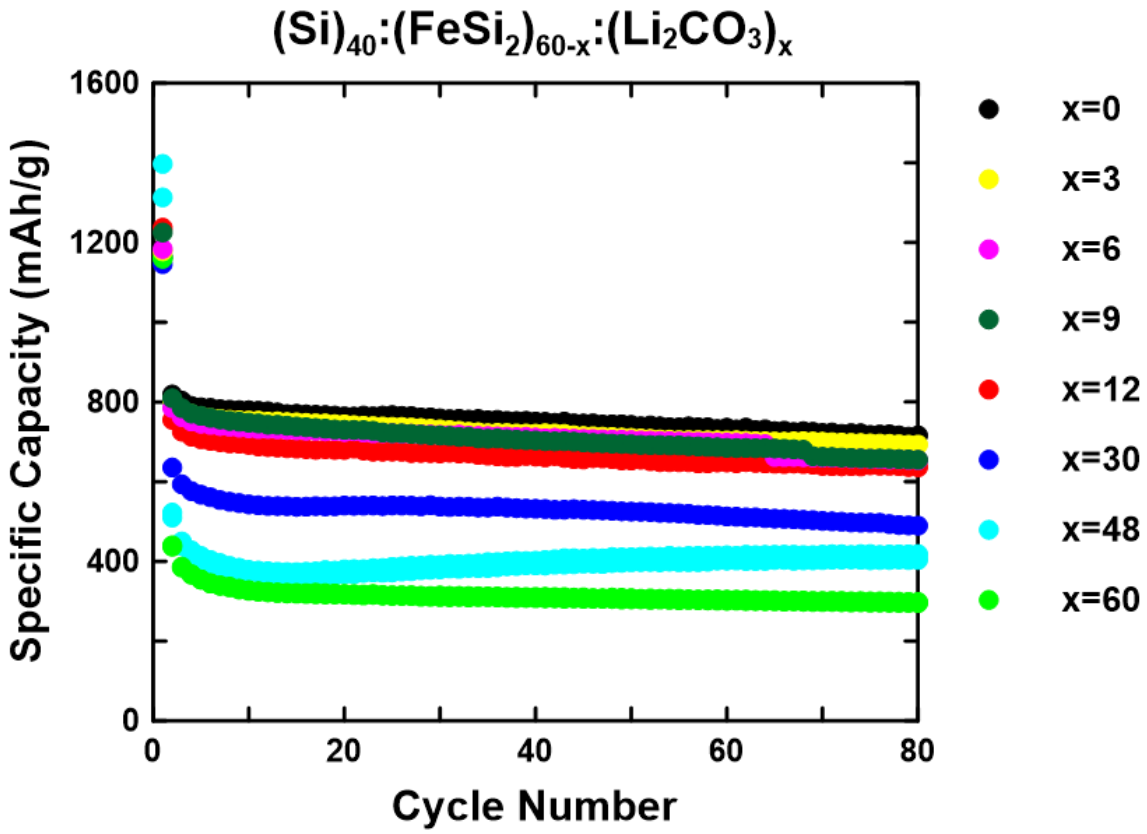

Figure 3.12. Specific capacity vs cycle number of $Si_{40'}(FeSi_2)_{(60-x)'}(Li_2CO_3)_{(x)'}$ electrodes.

$Si_{40'}(FeSi_2)_{(60-x)'}(Li_2CO_3)_{(x)'}$ electrodes were then evaluated in Li half cells shown in Figure 3.12. With increased Li_2CO_3 content, a decrease in capacity is observed. This indicates that active Si has likely reacted with Li_2CO_3 to form inactive products. Additionally, capacity retention was reduced for Li_2CO_3 contents below x = 9. As a result of poor electrochemical performance as Li_2CO_3 content was increased, further evaluation of $Si_{40'}(FeSi_2)_{(60-x)'}(Li_2CO_3)_{(x)'}$ alloys was not performed.

3.4 Conclusions

Both Li_2CO_3 and LiF were added to Si-Fe alloys to act as an inactive alloy component and to enhance SEI formation. Li_2CO_3 was found to react with active Si during ball milling, resulting in severe capacity reduction. In the case of LiF, no such reaction occurred, however it was

found that in order to maintain a nanocrystalline microstructure, it was necessary to first ball mill the Si and Fe components of the alloy and then incorporate LiF in a second ball milling step. $Si_{40'}(FeSi_2)_{(60-x)'}(LiF)_{(x)'}$ alloys showed improved electrochemical performance and capacity retention when x= 3, 6, and 9. It was also shown that when LiF was added as a slurry additive to electrodes containing Si-Fe alloys, improved cycling performance could also be achieved when FEC was also present in the electrolyte, however the improvement was not as great as when the LiF was incorporated directly into the Si-Fe alloy. The addition of electrode additives by ball milling or as a slurry additive may be valuable methods for improving electrochemical performance that can be used in conjunction with more traditional alloy compatible binders and liquid electrolyte additives.

CHAPTER 4. BINDER ADDITIVES

4.1 Introduction

Binders in Li-ion electrodes are important for maintaining cohesion of the electrode materials as well as ensuring good adhesion to the current collector. The binder is important for maintaining electrode coating integrity during handling but also contributes to good electrochemical performance. For Si-alloy negative electrode material, the choice of binder is especially important because there is a large volume expansion and contraction of the active material particles during lithiation and de-lithiation respectively.

During lithiation, the active electrode particles expand, resulting in compressive stress, which helps maintain electrical contact between the active particles and the current collector is maintained. However, subsequent de-lithiation causes contraction of the active particles. If the binder does not have adequate adhesion to the active particles, mechanical failure of the electrode coating and loss of electrical contact can result.

The choice of binder is directly correlated with electrochemical performance of Si negative electrodes. Ideal binders for Si-alloy materials should have adequate adhesion and cohesion between active material particles and the current collector, the ability to endure volume expansion during cycling, and the ability to coat the surface of active material particles to limit continuous SEI growth.[12]

For example, a conventional polyvinylidene fluoride (PVDF) binder used in negative electrodes is not a great binder for use in Si-alloy material. PVDF binder forms a network of polymer fibers that surround the active particles rather than forming a surface coating.[12,81] This fibrous

network means that a majority of the active particle surface is still exposed to electrolyte and will therefore react, increasing electrode impedance, and even isolating active particles.[12] PVDF also experiences dramatic swelling when exposed to electrolyte, compromising the electrodes mechanical integrity, and leading to loss of electrical contact.[82]

FEC, a popular additive mentioned before, produces an SEI composed predominantly of LiF. The reduction mechanism of FEC proposed by Alison L. Michan et al. suggests that FEC reduces to form LiF and VC, followed by subsequent reduction of the VC to polymerized VC (poly-VC).[83] Poly-VC consists of repeating EC units, shown in Figure 4.2. FEC containing electrolytes are used in Si-alloy negative electrodes to prevent the decomposition of electrolyte salts and solvents by forming a stable SEI layer. In Chapter 3, LiF was used as an electrode additive to mimic the effect of FEC in increasing the LiF content in the SEI. However, this ignores the poly-VC component to the SEI that results from FEC reduction. Poly-VC should be electrochemically stable as a polymer binder in Li-ion negative electrodes and therefore could contribute to the good cycling properties of Si negative electrodes in FEC containing electrolytes. Since poly-VC is structurally similar to a FEC or VC based SEI layer, it is speculated to have a multifunctional role.[84] Poly-VC formed by the reduction of FEC may aid in the mechanical integrity of the Si-alloy material while facilitating the formation of a stable SEI. In this chapter the use of poly-VC as a binder additive was explored to see if its presence could enhance the cycling of Si-alloy electrodes.

4.2 Polymerized VC

Polymerized VC or poly-VC is a common component in the SEI of Li-ion cells with electrolytes containing FEC or VC. Both FEC and VC are popular electrolyte additives that aid in the performance of Li-ion cells. When used as electrolyte additives, VC and FEC decompose before the bulk of the electrolyte to form a stable SEI and limit parasitic reactions. Poly-VC is a major component in the reduction of these popular additives and is thought to facilitate the formation of a stable SEI.

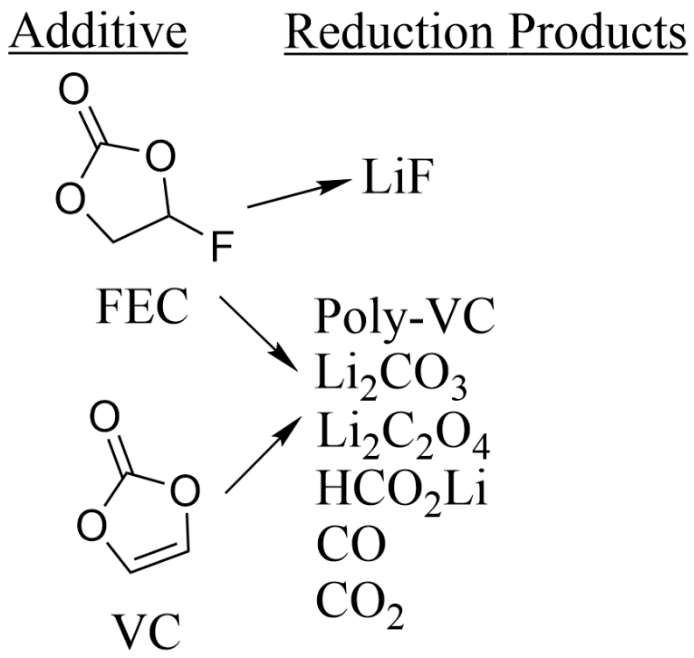

Figure 4.1. The chemical structure of FEC and VC and their major decomposition products.

Poly-VC was tested as a binder for graphite based negative electrodes in Li-ion cells by Hui Zhao et al.[84] They show that poly-VC functions as a traditional binder while also aiding in surface stabilization in propylene carbonate (PC) based electrolytes. Graphite based electrodes are prone to exfoliation in PC based electrolytes, but the use of poly-VC as a binder rather than PVDF binder allowed for enhanced cycling performance.[84] In an electrolyte containing 30%

PC, cells with poly-VC binder had a reversible specific capacity of 170 mAh/g while cells with PVDF binder failed to cycle.[84]

In this work, the effects of poly-VC as a binder additive and as a neat binder in Si-Fe alloy material is studied. The experiments build off the work in Chapter 3 with the use of $Si_{(40)}(FeSi_2)_{(54)}(LiF)_{(6)}$ as the active material. It is thought that poly-VC binder may play a multifunctional role in the Si-Fe alloy electrodes, acting as a binder and stabilizing component to the formed SEI.

4.2.1 Experimental

Poly-VC was synthesized in the Speed lab with the aid of Professor Alex Speed. Poly-VC was synthesized by starting with vinylene carbonate (VC, BASF) which is commonly used as an electrolyte additive. The VC is purified by running it through an alumina column, removing stabilizers. 5 g of purified VC and 0.095 g of azobisisobutyronitrile (AIBN, 98%, Sigma-Aldrich) were added to a 25 mL Schlenk flask set up in the fume hood. The Schlenk flask was degassed, before adding solvent by performing three cycles of freeze-pump-thaw. The flask was then immersed into a 70 °C oil bath and left to react overnight. After the overnight reaction, the reactants were dissolved in n-methyl-2-pyrrolidinone (NMP, 99.5%, Sigma-Aldrich) then precipitated with diethyl ether in a vacuum rotation evaporator. These steps are similar to the synthesis used by Hui Zhao et al. with the replacement of NMP in place of dimethylformamide (DMF, 99.8%, <50 ppm H_2O, Sigma-Aldrich).[84] This exchange was made because NMP is the solvent used in creating the electrode slurries, thus NMP impurities would have no detrimental effect to the results of the experiments.

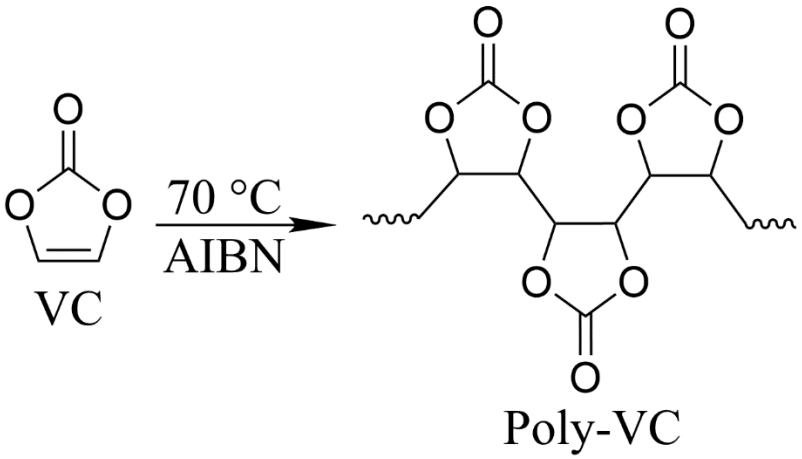

Figure 4.2. The synthesis and chemical structure of polymerized vinylene carbonate.

Electrodes were prepared by mixing a 70:5:25 weight ratio of alloy:carbon black (Imerys Graphite and Carbon, Super C65):binder in NMP. The alloys used were the $Si_{40'}(FeSi_2)_{(60-x)'}(LiF)_{(x)'}$ alloys where x = 0 and x = 6 alloys described in Chapter 3. These $Si_{40'}(FeSi_2)_{(60-x)'}(LiF)_{(x)'}$ alloys were prepared via the two-step ball milling procedure described in Section 3.2.1. The binders used were aromatic polyimide (PI) and poly-VC. PI was added in the form of a 20% (w:w) solution of poly(amic acids) in NMP (Hitachi DuPont MicroSystems, LLC). These electrodes were cycled against a lithium foil counter/reference electrode with electrolyte consisting of 1M $LiPF_6$ in (v:v) (3:6:1) EC:DEC:FEC and the same composition without FEC. For a further description of electrode preparation, cycling conditions, and coin cell assembly please refer to Chapter 2 sections 2.2, 2.3, and 2.3.1 respectively.

4.2.2 Results and Discussion

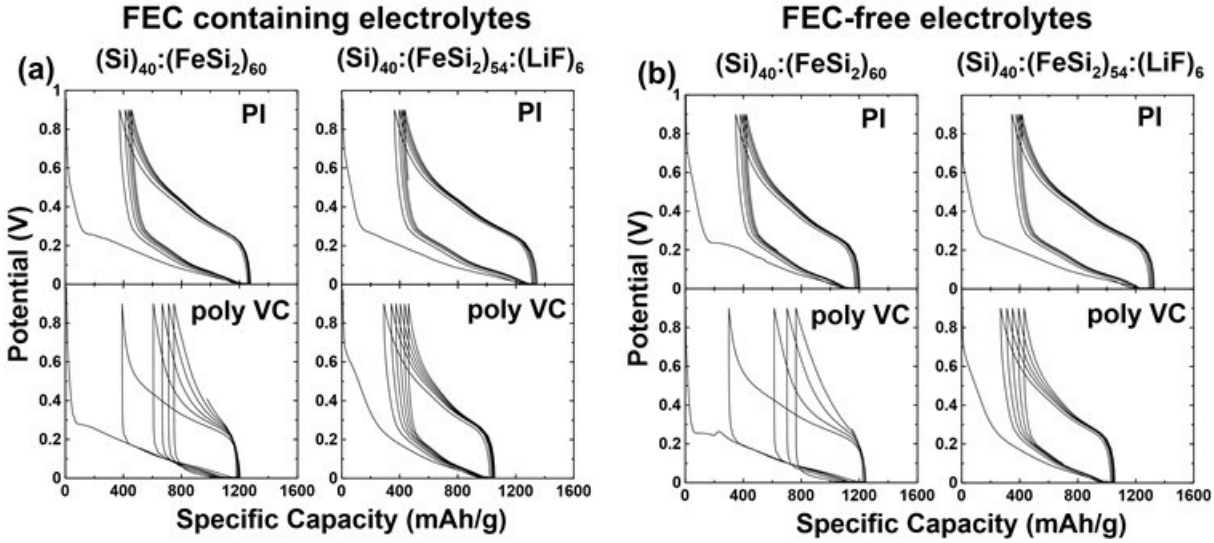

Figure 4.3 Potential profiles of $Si_{40'}(FeSi_2)_{(60)'}$ and $Si_{40'}(FeSi_2)_{(54)'}(LiF)_{(6)'}$ electrodes with PI, poly-VC, and poly-VC:PI(50:50) binders. Cycled with FEC containing electrolyte (a) and FEC-free electrolyte (b).

Figure 4.3 shows the potential profiles of $Si_{40'}(FeSi_2)_{(60)'}$ and $Si_{40'}(FeSi_2)_{(54)'}(LiF)_{(6)'}$ electrodes with PI and poly-VC binders. All electrodes with PI binder have substantial initial capacity between 0.8 V and 0.3 V during their first lithiation. PI binder is expected to have a capacity plateau here, as it has been previously observed that aromatic-PI undergoes reduction until it becomes fully carbonized at low potentials in Li-ion cells.[62] Reduction is not expected to occur for poly-VC, which is aliphatic and, accordingly, no significant capacity is observed for poly-VC containing $Si_{40'}(FeSi_2)_{(60)'}$ electrodes during their initial lithiation between 0.8 V and 0.3 V. However, substantial initial capacity in this range is observed for poly-VC electrodes with $Si_{40'}(FeSi_2)_{(54)'}(LiF)_{(6)'}$. This initial capacity is suspected to be from the reduction of H_2O. If the poly-VC binder does not fully coat the alloy particles or is otherwise permeable to water, then when hygroscopic LiF is present, substantial water may be absorbed by the alloy during the coating process in air which may not be removed during the 120 °C drying process.

In the case of PI, the additional curing step of heating to 300 °C for 4 hours could have removed any absorbed H_2O. Additionally, PI is known to form a conformal coating around alloy materials. This may create a protective layer around the active particles which could prevent the LiF from absorbing H_2O.[85] This would explain why the potential profiles for $Si_{40'}(FeSi_2)_{(54)'}(LiF)_{(6)'}$ electrodes with PI are quite similar to $Si_{40'}(FeSi_2)_{(60)'}$ electrodes with PI.

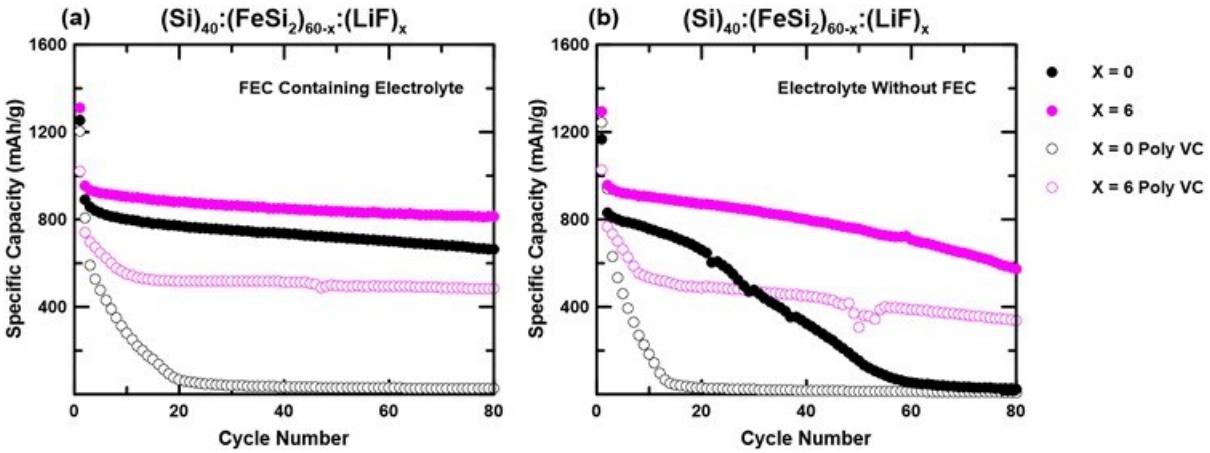

Figure 4.4 Cycling of $Si_{(40)'}(FeSi_2)_{(60-x)'}(LiF)_{(x)'}$ (x = 0 and x = 6) electrodes containing PI and poly-VC with FEC containing electrolyte (a) and electrolyte without FEC (b).

Figures 4.4(a) and 4.4(b) show the specific capacity vs. cycle number of half cells with $Si_{(40)'}(FeSi_2)_{(60-x)'}(LiF)_{(x)'}$ (x = 0 and x = 6) electrodes with PI binder and poly-VC binder. The electrodes were tested with and without FEC to determine if poly-VC was able to aid in the capacity retention to the same extent as FEC containing electrolytes. In Figure 4.4(a), the cells with FEC containing electrolyte, it is observed that no cell performed as well as the one with the PI binder electrode. It is also seen that poly-VC binders performed the worst, with the $Si_{(40)'}(FeSi_2)_{(54)'}(LiF)_{(6)'}$ cell containing poly-VC binder outperforming the $Si_{(40)'}(FeSi_2)_{(60)'}$ alloy containing poly-VC binder.

Figure 4.4(b) shows the same cells as in Figure 4.4(a), excepting without FEC additive. As previously observed, the presence of LiF improved cycling in all cases. When LiF was present, poly-VC resulted in increased capacity fade. However, when LiF was not present,

electrodes with poly-VC failed rapidly. This illustrates that poly-VC alone can not be utilized as a binder for Si-alloy electrodes. Its effect on cycling performance is not as great as the presence of LiF and much greater improvements can be realized if FEC is used as an electrolyte additive instead.

4.3 Conclusions

Poly-VC is shown to be a poor binder in $Si_{(40)'}(FeSi_2)_{(60)'}$ cells with the specific capacity reducing to ~0mAh/g for $Si_{(40)'}(FeSi_2)_{(60)'}$ cells with poly-VC binder in FEC containing electrolyte and electrolytes without FEC at 20 cycles and 13 cycles, respectively. It is observed that no cell in the series tested performed as well as $Si_{(40)'}(FeSi_2)_{(54)'}(LiF)_{(6)'}$ with PI binder. The $Si_{(40)'}(FeSi_2)_{(54)'}(LiF)_{(6)'}$ cell containing poly-VC binder also shows higher capacity retention than $Si_{(40)'}(FeSi_2)_{(60)'}$ cells with PI binder in electrolytes without FEC. However, the use of poly-VC binder was judged not to be as effective a strategy for improving the cycling of Si-alloy material when compared to the use of state-of-the-art binders and electrolyte additives. To explore the effects of poly-VC on SEI formation, poly-VC should be mixed with another binder in future work to determine if there is an ideal amount of poly-VC to add that will act to replace the use of FEC in $Si_{(40)'}(FeSi_2)_{(54)'}(LiF)_{(6)'}$ electrodes.

CHAPTER 5. WATER AS AN ELECTROLYTE ADDITIVE FOR NMC/Si-ALLOY Li-ION CELLS[2]

5.1 Introduction

The advancement of current electrolyte systems is focused on the discovery of solvent additives which account for less than 10% the weight of the bulk solvent while drastically altering a cells performance and lifetime.[27] Additives are preferentially involved in interfacial redox reactions, reducing or oxidizing before the bulk of the electrolyte to limit parasitic reactions in later cycles. The decomposition of additives contributes to the formation, morphology, and composition of the SEI. Addivitves play a critcal role in the design of advanced Li-ion cells, but as the technology progresses, researchers will continue to reduce costs and increase efficencies. FEC is one additive that has become the standard in the field, resulting in dramatic improvements in alloy electrode cycle life.

The effectiveness FEC in improving Si-alloy cycling performance has been attributed both to its formation of an LiF rich SEI and to the formation of organic polymers (particularly poly-vinylene carbonate) also as SEI components. However, FEC has significant disadvantages: FEC has a higher cost than conventional electrolyte solvents and it is continually consumed

---

[2] The work in Chapter 5 has been submitted for publication as: R. S. Young, H. Yu, and M. N. Obrovac, Enhancing NMC/silicon alloy full cell cycling by adding water to the electrolyte, J. Appl. Electrochem. (under review). All cycling, and XPS is content from this article. R.S. Young prepared all XPS samples and built the coin cells used for XPS. H. Yu produced all the coatings, built all the cells for cycling, and performed Karl Fischer titration on the electrolytes.

during alloy cycling, thereby requiring larger amounts if a long cycle life is desired.[86] For these reasons, the required use of FEC is an obstacle for the commercialization of alloy electrodes. Recently, inexpensive alternatives to FEC have been proposed. For instance, CO_2 has been shown to be an excellent additive for the enhancement of silicon alloy cycling with similar performance as FEC.[55] A higher CO_2 content was found to sustain a longer cycle life. However, since the CO_2 solubility in electrolyte is low, there are few practical methods to introduce a sufficient amount CO_2 into LIBs.

To maximize the CO_2 content in silicon alloy cells, in-situ gas generation is a promising method. Typically, internal gas generation is thought to be detrimental and therefore, efforts are generally focused on gas suppression. However, considering the improvements in cycling observed from intentionally adding CO_2 to cells containing Si-alloys, in the case of Si-alloy electrodes, internal CO_2 gas generation may be beneficial for cycling. One source of CO_2 generation in Li-ion cells is via reaction of ethylene carbonate (EC) with OH^-.[87]

$$OH^- + C_3H_4O_3 \rightarrow C_2H_5O_2^- + CO_2 \quad (5.1)$$

Where the OH^- is generated via H_2O reduction at the negative electrode. This reaction is auto-catalyzed, since the $C_2H_5O_2^-$ formed can further react with EC to produce more CO_2 via the following reaction:

$$C_2H_5O_2^- + C_3H_4O_3 \rightarrow HO(C_2H_4O)_2^- + CO_2 \quad (5.2)$$

Therefore, a small amount of trace H_2O in the electrolyte has the potential of considerable amounts of CO_2. CO_2 may also be generated at the positive electrode.

In the case of $LiCoO_2$ (LCO)/graphite cells, the onset of CO_2 generation is usually around 3 V, but the amount of CO_2 is minimal.[88] In contrast, CO_2 formation is considerable if Mn or Ni are present in the positive electrode, even at a low potentials between 3.6 V and 4.1 V.[88] Gasteiger et al. conducted a comprehensive study on the origin of CO_2 generation on the surface of lithium nickel manganese oxide positive electrodes (NMCs) and concluded that oxygen release from NMC is associated with CO_2 generation[89], as opposed to the previous consensus that lithium carbonate impurities produced the CO_2.[90] They proposed a mechanism that in the aid of free oxygen produced from NMC decomposition, EC will decompose and produce both CO and CO_2 as shown in the equation below.

$$C_3H_4O_3 + 2O_2 \rightarrow CO + 2CO_2 + 2H_2O \qquad (5.3)$$

Reaction 5.3 produces H_2O, which may lead to further CO_2 production at the negative electrode, according to equations (5.1) and (5.2). From the above reactions, the presence of water in electrolyte and the use of an NMC positive electrode are both associated with the generation of CO_2 in Li-ion cells during cycling.

5.2 Water Additive

Two of the main reduction products of FEC are vinylene carbonate (VC) and LiF.[83] The subsequent decomposition products of VC include HCO_2Li, $Li_2C_2O_4$, polymerized VC, and Li_2CO_3.[83] The added H_2O will provide similar reduction products via the following proposed reaction scheme.[55]

$$2CO_2 + 2e^- + 2Li^+ \rightarrow CO + Li_2CO_3 \qquad (5.4)$$

$$LiPF_6 \leftrightarrow LiF + PF_5\ ;\ PF_5 + H_2O \rightarrow 2HF + PF_3O \qquad (5.5)$$

$$PF_3O + ne^- + nLi^+ \rightarrow LiF + Li_xPOF_y \quad (5.6)$$

From the above considerations, small amounts of H_2O could be beneficial for Si-negative electrode cycling in cells with an NMC positive electrode. However, presence of H_2O in Li-ion cells is typically considered to be detrimental. Li-ion cells typically contain less than 50 ppm of water and H_2O impurities have been shown to have negative effects on cycling due to unwanted reactions with some active electrodes and electrolyte, especially in conjunction with $LiPF_6$ in which products such as H_2 and HF are formed.[91–94] HF can increase capacity fade of $LiCoO_2$ electrodes,[95] but is said to have a beneficial impact on the SEI formation of Si electrodes.[96] In other work, $LiCoO_2$ and $Li[Ni_{0.42}Mn_{0.42}Co_{0.16}]O_2$ vs graphite as well as $LiCoO_2$ vs $Li_4Ti_5O_{12}$ cells with up to 1000ppm of water had no detrimental effects on cycling other than the swelling caused by gas production.[97–99]

In this work, water was added to NMC/silicon alloy and LCO/silicon alloy full cells to intentionally cause CO_2 and LiF generation, for the purpose of improving cycling of full cells with Si-alloy electrodes. By this method it is shown that H_2O is an effective additive in full NMC/silicon alloy Li-ion cells, and that it is just as effective as FEC.

5.2.1 Experimental

Silicon alloy negative electrodes consisted of V6 silicon alloy (3M), SFG6L (Imerys Graphite and Carbon), carbon black (CB, Super C65, Imerys Graphite and Carbon), and a 10 wt% aqueous solution of LiPAA (made by neutralizing PAA solution (Sigma-Aldrich, average molecular weight~250,000 g mol^{-1}, 35 wt% in H_2O) with $LiOH{\cdot}H_2O$ (Sigma Aldrich, 98%) in a weight ratio of 44:44:2:10 in distilled water. These components were thoroughly mixed in with three 0.5-inch tungsten carbide balls in a planetary mixer (PM200, Retsch) at 100 rpm for

60 minutes to create a uniform slurry. The slurry was coated onto copper foil (Furukawa) and dried at 120 °C in air for 1 h. These electrodes had a nominal capacity of 650 mAh g^{-1} and a capacity loading of 2.7 mAh cm^{-2}.

NMC positive electrodes were made by NOVONIX Battery Technology Solutions Inc., Bedford, Nova Scotia, Canada using $LiNi_{0.3}Mn_{0.3}Co_{0.3}O_2$. $LiCoO_2$ (LCO) electrodes were made using $LiCoO_2$, PVDF, and carbon black in a weight ratio of 94:3:3 with n-methyl-2-pyrrolidone (NMP, 99.5 %, Aldrich) used as a slurry solvent. The slurry was mixed using the same conditions as the negative electrode slurries, then coated onto aluminum foil and dried at 120 °C in air for 1 h. All hand coated electrodes were calendered by an adjustable gap calender with 6 in. diameter rolls (DPM Solutions, Nova Scotia, Canada) to achieve a porosity of 20-30%. All coatings were punched into 2.52 cm^2 circular disk electrodes. NMC and LCO electrodes had a nominal capacity of 170 mAh g^{-1} and a capacity loading of 2.4 mAh cm^{-2} at 4.4 V vs Li.

Full coin cells were assembled using an electrode alignment jig, to ensure proper alignment of the positive and negative electrodes. Duplicate cells were made to ensure the accuracy of results. The full cell electrode capacity balance was N/P = 1.13. These full coin cells were filled with 1 M $LiPF_6$ in ethylene carbonate (EC):diethylene carbonate (DEC) (1:2 v/v) electrolyte (control) with the optional addition of 10 vol% FEC or water (500 or 1000 ppm). In order to verify the added water content, the Karl Fischer titration was conducted by a MSc student in the Obrovac lab. The student, Haonan Yu, conducted Karl Fischer titration to obtain the actual water content in electrolyte samples. Karl Fischer results were consistent with estimated water content with only 10% error. All electrolyte salts and solvents were obtained from BASF. Cells were cycled at 30.0 ± 0.1 °C with a Maccor Series 4000 Automated Test System between 3 to 4.4 V galvanostatically at 0.1C for the first cycle and 0.2C for subsequent cycles.

X-ray photoelectron spectroscopy (XPS) measurements of the negative and positive electrodes of NMC-V6/SFG6L full cells were performed in both pristine and post-formation (after 3 cycles) states. All samples were prepped in an argon-filled glove box. Preparation of the sample involved disassembling the coin cells to extract the electrodes, rinsing the electrodes with DEC to remove impurities, and allowing the electrodes to dry in the glove box overnight. After drying, the samples were transported to the spectrometer in airtight argon-filled bags to limit exposure to the atmosphere to be processed by Andrew George from the Department of Physics and Atmospheric Science at Dalhousie University. The F1s, C1s, and O1s spectra were focused on to analyze the species present in the SEI. Various levels of surface charging were observed in the samples, shifting the peaks. To account for surface charging, the F1s spectra were aligned using the LiF F1s peak, the C1s spectra were aligned using the C-C bond C1s peak, and the O1s spectra were aligned using the Li_2CO_3 O1s peak.

5.2.2 Results and Discussion

Figure 5.1(a) shows the first and second cycle potential profiles of NMC-V6/SFG6L full cells with EC-DEC baseline electrolyte solvent and with electrolytes with additives as indicated. Corresponding differential capacity curves are shown in Figure 5.1(b). The addition of 10% FEC to the baseline electrolyte results in additional irreversible capacity near 4 V, due to the reduction of FEC at the negative electrode.

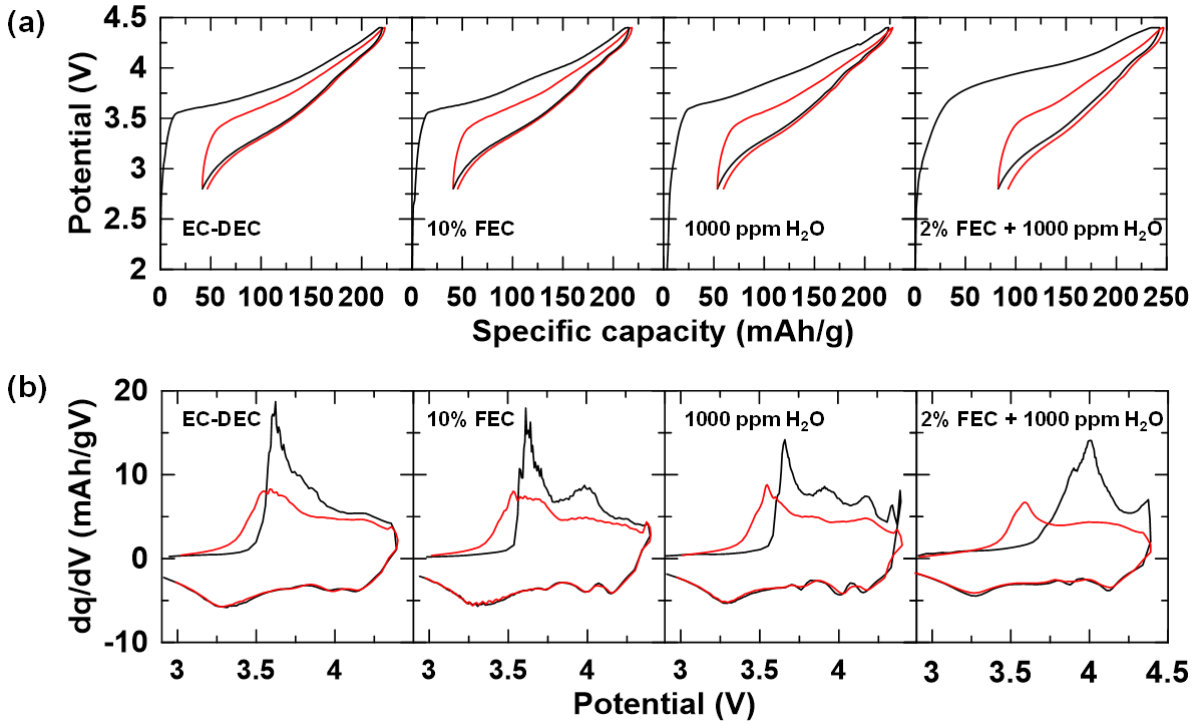

Figure 5.1. (a) Potential-capacity and (b) differential capacity curves of NMC-V6/SFG6L full cells with EC-DEC baseline solvent electrolyte and with different electrolyte additives, as indicated. 1st (black) and 2nd (red) cycles are shown.

The addition of H_2O results in two additional peaks in the first charge differential capacity, at about 3.8 V and 4.3 V. The origin of these peaks are not known; however, their potentials are consistent with potentials corresponding to the oxidation of organic carbonates to produce CO_2 and electrolyte reduction at the negative electrode, respectively.[100] No evidence of water reduction is observed, which should occur at low cell potentials (i.e. < 3.5 V).[100] The second cycle differential capacities of the baseline, and 10% FEC and 1000 ppm H_2O additive cells are similar, except that cell polarization is slightly less and peaks/plateaus from graphite staging are more apparent during discharge in the cells with 10% FEC and 1000 ppm H_2O additives. This may be due to the additives forming a thinner, lower impedance SEI, compared to the baseline electrolyte. Combining FEC and H_2O results in a large increase in irreversible capacity and a large peak in the first cycle differential capacity near 4 V.

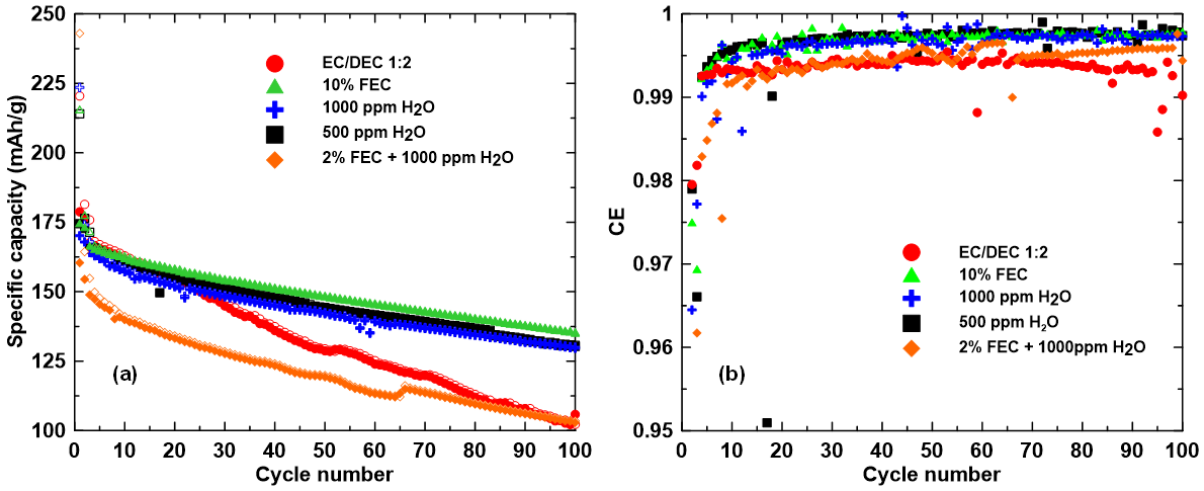

Figure 5.2. (a) The cycling performance and (b) coulombic efficiency of NMC-V6/SFG6L full cells with different additives.

Figure 5.2(a) shows the cycling performance of the NMC-V6/SFG6L full cells. As expected, the baseline cell with no additive has poor capacity retention (59 %/100 cycles), due to continual electrolyte reactions at the alloy surface. The addition of 10% FEC results in an 18% improvement in capacity retention (77%/100 cycles). This is also expected, since FEC is well known for improving the cycling performance of alloy cells by forming an efficient SEI layer on alloy surfaces to reduce reactivity with electrolytes. Surprisingly, the cell with 1000 ppm water has a capacity retention that is nearly the same as the cell with FEC additive (76%/100 cycles). However, this cell's irreversible capacity is slightly higher than the FEC cell, likely due to irreversible reactions caused by the large quantity of water in the electrolyte. Due to the Li-loss associated with this irreversible capacity, the reversible capacity of the 1000 ppm H_2O cell is accordingly lower than the FEC cell by an amount that closely corresponds with its excess irreversible capacity. Reducing the water content to 500 ppm lowers the first cycle irreversible capacity and increases the reversible capacity, with no degradation in capacity loss. It is not known how little water is needed to maintain this improved cycling effect. Combining FEC and water additives results in the highest capacity fade. Considering the significant changes in

the differential capacity that occurred in this cell, this electrolyte combination may be causing excessive gas production or irreversible damage to the active materials (e.g. via the formation of HF). Figure 5.2(b) shows the coulombic efficiency (CE) of the NMC/alloy cells as a function of cycle number. The differences in cycle life are reflected in the CE, with the FEC and water additive cells achieving similarly high CE values of about 99.8%, while the EC/DEC baseline and 2% FEC + 1000 ppm H_2O cells having lower CE values of about 99.4%.

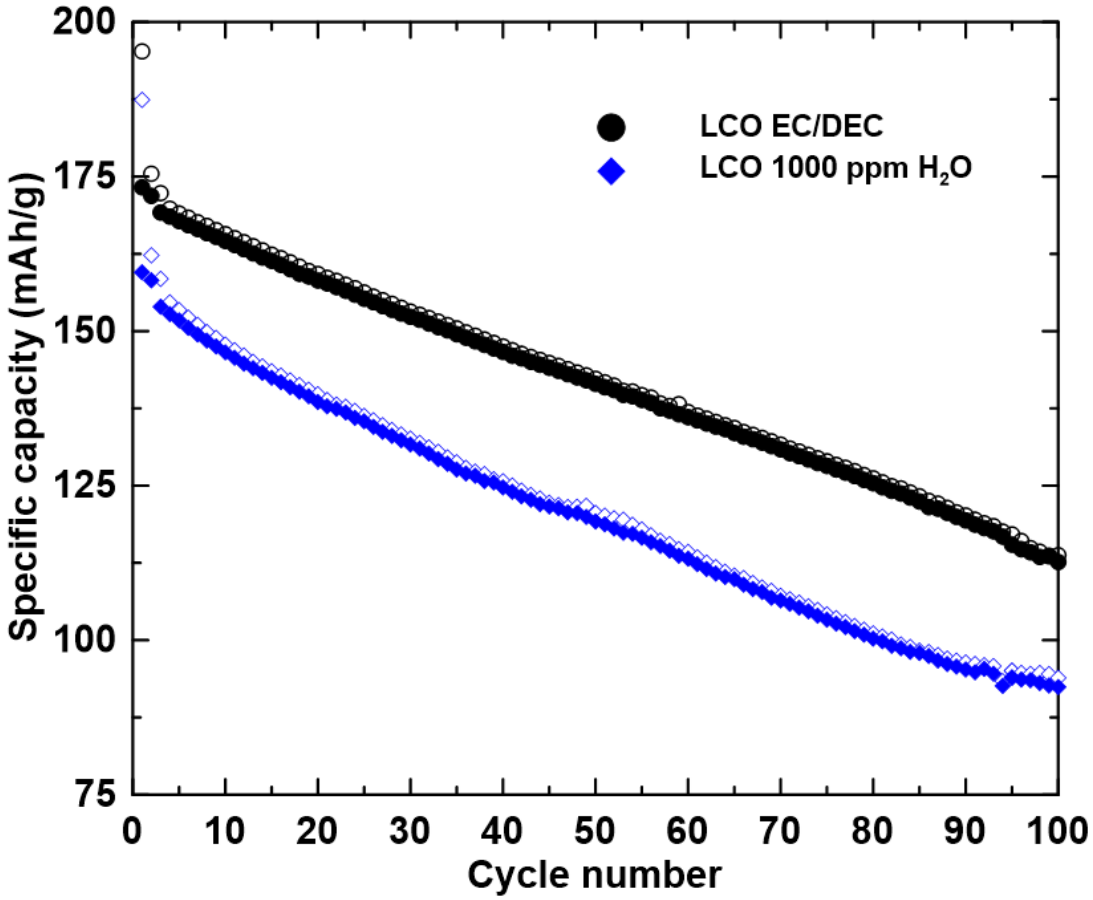

Figure 5.3. The cycling performance of LCO-V6/SFG6L full cells with and without water additive.

Figure 5.3 demonstrates the effects of water additive for alloy cells with LCO positive electrodes. When there is no water additive present, the cells with LCO positive electrode have a similar capacity fading trend as NMC. However, in contrast to the NMC cells, when water is added to the electrolyte in LCO cells, a significant reduction in capacity and cycling retention

results. These results suggest that the positive electrode may be involved in forming an intermediate species that subsequently enhances the SEI at the negative electrode. It is speculated that NMC may act as a catalyst for the production of CO_2, while this reaction appears to be prohibited in cells with LCO positive electrode. However, CO_2(g) has yet to be detected in the electrolyte of cycled cells with water added using gas chromatography. It is expected that any reaction products made by the H_2O additive are likely incorporated in the SEI, which would make them difficult to detect in the electrolyte solution.

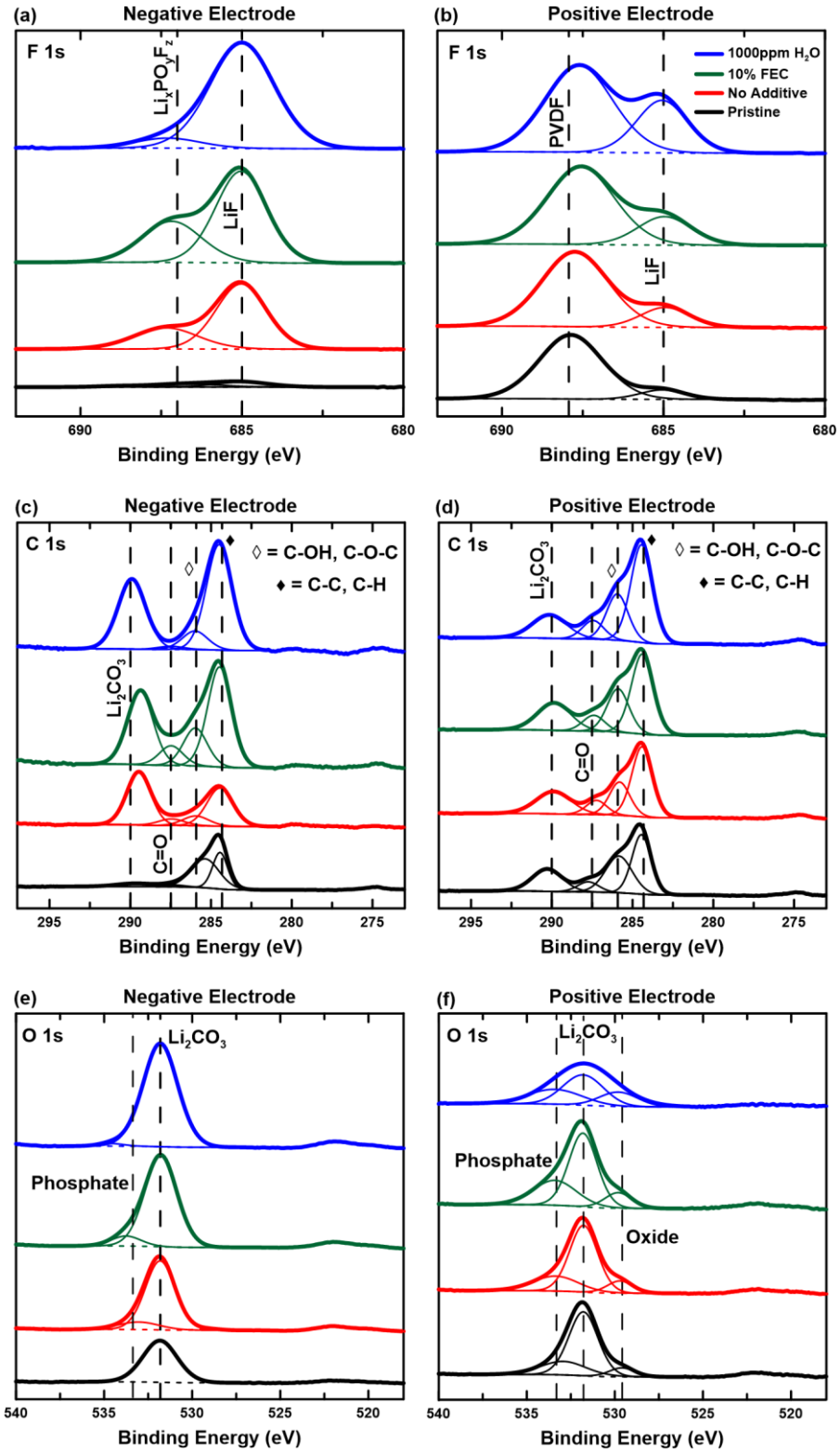

Figure 5.4. Post formation XPS F 1s, C1s, and O1s spectra for negative electrodes (a,c,b) and positive electrodes (b,d,f) of NMC-V6/SFG6L full cells with 1 M $LiPF_6$ in EC:DEC (1:2 v/v) electrolyte with 10 vol% FEC (green), 1000ppm of H_2O (blue), and no additives (red). Pristine electrode samples are also given in black.

Figure 5.4(a-f) shows results from surface analysis by XPS of pristine negative and positive electrodes and those extracted after cycling in NMC-V6/SFG6L full cells with electrolytes consisting of 1 M $LiPF_6$ in EC:DEC (1:2 v/v) with either 10 vol% FEC (green), 1000 ppm H_2O (blue), or no additive (red). Comparing the post-formation negative electrode samples in Figure 5.4(a) to the pristine sample, in which essentially no fluorine was detected, shows that the fluorinated compounds originate from the decomposition of electrolyte during cycling. The relative amounts of LiF present were estimated by peak fitting the F1s spectra with gaussian functions. Error in the peak fitting was determined by measuring the variation in the peak ratios corresponding to a ± 1 change in the goodness of fit. The ratio of LiF to other fluorinated compounds (most likely Li_xPOF_y species)[35] is similar for the no additive negative electrode (0.74 ± 0.02) and the negative electrode cycled with 10% FEC (0.66 ± 0.02). In contrast, the ratio of LiF compared to other fluorinated compounds is much larger (0.91 ± 0.01) on the surface of the negative electrode cycled with 1000 ppm H_2O. The increased amount of LiF present in the negative electrode cycled with 1000 ppm H_2O is also evident at the positive electrode (Figure 5.4(b)), where the ratio of LiF to other fluorinated compounds (most likely from the PVDF binder[101]) was 0.31 ± 0.01 on the positive electrode with 1000ppm of H_2O compared to 0.23 ± 0.01 for the cell with 10% FEC. The enhanced LiF content at the negative electrode for the 1000 ppm H_2O and 10% FEC electrolytes is associated with improved alloy cycling performance. It is thought that LiF is a preferred SEI component due to its good passivation layer forming properties, leading to a more compact SEI.[35,52]

All post-formation electrodes form Li_2CO_3 and organic species during cycling (indicated by the presence of C-C, C-H, C-O-C, and C-OH bonding) as indicated in their C1s and O1s spectra (Figure 4(c) and (e), respectively). However, the amount of organic species is enhanced for the negative electrode cycled in 10% FEC compared to the negative electrode cycled with no

additives. This is consistent with previous findings, that associated the presence of enhanced organic species with improved alloy cycling performance. Swapnil Dalavi et al. found that the C1s spectrum of a Si negative electrode with added 3% FEC to 1 M $LiPF_6$ in EC:DMC:DEC (1:1:1 v/v) is characterized by a large C-H peak around 285 eV and small C-O and C=O peaks at 286-287 eV and 288-289 eV, respectively.[78] Interestingly, the negative electrode with 1000 ppm H_2O additive also shows an enhanced presence of organic species. The similarities between peak ratios of cells containing 1000 ppm H_2O and 10% FEC suggest the reduction of H_2O leads to a similar SEI to that of cells with 10% FEC, excepting with even higher LiF content. Apart from enhanced LiF content at the positive electrode for the 1000 ppm H_2O electrolyte (Figure 5.4(b)), the C1s and O1s spectra of the positive electrodes (Figure 5.4(d) and (f)) are similar. This suggests that the addition of 1000 ppm H_2O does not impact the positive electrode surface composition, apart from an increased LiF content.

The above results suggest that H_2O additive in NMC full cells with Si-alloy negative electrodes is effective in increasing cycle life and that the resulting SEI may be similar to that formed by FEC. Therefore, H_2O may be an inexpensive alternative to FEC additive in such cells.

5.3 Conclusions

Water was found to be an effective additive for improving the cycle life of full NMC vs. silicon alloy cells. 1000 ppm or 500 ppm water in the electrolyte resulted in nearly identical improvement in cycle life compared to 10% FEC. These results were not complementary, as combining FEC and H_2O additives resulted in rapid cell failure. Moreover, the use of H_2O as an additive seems to have unique benefits for NMC cells, as it was found to negatively impact LCO cell cycling. These results suggest that the positive electrode may be involved in forming

an intermediate species that subsequently enhances the SEI at the negative electrode. Therefore, H_2O may be an effective and inexpensive additive for Si-alloy cells with NMC positive electrodes.

CHAPTER 6. CONCLUSIONS AND FUTURE WORK

6.1 Solid Phase Additives to Modify SEI Formation

In Chapter 3, LiF was incorporated as solid phase active material additives into Si-Fe alloys. $Si_{40'}(FeSi_2)_{(60-x)'}(LiF)_{(x)'}$ alloys showed increased capacity retention when x= 3, 6, and 9. LiF added as a slurry additive to Si-Fe alloy electrodes also displayed improved cycling performance in FEC containing electrolytes, however the improvement was not as substantial as when the LiF was incorporated directly into the Si-Fe alloy. This suggests that the addition of solid phase additives as components of active materials or as a slurry additive may be a method for improving the electrochemical performance of Li-ion cells. Due to the hygroscopicity of LiF, this method of incorporating LiF into the electrode would not be practical for water-based binders. Thus, other fluorine sources should be considered in a similar application. Alternatively, methods can be implemented to protect the added LiF from H_2O such as carbon coatings. Li_2CO_3 was also tested as a solid phase additive but was found to react with active Si during ball milling. This reactivity with active Si resulted in severe capacity reduction. Therefore, it is suggested that for further work with incorporating solid phase additives like Li_2CO_3 into active materials that new processes be developed to avoid such reactions. The investigation of various components as electrode additives could provide another pathway for increasing the performance of Si-alloy negative electrode material that can be used with traditional alloy compatible binders and liquid electrolyte additives.

6.2 Binder Additives

In Chapter 4, poly-VC was utilized as a binder in Si-Fe alloys. It was discovered that Poly-VC is a poor binder in $Si_{(40)'}(FeSi_2)_{(60)'}$ cells. The specific capacity of $Si_{(40)'}(FeSi_2)_{(60)'}$ cells with Poly-VC binder reduced to ~0mAh/g in FEC containing electrolyte and FEC-free electrolytes at 20 cycles and 13 cycles, respectively. Poly-VC was tested in $Si_{(40)'}(FeSi_2)_{(54)'}(LiF)_{(6)'}$ alloy material from chapter 3 and it was found that no cell in the series tested performed as well as the $Si_{(40)'}(FeSi_2)_{(54)'}(LiF)_{(6)'}$ with PI binder. These results show that poly-VC is not sufficient as a primary binder. To explore the effects of poly-VC on SEI formation, poly-VC should be mixed with another binder in future work to determine if there is an ideal amount of poly-VC to add that will work with the added LiF to replace the use of FEC in Si-Fe alloy electrodes.

6.3 Water as an Electrolyte Additive

In Chapter 5, water was determined to be an effective electrolyte solution additive for improving the cycle life of full NMC vs. silicon alloy cells. 1000 ppm and 500 ppm of water in the electrolyte resulted in improvement in cycle life comparable to 10% FEC. Combining both FEC and H_2O additives resulted in rapid cell failure. The use of H_2O as an additive seems to have unique benefits for NMC cells, as it was found to negatively impact LCO cell cycling. Water is also generally considered detrimental for all Li-ion chemistries. The findings here show that the effects of water are electrode specific, and that water may be beneficial for certain electrode combinations. In the case of NMC/Si-alloy cells the results suggest that the positive electrode may be involved in forming an intermediate species that subsequently enhances the SEI at the negative electrode. Therefore, H_2O may be an effective and inexpensive additive for Si-alloy cells with NMC positive electrodes. The general belief that H_2O is detrimental to cell

cycling likely means that its potential benefits for certain electrode combinations have not been sufficiently explored. It would be interesting, in future work, to test the effects of H_2O additive with cells containing other types of positive and negative electrode material combinations such as lithium iron phosphate (LFP), lithium nickel cobalt aluminum oxide (NCA) positive electrodes vs. graphite and Si-alloy electrodes. In addition, it would be interesting to explore blended electrodes, for instance if the H_2O tolerance of LCO vs. graphite cells could be improved by adding small amounts of NMC to the positive electrode and Si-alloy to the negative electrode. In addition to cycle life, the effect of H_2O additive on gas production and long-term storage are other important parameters that require further study in order to evaluate the use of H_2O as an effective additive for practical Si-alloy/NMC cells.

BIBLIOGRAPHY

1. J. P. Deane, B. P. Ó Gallachóir, and E. J. McKeogh, Techno-economic review ofexisting and new pumped hydro energy storage plant. *Renew. Sustain. Energy Rev.*, **14**, 1293–1302 (2010).

2. Y. Liang, C. Zhao, H. Yuan et al., A review of rechargeable batteries for portable electronic devices. *InfoMat*, **1**, 6–32 (2019).

3. J. Park, *Principles and Applications of Lithium Secondary Batteries*, (2012).

4. C. P. Grey and D. S. Hall, Prospects for lithium-ion batteries and beyond - a 2030 vision. *Nat. Commun.*, **11**, 6279 (2020).

5. E. Peled and S. Menkin, Review-SEI: Past, Present and Future. *J. Electrochem. Soc.*, **164**, 1703–1719 (2017).

6. Z. S. Wu, L. Xue, W. Ren et al., A LiF nanoparticle-modified graphene electrode for high-power and high-energy lithium ion batteries. *Adv. Funct. Mater.*, **22**, 3290–3297 (2012).

7. R. Korthauer, *Lithium-Ion Batteries: Basics and Applications*, (2018).

8. N. Nitta, F. Wu, J. T. Lee, and G. Yushin, Li-ion battery materials: Present and future. *Mater. Today*, **18**, 252–264 (2015).

9. C. S. Ioakimidis, A. Murillo-Marrodán, A. Bagheri, et al., Life cycle assessment of a lithium iron phosphate (LFP) electric vehicle battery in second life application scenarios. *Sustain.*, **11**, 2527 (2019).

10. G. Liang, V. K. Peterson, K. W. See, et al., Enhanced magnetic properties of co-doped $BiFeO_3$ thin films via structural progression. *J. Mater. Chem. A*, **8**, 15373–15398 (2020).

11. G. Plett, *Battery Management Systems, Battery Modeling*, (2015).

12. M. N. Obrovac and V. L. Chevrier, Alloy negative electrodes for Li-ion batteries. *Chem. Rev.*, **114**, 11444–11502 (2014).

13. M. K. Song, S. Do Hong, and K. T. No, The Structure of Lithium Intercalated Graphite Using an Effective Atomic Charge of Lithium. *J. Electrochem. Soc.*, **148**, A1159 (2001).

14. S. Basu, C. Zeller, P. J. Flanders et al., Synthesis and properties of lithium-graphite intercalation compounds. *Mater. Sci. Eng.*, **38**, 275–283 (1979).

15. M. N. Obrovac, Si-alloy negative electrodes for Li-ion batteries. *Curr. Opin. Electrochem.*, **9**, 8–17 (2018).

16. M. T. McDowell, S. W. Lee, W. D. Nix, and Y. Cui, 25th anniversary article: Understanding the lithiation of silicon and other alloying anodes for lithium-ion batteries. *Adv. Mater.*, **25**, 4966–4985 (2013).

17. L. Y. Beaulieu, T. D. Hatchard, A. Bonakdarpour et al., Reaction of Li with Alloy Thin Films Studied by In Situ AFM. *J. Electrochem. Soc.*, **150**, A1457 (2003).

18. L. MacEachern, R. A. Dunlap, and M. N. Obrovac, Mechanically Milled Fe-Si-Zn Alloys as Negative Electrodes for Li-Ion Batteries. *J. Electrochem. Soc.*, **162**, A2319–A2324 (2015).

19. D. S. M. Iaboni and M. N. Obrovac, $Li_{15}Si_4$ Formation in Silicon Thin Film Negative Electrodes. *J. Electrochem. Soc.*, **163**, A255–A261 (2016).

20. Y. Cao, B. Scott, R. A. Dunlap et al., An Investigation of the Fe-Mn-Si System for Li-Ion Battery Negative Electrodes. *J. Electrochem. Soc.*, **166**, A21–A26 (2019).

21. M. N. Obrovac, L. Christensen, D. B. Le, and J. R. Dahn, Alloy negative electrodes for Li-ion batteries. *J. Electrochem. Soc.*, **154**, A849 (2007).

22. V. L. Chevrier, L. Liu, D. B. Le et al., Evaluating Si-Based Materials for Li-Ion Batteries in Commercially Relevant Negative Electrodes. *J. Electrochem. Soc.*, **161**, A783–A791 (2014).

23. V. A. Sethuraman, M. J. Chon, M. Shimshak et al., In situ measurements of stress evolution in silicon thin films during electrochemical lithiation and delithiation. *J. Power Sources*, **195**, 5062–5066 (2010).

24. M. J. Chon, V. A. Sethuraman, A. McCormick et al., Real-time measurement of stress and damage evolution during initial lithiation of crystalline silicon. *Phys. Rev. Lett.*, **107**, 1–4 (2011).

25. K. Xu, Electrolytes and interphases in Li-ion batteries and beyond. *Chem. Rev.*, **114**, 11503–11618 (2014).

26. C. L. Campion, W. Li, and B. L. Lucht, Thermal Decomposition of $LiPF_6$-Based Electrolytes for Lithium-Ion Batteries *J. Electrochem. Soc.*, **152**, A2327 (2005).

27. S. S. Zhang, A review on electrolyte additives for lithium-ion batteries. *J. Power Sources*, **162**, 1379–1394 (2006).

28. K. Xu, Nonaqueous liquid electrolytes for lithium-based rechargeable batteries. *Chem. Rev.*, **104**, 4303–4417 (2004).

29. M. Inaba, Z. Siroma, Y. Kawatate et al., Electrochemical scanning tunneling microscopy analysis of the surface reactions on graphite basal plane in ethylene carbonate-based solvents and propylene carbonate. *J. Power Sources*, **68**, 221–226 (1997).

30. J. O. Besenhard, M. Winter, J. Yang, and W. Biberacher, Filming mechanism of lithium-carbon anodes in organic and inorganic electrolytes. *J. Power Sources*, **54**, 228–231 (1995).

31. P. Novák, F. Joho, M. Lanz et al., The complex electrochemistry of graphite electrodes in lithium-ion batteries. *J. Power Sources*, **97**–**98**, 39–46 (2001).

32. H. H. Lee, C. C. Wan, and Y. Y. Wang, Thermal Stability of the Solid Electrolyte Interface on Carbon Electrodes of Lithium Batteries. *J. Electrochem. Soc.*, **151**, A542 (2004).

33. M. Dahbi, F. Ghamouss, F. Tran-Van et al., Comparative study of EC/DMC LiTFSI and $LiPF_6$ electrolytes for electrochemical storage. *J. Power Sources*, **196**, 9743–9750 (2011).

34. Y. Okuno, K. Ushirogata, K. Sodeyama, and Y. Tateyama, Decomposition of the fluoroethylene carbonate additive and the glue effect of lithium fluoride products for the solid electrolyte interphase: An ab initio study. *Phys. Chem. Chem. Phys.*, **18**, 8643–8653 (2016).

35. L. Ma, L. Ellis, S. L. Glazier et al., Combinations of $LiPO_2F_2$ and Other Electrolyte Additives in $Li[Ni_{0.5}Mn_{0.3}Co_{0.2}]O_2$ /Graphite Pouch Cells. *J. Electrochem. Soc.*, **165**, A1718–A1724 (2018).

36. M. Sina, J. Alvarado, H. Shobukawa et al., Direct Visualization of the Solid Electrolyte Interphase and Its Effects on Silicon Electrochemical Performance. *Adv. Mater. Interfaces*, **3**, 1–10 (2016).

37. E. Markevich, G. Salitra, and D. Aurbach, Fluoroethylene Carbonate as an Important Component for the Formation of an Effective Solid Electrolyte Interphase on Anodes and Cathodes for Advanced Li-Ion Batteries. *ACS Energy Lett.*, **2**, 1337–1345 (2017).

38. R. Elazari, G. Salitra, G. Gershinsky et al., Li Ion Cells Comprising Lithiated Columnar Silicon Film Anodes, TiS_2 Cathodes and Fluoroethyene Carbonate (FEC) as a Critically Important Component. *J. Electrochem. Soc.*, **159**, A1440–A1445 (2012).

39. S. J. An, J. Li, C. Daniel et al., The state of understanding of the lithium-ion-battery graphite solid electrolyte interphase (SEI) and its relationship to formation cycling. *Carbon N. Y.*, **105**, 52–76 (2016).

40. Jurgen O. Besenhard, *Hand Book of Battery Material*, (1999).

41. E. Peled, D. Golodnitsky, and G. Ardel, Advanced Model for Solid Electrolyte Interphase Electrodes in Liquid and Polymer Electrolytes. *J. Electrochem. Soc.*, **144**, L208–L210 (1997).

42. W. Liu, P. Liu, and D. Mitlin, Review of Emerging Concepts in SEI Analysis and Artificial SEI Membranes for Lithium, Sodium, and Potassium Metal Battery Anodes. *Adv. Energy Mater.*, **10**, 1–24 (2020).

43. J. G. Thevenin and R. H. Muller, Impedance of Lithium Electrodes in a Propylene Carbonate Electrolyte. *J. Electrochem. Soc.*, **134**, 273–280 (1987).

44. Z. Yan, C. Wei, and M. N. Obrovac, Understanding interfacial impedance growth in porous electrodes containing blended active materials. *J. Power Sources*, **438**, 226955 (2019).

45. P. Verma, P. Maire, and P. Novák, A review of the features and analyses of the solid electrolyte interphase in Li-ion batteries. *Electrochim. Acta*, **55**, 6332–6341 (2010).

46. H. Momose, H. Honbo, S. Takeuchi et al., X-ray photoelectron spectroscopy analyses of lithium intercalation and alloying reactions on graphite electrodes. *J. Power Sources*, **68**, 208–211 (1997).

47. S. Ma, M. Jiang, P. Tao et al., Temperature effect and thermal impact in lithium-ion batteries: A review. *Prog. Nat. Sci. Mater. Int.*, **28**, 653–666 (2018).

48. Y. Guo, D. Li, R. Xiong, and H. Li, Investigation of the temperature-dependent behaviours of Li metal anode. *Chem. Commun.*, **55**, 9773–9776 (2019).

49. A. Zaban and D. Aurbach, Impedance spectroscopy of lithium and nickel electrodes in propylene carbonate solutions of different lithium salts A comparative study. *J. Power Sources*, **54**, 289–295 (1995).

50. D. Bar-Tow, E. Peled, and L. Burstein, A Study of Highly Oriented Pyrolytic Graphite as a Model for the Graphite Anode in Li-Ion Batteries. *J. Electrochem. Soc.*, **146**, 824–832 (1999).

51. E. Peled, D. Bar-Tow, A. Merson et al., Composition, depth profiles and lateral distribution of materials in the SEI built on HOPG-TOF SIMS and XPS studies. *J. Power Sources*, **97**–**98**, 52–57 (2001).

52. Y. X. Lin, Z. Liu, K. Leung et al., Connecting the irreversible capacity loss in Li-ion batteries with the electronic insulating properties of solid electrolyte interphase (SEI) components. *J. Power Sources*, **309**, 221–230 (2016).

53. A. Schiele, B. Breitung, T. Hatsukade et al., The Critical Role of Fluoroethylene Carbonate in the Gassing of Silicon Anodes for Lithium-Ion Batteries. *ACS Energy Lett.*, **2**, 2228–2233 (2017).

54. M. Moshkovich, M. Cojocaru, H. E. Gottlieb, and D. Aurbach, The study of the anodic stability of alkyl carbonate solutions by in situ FTIR spectroscopy, EQCM, NMR and MS. *J. Electroanal. Chem.*, **497**, 84–96 (2001).

55. D. Aurbach, Review of selected electrode-solution interactions which determine the performance of Li and Li ion batteries. *J. Power Sources*, **89**, 206–218 (2000).

56. T. Eriksson, A. M. Andersson, C. Gejke, T. Gustafsson, and J. O. Thomas, Influence of Temperature on the Interface Chemistry of $Li_xMn_2O_4$ Electrodes. *Langmuir*, **18**, 3609–3619 (2002).

57. T. Eriksson, T. Gustafsson, and J. O. Thomas, Surface structure of $LiMn_2O_4$ electrodes. *Electrochem. Solid-State Lett.*, **5**, A35-A38 (2002).

58. T. J. Lee, H. Kim, H. S. Hwang et al., Solid Permeable Interface (SPI) on a High-Voltage Positive Electrode of Lithium-Ion Batteries. *J. Electrochem. Soc.*, **165**, A575–A583 (2018).

59. D. L. Zhang, Processing of advanced materials using high-energy mechanical milling. *Prog. Mater. Sci.*, **49**, 537–560 (2004).

60. P. S. Gilman and J. S. Benjamin, Mechanical Alloying. *Ann. Rev. Mater. Sci.*, **13**, 279–300 (1983).

61. T. D. Hatchard, A. Genkin, and M. N. Obrovac, Rapid mechanochemical synthesis of amorphous alloys. *AIP Adv.*, **7**, 045201 (2017).

62. B. N. Wilkes, Z. L. Brown, L. J. Krause et al., The Electrochemical Behavior of Polyimide Binders in Li and Na Cells. *J. Electrochem. Soc.*, **163**, A364–A372 (2016).

63. W. Zhou and Z. L. Wang, *Scanning Microscopy for Nanotechnology*, (2007).

64. R. Jenkins and R. Snyder, *Introduction to X-ray Powder Diffractometry*, (1996).

65. G. Bhagavannarayana, S. Parthiban, C. Chandrasekaran, and S. Meenakshisundaram, Powder Diffraction Data for Pure KHP. *CrystEngComm* (2009).

66. G. Bhagavannarayana, S. Parthiban, C. Chandrasekaran, and S. Meenakshisundaram, Effect of alkaline earth and transition metals doping on the properties and crystalline perfection of potassium hydrogen phthalate (KHP) crystals. *CrystEngComm*, **11**, 1635–1641 (2009).

67. T. L. Alford, L. C. Feldman, and J. W. Mayer, *Fundamentals of Nanoscale Film Analysis,* (2007).

68. J. F. Watts and J. Wolstenholme, *An Introduction to Surface Analysis by XPS and AES*, (2003).

69. R. Nix, *LibreTexts*, **10**, 22 (2021).

70. M. E. Orazem and B. Tribollet, *Electrochemical Impedance Spectroscopy*, (2017).

71. A. Lasia, *Electrochemical impedance spectroscopy and its applications*, (2014).

72. P. B. Balbuena and Y. Wang, *Lithium-Ion Batteries - Solid-Electrolyte Interphase*, (2004).

73. Z. Du, R. A. Dunlap, and M. N. Obrovac, Structural and Electrochemical Investigation of Fe_xSi_{1-x} Thin Films in Li Cells. *J. Electrochem. Soc.*, **163**, A2011–A2016 (2016).

74. M. N. Obrovac and L. Christensen, Structural Changes in Silicon Anodes during Lithium Insertion/Extraction. *Electrochem. Solid-State Lett.*, **7**, A93 (2004).

75. R. Petibon, L. Madec, D. W. Abarbanel, and J. R. Dahn, Effect of $LiPF_6$ concentration in $Li[Ni_{0.4}Mn_{0.4}Co_{0.2}]O_2$/graphite pouch cells operated at 4.5V. *J. Power Sources*, **300**, 419–429 (2015).

76. L. J. Krause, T. Brandt, V. L. Chevrier, and L. D. Jensen, Surface Area Increase of Silicon Alloys in Li-Ion Full Cells Measured by Isothermal Heat Flow Calorimetry. *J. Electrochem. Soc.*, **164**, A2277–A2282 (2017).

77. L. Bai, M. Sun, W. Ma et al., Enhanced magnetic properties of co-doped $BiFeO_3$ thin films via structural progression. *Nanomaterials*, **10**, 1–13 (2020).

78. S. Dalavi, P. Guduru, and B. L. Lucht, Performance Enhancing Electrolyte Additives for Lithium Ion Batteries with Silicon Anodes. *J. Electrochem. Soc.*, **159**, A642-A646 (2012).

79. G. Yang, J. Shi, C. Shen et al., Improving the cyclability performance of lithium-ion batteries by introducing lithium difluorophosphate ($LiPO_2F_2$) additive. *RSC Adv.*, **7**, 26052–26059 (2017).

80. B. Zhang, M. Metzger, S. Solchenbach et al., Role of 1,3-propane sultone and vinylene carbonate in solid electrolyte interface formation and gas generation. *J. Phys. Chem. C*, **119**, 11337–11348 (2015).

81. M. Wachtler, M. R. Wagner, M. Schmied et al., The effect of the binder morphology on the cycling stability of Li-alloy composite electrodes. *J. Electroanal. Chem.*, **510**, 12–19 (2001).

82. S. Komaba, N. Yabuuchi, T. Ozeki et al., Comparative study of sodium polyacrylate and poly(vinylidene fluoride) as binders for high capacity si-graphite composite negative electrodes in Li-ion batteries. *J. Phys. Chem. C*, **116**, 1380–1389 (2012).

83. A. L. Michan, B. S. Parimalam, M. Leskes et al., Fluoroethylene carbonate and vinylene carbonate reduction: Understanding lithium-ion battery electrolyte additives and solid electrolyte interphase formation. *Chem. Mater.*, **28**, 8149–8159 (2016).

84. H. Zhao, X. Zhou, S. Park et al., A polymerized vinylene carbonate anode binder enhances performance of lithium-ion batteries. *J. Power Sources*, **263**, 288–295 (2014).

85. Q. Yuan, F. Zhao, Y. Zhao, Z. Liang, and D. Yan, Reason analysis for Graphite-Si/SiOx/C composite anode cycle fading and cycle improvement with PI binder. *J. Solid State Electrochem.*, **18**, 2167–2174 (2014).

86. K. Schroder et al., The Effect of Fluoroethylene Carbonate as an Additive on the Solid Electrolyte Interphase on Silicon Lithium-Ion Electrodes. *Chem. Mater.*, **27**, 5531–5542 (2015).

87. R. Bernhard, M. Metzger, and H. A. Gasteiger, Gas Evolution at Graphite Anodes Depending on Electrolyte Water Content and SEI Quality Studied by On-Line Electrochemical Mass Spectrometry. *J. Electrochem. Soc.*, **162**, A1984–A1989 (2015).

88. A. Wuersig, W. Scheifele, and P. Novák, CO_2 Gas Evolution on Cathode Materials for Lithium-Ion Batteries. *J. Electrochem. Soc.*, **154**, A449 (2007).

89. R. Jung, M. Metzger, F. Maglia et al., Oxygen Release and Its Effect on the Cycling Stability of $LiNi_xMn_yCo_zO_2$ (NMC) Cathode Materials for Li-Ion Batteries. *J. Electrochem. Soc.*, **164**, A1361–A1377 (2017).

90. L. D. Ellis, J. P. Allen, L. M. Thompson et al., Quantifying, Understanding and Evaluating the Effects of Gas Consumption in Lithium-Ion Cells. *J. Electrochem. Soc.*, **164**, A3518–A3528 (2017).

91. G. Zhuang, P. N. Ross, F. Kong, and F. McLarnon, The Reaction of Clean Li Surfaces with Small Molecules in Ultrahigh Vacuum: II. Water. *J. Electrochem. Soc.*, **145**, 159–164 (1998).

92. D. Aurbach, I. Weissman, A. Zaban, and P. Dan, On the role of water contamination in rechargeable Li batteries. *Electrochim. Acta*, **45**, 1135–1140 (1999).

93. S. F. Lux, J. Chevalier, I. T. Lucas, and R. Kostecki, HF formation in $LiPF_6$-based organic carbonate electrolytes. *ECS Electrochem. Lett.*, **2**, 121–123 (2013).

94. X. Ren, J. Wang, Z. Peng, and L. Lu, Direct monitoring of trace water in Li-ion batteries using: Operando fluorescence spectroscopy. *Chem. Sci.*, **9**, 231–237 (2017).

95. J. L. Tebbe, A. M. Holder, and C. B. Musgrave, Mechanisms of $LiCoO_2$ Cathode Degradation by Reaction with HF and Protection by Thin Oxide Coatings. *ACS Appl. Mater. Interfaces*, **7**, 24265–24278 (2015).

96. H. Lin, H. Noguchi, and K. Uosaki, Effects of HF on the Lithiation Behavior of the Silicon Anode in $LiPF_6$ Organic Electrolyte Solution. *ACS Omega*, **5**, 2081–2087 (2020).

97. D. J. Xiong, R. Petibon, L. Madec et al., Some Effects of Intentionally Added Water on $LiCoO_2$/Graphite Pouch Cells. *J. Electrochem. Soc.*, **163**, A1678–A1685 (2016).

98. J. C. Burns, N. N. Sinha, Gaurav Jain et al., The Impact of Intentionally Added Water to the Electrolyte of Li-ion Cells: I. Cells with Graphite Negative Electrodes. *J. Electrochem. Soc.*, **160**, A2281–A2287 (2013).

99. J. C. Burns, N. N. Sinha, Gaurav Jain et al., The Impact of Intentionally Added Water to the Electrolyte of Li-ion Cells: II. Cells with Lithium Titanate Negative Electrodes. *J. Electrochem. Soc.*, **161**, A247–A255 (2014).

100. S. A. Freunberger, Y. Chen, Z. Peng et al., Reactions in the rechargeable lithium-O_2 battery with alkyl carbonate electrolytes. *J. Am. Chem. Soc.*, **133**, 8040–8047 (2011)..

101. R. Crowe and J. P. S. Badyal, Surface modification of poly(vinylidene difluoride) (PVDF) by LiOH. *J. Chem. Soc. Chem. Commun.*, **14**, 958–959 (1991).

APPENDIX

This Agreement between Dalhousie University -- Robert Young ("You") and Springer Nature ("Springer Nature") consists of your license details and the terms and conditions provided by Springer Nature and Copyright Clearance Center.

License Number	5110350276339
License date	Jul 15, 2021
Licensed Content Publisher	Springer Nature
Licensed Content Publication	Springer eBook
Licensed Content Title	Lithium-ion battery overview
Licensed Content Author	Stephan Leuthner
Licensed Content Date	Jan 1, 2018
Type of Use	Thesis/Dissertation
Requestor type	academic/university or research institute
Format	print and electronic
Portion	figures/tables/illustrations
Number of figures/tables/illustrations	1
Will you be translating?	no
Circulation/distribution	200 - 499
Author of this Springer Nature content	no
Title	UNCONVENTIONAL ADDITIVES FOR IMPROVING THE SOLID ELECTROLYTE INTERPHASE IN LI-ION BATTERIES
Institution name	Dalhousie University
Expected presentation date	Aug 2021
Portions	Figure 2.1, Chapter 2, Page 15
Requestor Location	Dalhousie University

Order Date	14-Jul-2021	Type of Use	Republish in a thesis/dissertation
Order License ID	1133114-1	Portion	Chart/graph/table/figure
ISBN-13	9781630810276		

LICENSED CONTENT

Publication Title	Battery management systems	Country	United States of America
Author/Editor	Plett, Gregory L.	Rightsholder	Artech House Inc
Date	01/01/2015	Publication Type	Book
Language	English		

REQUEST DETAILS

Portion Type	Chart/graph/table/figure	Distribution	Worldwide
Number of charts / graphs / tables / figures requested	2	Translation	Original language of publication
		Copies for the disabled?	No
Format (select all that apply)	Print, Electronic	Minor editing privileges?	Yes
Who will republish the content?	Academic institution	Incidental promotional use?	No
Duration of Use	Current edition and up to 5 years	Currency	CAD
Lifetime Unit Quantity	Up to 499		
Rights Requested	Main product		

NEW WORK DETAILS

Title	UNCONVENTIONAL ADDITIVES FOR IMPROVING THE SOLID ELECTROLYTE INTERPHASE IN LI-ION BATTERIES	Institution name	Dalhousie University
		Expected presentation date	2021-08-13
Instructor name	Mark Obrovac		

ACS Publications
Most Trusted. Most Cited. Most Read.

Alloy Negative Electrodes for Li-Ion Batteries

Author: M. N. Obrovac, V. L. Chevrier
Publication: Chemical Reviews
Publisher: American Chemical Society
Date: Dec 1, 2014

PERMISSION/LICENSE IS GRANTED FOR YOUR ORDER AT NO CHARGE

This type of permission/license, instead of the standard Terms and Conditions, is sent to you because no fee is being charged for your order. Please note the following:

- Permission is granted for your request in both print and electronic formats, and translations.
- If figures and/or tables were requested, they may be adapted or used in part.
- Please print this page for your records and send a copy of it to your publisher/graduate school.
- Appropriate credit for the requested material should be given as follows: "Reprinted (adapted) with permission from {COMPLETE REFERENCE CITATION}. Copyright {YEAR} American Chemical Society." Insert appropriate information in place of the capitalized words.
- One-time permission is granted only for the use specified in your RightsLink request. No additional uses are granted (such as derivative works or other editions). For any uses, please submit a new request.

If credit is given to another source for the material you requested from RightsLink, permission must be obtained from that source.

Order Date	16-Jul-2021	Type of Use	Republish in a thesis/dissertation
Order License ID	1133687-1	Publisher	IOP Publishing
ISSN	1945-7111	Portion	Chart/graph/table/figure

LICENSED CONTENT

Publication Title	Journal of the Electrochemical Society	Country	United States of America
Author/Editor	Electrochemical Society.	Rightsholder	IOP Publishing, Ltd
Date	01/01/1948	Publication Type	e-Journal
Language	English	URL	http://www.scitation.org/JES

REQUEST DETAILS

Portion Type	Chart/graph/table/figure	Distribution	Worldwide
Number of charts / graphs / tables / figures requested	1	Translation	Original language of publication
		Copies for the disabled?	No
Format (select all that apply)	Print, Electronic	Minor editing privileges?	Yes
Who will republish the content?	Author of requested content	Incidental promotional use?	No
Duration of Use	Current edition and up to 5 years	Currency	CAD
Lifetime Unit Quantity	Up to 499		
Rights Requested	Main product		

NEW WORK DETAILS

Title	UNCONVENTIONAL ADDITIVES FOR IMPROVING THE SOLID ELECTROLYTE INTERPHASE IN LI-ION BATTERIES	Institution name	Dalhousie University
		Expected presentation date	2021-08-13
Instructor name	Mark Obrovac		

Order Date	16-Jul-2021	Type of Use	Republish in a thesis/dissertation
Order License ID	1133761-1	Publisher	ELSEVIER S.A.
ISSN	0378-7753	Portion	Chart/graph/table/figure

LICENSED CONTENT

Publication Title	Journal of power sources	Publication Type	Journal
Article Title	Filming mechanism of lithium-carbon anodes in organic and inorganic electrolytes	Start Page	228
		End Page	231
		Issue	2
Date	01/01/1976	Volume	54
Language	English, French, French, German, German		
Country	Switzerland		
Rightsholder	Elsevier Science & Technology Journals		

REQUEST DETAILS

Portion Type	Chart/graph/table/figure	Distribution	Worldwide
Number of charts / graphs / tables / figures requested	1	Translation	Original language of publication
		Copies for the disabled?	No
Format (select all that apply)	Print, Electronic	Minor editing privileges?	Yes
Who will republish the content?	Author of requested content	Incidental promotional use?	No
Duration of Use	Life of current edition	Currency	CAD
Lifetime Unit Quantity	Up to 499		
Rights Requested	Main product		

NEW WORK DETAILS

Title	UNCONVENTIONAL ADDITIVES FOR IMPROVING THE SOLID ELECTROLYTE INTERPHASE IN LI-ION BATTERIES	Institution name	Dalhousie University
		Expected presentation date	2021-08-13
Instructor name	Mark Obrovac		

Order Date	16-Jul-2021	Type of Use	Republish in a thesis/dissertation
Order License ID	1133762-1	Publisher	IOP Publishing
ISSN	1945-7111	Portion	Chart/graph/table/figure

LICENSED CONTENT

Publication Title	Journal of the Electrochemical Society	Publication Type	e-Journal
Article Title	Review—SEI: Past, Present and Future	Start Page	A1703
Author/Editor	Electrochemical Society.	End Page	A1719
Date	01/01/1948	Issue	7
Language	English	Volume	164
Country	United States of America	URL	http://www.scitation.org/JES
Rightsholder	IOP Publishing, Ltd		

REQUEST DETAILS

Portion Type	Chart/graph/table/figure	Distribution	Worldwide
Number of charts / graphs / tables / figures requested	1	Translation	Original language of publication
Format (select all that apply)	Print, Electronic	Copies for the disabled?	No
Who will republish the content?	Author of requested content	Minor editing privileges?	Yes
Duration of Use	Life of current edition	Incidental promotional use?	No
Lifetime Unit Quantity	Up to 499	Currency	CAD
Rights Requested	Main product		

NEW WORK DETAILS

Title	UNCONVENTIONAL ADDITIVES FOR IMPROVING THE SOLID ELECTROLYTE INTERPHASE IN LI-ION BATTERIES	Institution name	Dalhousie University
		Expected presentation date	2021-08-13
Instructor name	Mark Obrovac		

Order Date	16-Jul-2021	Type of Use	Republish in a thesis/dissertation
Order License ID	1133764-1	Publisher	IOP Publishing
ISSN	1945-7111	Portion	Chart/graph/table/figure

LICENSED CONTENT

Publication Title	Journal of the Electrochemical Society	Publication Type	e-Journal
Article Title	Advanced Model for Solid Electrolyte Interphase Electrodes in Liquid and Polymer Electrolytes	Start Page	L208
		End Page	L210
Author/Editor	Electrochemical Society.	Issue	8
Date	01/01/1948	Volume	144
Language	English	URL	http://www.scitation.org/JES
Country	United States of America		
Rightsholder	IOP Publishing, Ltd		

REQUEST DETAILS

Portion Type	Chart/graph/table/figure	Distribution	Worldwide
Number of charts / graphs / tables / figures requested	1	Translation	Original language of publication
Format (select all that apply)	Print, Electronic	Copies for the disabled?	No
Who will republish the content?	Author of requested content	Minor editing privileges?	Yes
Duration of Use	Life of current edition	Incidental promotional use?	No
Lifetime Unit Quantity	Up to 499	Currency	CAD
Rights Requested	Main product		

NEW WORK DETAILS

Title	UNCONVENTIONAL ADDITIVES FOR IMPROVING THE SOLID ELECTROLYTE INTERPHASE IN LI-ION BATTERIES	Institution name	Dalhousie University
		Expected presentation date	2021-08-13
Instructor name	Mark Obrovac		